The use of magnetic fields to create high-speed plasma jets for spacecraft propulsion.

Stephen Norman Bathgate

A thesis submitted in fulfilment of
the requirements for the degree of
Doctor of Philosophy.

University of Sydney - Faculty of Science - School of Physics

February 2017

This is to certify that to the best of my knowledge, the content of this thesis is my own work. This thesis has not been submitted for any degree or other purposes.

I certify that the intellectual content of this thesis is the product of my own work and that all the assistance received in preparing this thesis and sources have been acknowledged.

Stephen Bathgate

This thesis contains material published in *Plasma Science and Technology*, chapter 1 to 5, published in the *European Physical Journal Applied Physics (2016) 76: 30801,* chapter 8 and submitted to the *European Physical Journal Applied Physics,* chapter 9. In all cases, I designed the study, analysed the data, wrote the drafts of the manuscript and prepared the illustrations.

And yet surely to alchemy this right is due, that it may be compared to the husbandman whereof Æsop makes the fable, that when he died he told his sons that he had left unto them gold buried under the ground in his vineyard: and they digged over the ground, gold they found none, but by reason of their stirring and digging the mould about the roots of their vines, they had a great vintage the year following: so assuredly the search and stir to make gold hath brought to light a great number of good and fruitful inventions and experiments, as well for the disclosing of nature as for the use of man's life.
Sir Francis Bacon,
The Advancement of Learning (1605)

Nothing in this world can take the place of persistence. Talent will not. Nothing is more common than unsuccessful men with talent. Genius will not. Unrewarded genius is almost a proverb. Education will not. The world is full of educated derelicts. Persistence and determination alone are omnipotent.
Calvin Coolidge
30th President of the United States

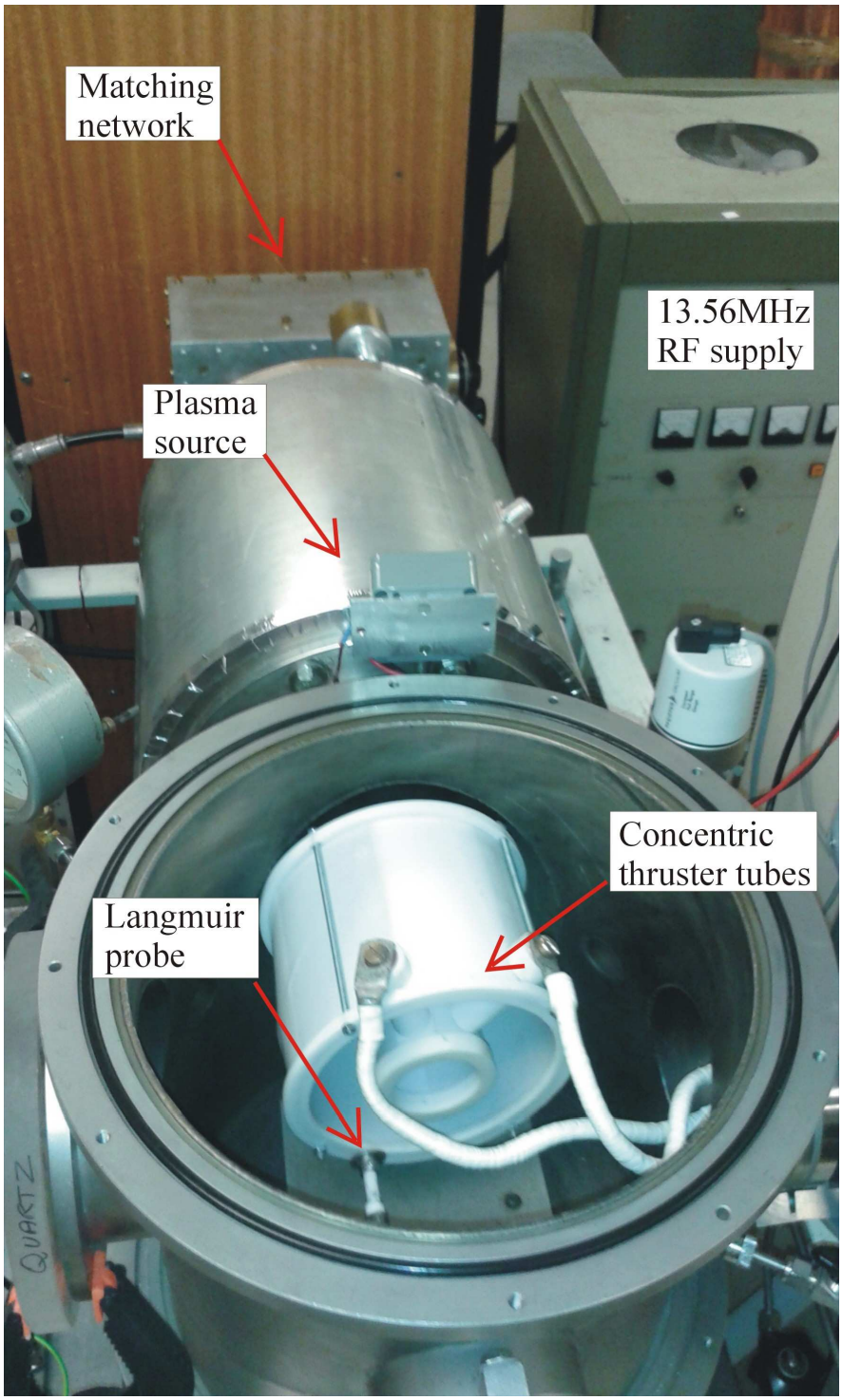

The experimental magnetic reconnection thruster constructed for this investigation. Consisting of two concentric copper tubes, the inner tube acts as a theta pinch device while the annular region between the inner and outer tubes is designed to produce magnetic reconnection in a plasma. In operation, the copper tubes were covered with Teflon insulation to prevent the driving current shorting to ground through the conductive plasma
A large current pulse was applied to the terminals and the resulting magnetic interactions along the axis and in the annulus were investigated as a means of producing high-speed plasma jets suitable for spacecraft propulsion.

Contents

Acknowledgements

In a complex project such as that described in this work acknowledging the contributions of all those who have assisted in its completion is in itself a significant task.

I would like to thank Professor David McKenzie, my primary supervisor, for his unfailing enthusiasm and ever-willing guidance in negotiating what has been a long and at times drawn out attempt to design, construct and implement two complex and quite different devices. Firstly, the magnetic reconnection-theta pinch thruster and then secondly, the HiPIMS thruster.

Adding to Professor McKenzie's invaluable advice, Professor Marcela Bilek has always been willing to engage in the effort to understand the intricacies of the effort of deriving meaning from what at times have been obscure findings. She has unfailingly given excellent advice in the preparation of research papers and this thesis from those results.

The coursework provided by Professors Serdar Kuyucak and Iver Cairns was both challenging and interesting. Dr. Ian Falconer kindly gave up his time to read through my review – or as he said book - on electrodeless plasma thrusters that has formed the basis of a research paper and the first part of this dissertation.

Dr. Rajesh Ganesan's enthusiastic participation in the HiPIMS experiments was an essential contribution to this work while on the more practical side, Phil Dennis offered invaluable advice and assistance in the design and construction of the apparatus used in both the HiPIMS and magnetic reconnection experiments. His understanding of the arcane details of radio frequency devices was of very considerable importance in the ultimate success of producing stable plasma in what was, in the scale of the plasma physics laboratory, a substantial experimental chamber.

That chamber itself passed through a number of iterations until Terry Pfeiffer, Senior Technical Officer in the former School of Physics workshop, in large part constructed the final version. Succeeding several earlier versions, the chamber was finally capable of maintaining a stable discharge and became the central component in the concluding magnetic reconnection experiments.

I also wish to acknowledge the financial support of the Australian Research Council for this project and the assistance accorded by the Australian Government in the provision of an Australian Postgraduate Award.

On the home front, my partner Jennifer has been consistently supportive and always tolerant of the time that I have spent in front of my computer, in the home workshop or in the lab, labouring over complex and often inscrutable documents and components that have been central to the task of completing this extended effort.

Lastly, I wish to mention the unflagging encouragement of my parents in my endeavours through the years. It is to their memory that this thesis is dedicated.

Publications

1. S. N. Bathgate, R. Ganesan, M. M.M. Bilek and D. R. McKenzie, *"A HiPIMS plasma source with a magnetic nozzle that accelerates ions: application in a thruster", Eur. Phys. J. Appl. Phys. (2016) 76: 30801,* 2016. An illustration from that paper was published on the front cover of the journal (below).

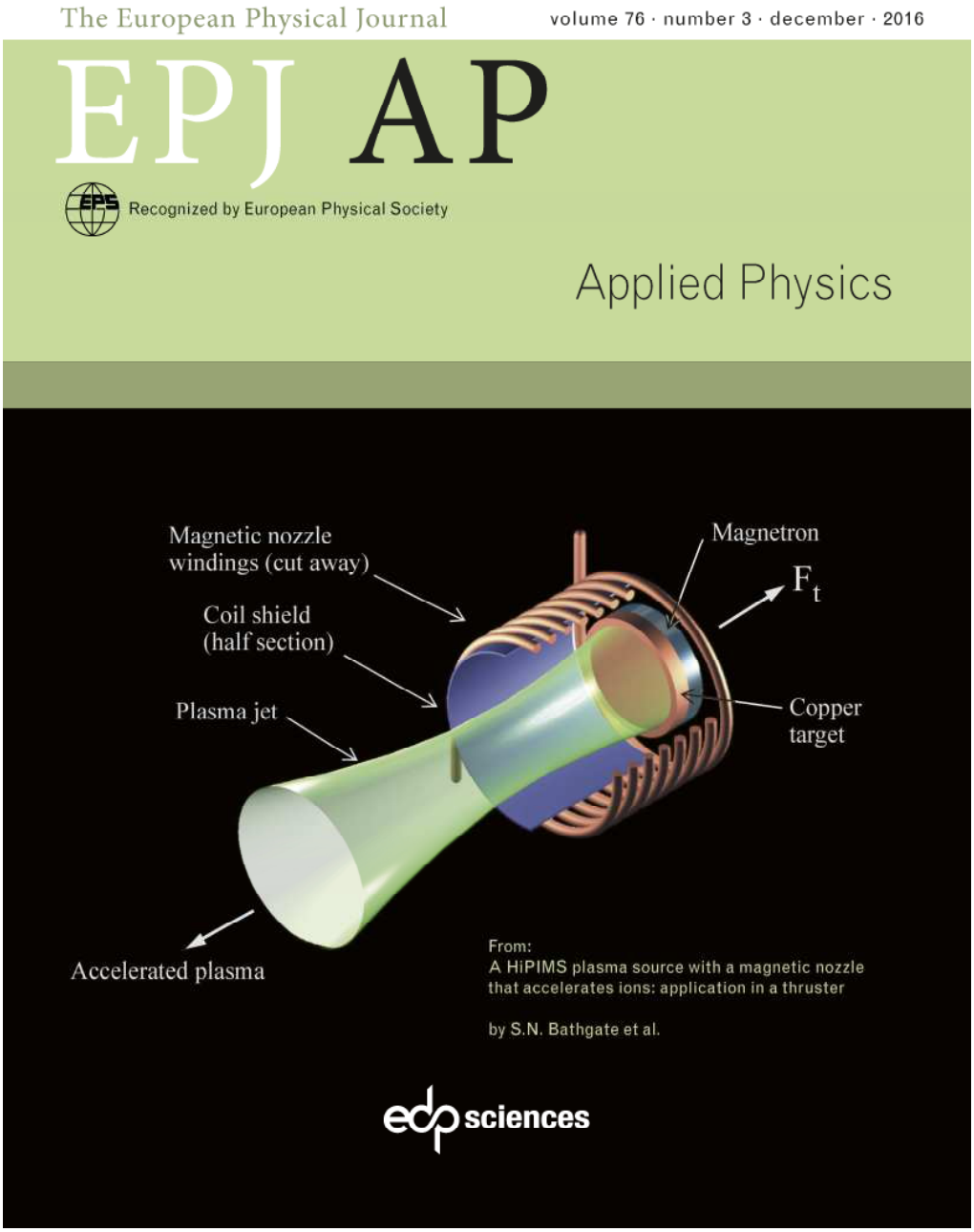

2. S.N. Bathgate, M. M. M. Bilek and D.R. McKenzie, "Electrodeless plasma thrusters for spacecraft: a review" , *Plasma Sci. Technol. 19 (2017) 083001 (24pp)*

3. S. N. Bathgate, M. M. M. Bilek and D. R. McKenzie, *"A thruster using magnetic reconnection to create a high-speed plasma jet"*, to be submitted to European Physical Journal – Applied Physics 2017

1 Introduction

An historical introduction and outline of the contents of the thesis.

Rockets first appeared in Medieval China as the result of the work of 9th Century alchemists who, seeking an elixir of life, mixed sulphur, saltpetre (potassium nitrate) and charcoal to create what became known in the West as gunpowder, used initially for bombs and later as a propellant for guns and then rockets [Needham et al 1986 [1]]. Although the first recorded use of rockets was in China in 1264, it was not until the work of Isaac Newton in the 17th Century that the basic physics – although not the chemistry - was properly understood. Following Newton, a further 200 years elapsed before the Russian Konstantin Tsiolkovsky demonstrated the importance of the exhaust velocity as a determinant of a rocket's performance. Tsiolkovsky derived the rocket equation (Eq. 1), a fundamental result that he published in 1903 [Tsiolkovsky 1903 [2]] :

$$\Delta v = v_e \, ln \frac{m_i}{m_f} \qquad \text{Eq. 1}$$

Where Δv = the rocket's velocity increment resulting from the expulsion of propellant,

v_e = the exhaust velocity,

$\frac{m_i}{m_f}$ = the ratio of the rocket's initial mass m_i to its final mass m_f that includes the payload.

Tsiolkovsky subsequently proposed the use of electricity for propulsion, a suggestion that had its origins in the discoveries of J.J. Thompson [Thompson 1897 [3]] who determined the velocities of cathode rays - now recognized as electrons. Tsiolovsky saw that those particles were travelling 6000 to 20,000 times faster than the velocity of gases produced by combustion [Choueri 2004 [4]].

Working at a slightly earlier date although initially unpublished, the American rocket pioneer Robert Goddard filed a patent for an electrical propulsion device [Goddard 1920 [5]] entitled "Method of and means for producing electrified jets of gas" (U.S. Patent 1,363,037) that described an apparatus that was intended to produce a high velocity stream of ionized mercury vapour (fig. 1). Goddard, who would go on to construct the first liquid fuel rockets, similarly recognized that electrical devices could produce much greater exhaust velocities than were obtainable with chemical rockets. Although he constructed small-scale electrostatic ion thrusters, technical limitations ruled out practical applications for his designs and he instead devoted his time to developing chemical rockets.

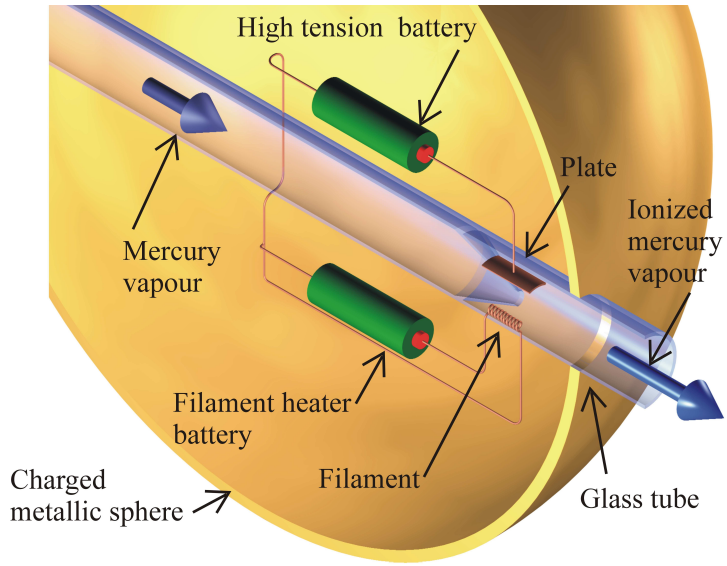

Figure 1 . Schematic of Robert Goddard's apparatus for producing a high velocity stream of ionized mercury vapor. The mercury vapor is ionized by electron bombardment from a current passing between a hot filament and a cathode at a constriction in a glass tube.

Other investigators such as the Russian Valentin Petrovich Glusko built and tested the first electrothermal thrusters at the Leningrad Gas Dynamics Laboratory between 1929 and 1933 [Barnett 1990 [6]] and Hermann Oberth, extending the work of Tsiolkovsky and others, discussed electric propulsion in his book "*Wege zur Raumschiffahrt"* (The Road to Space Ship Travel) [Oberth 1929 [7]]. The book's last chapter "*Das elektrische Raumschiff*" (The Electric Spaceship) was devoted to electrostatic ion thrusters. Although many investigators contributed to theoretical developments after Tsiolkovsky, Goddard, Oberth and Glusko it was not until early in 1958 that the first tungsten gridded caesium ion thruster was tested by Stavisskii in the former Soviet Union [Heller 1962 [8]]. Later that year, a similar device was tested at the Rocketdyne division of North American Aviation [Stuhlinger 1964 [9]]. Following that success and others, in 1960 NASA established a program to develop electric propulsion systems, as did the former Soviet Union. By 1964 the Space Electric Rocket Test 1, a caesium gridded ion thruster with a hollow cathode neutralizer, built at the then NASA Lewis Research Centre (now NASA John H. Glenn Research Centre), operated for half an hour during a sub-orbital flight [Sovey et al 2001 [10]]. In the same year, pulsed plasma thrusters used for attitude control were installed on the Soviet Zond-2 Mars probe [Kazeev et al 2009 [11]]. Since that time a large number of devices have been tested and ion thrusters similar to Goddard's original proposal have been deployed operationally (for example Deep Space 1 [Marcucci and Polk 2000 [12]], Dawn [Brophy 2011 [13]], GOCE [Wallace et al 2011 [14]]).

Hall thrusters, developed in the former Soviet Union in the 1960s, use a radial magnetic field to produce an azimuthal Hall current that retards the electrons that flow towards the internal anode from an external cathode. The retarded electrons both ionize the propellant gas and produce an electric field that accelerates the resulting ions while other electrons emitted by the cathode neutralize the

accelerated ions [Goebel and Katz 2008 [15]]. Hall thrusters are therefore regarded as grid-less electrostatic devices although they have cathodes that are subject to erosion. SPT-60 Hall thrusters were first used on a Russian Meteor satellite in 1976 [Kim et al 2001 [16]] and contemporary Hall thrusters are routinely used on Russian communications satellites for station keeping [Gorshkov et al 2001 [17]]. They have also been deployed on American and European spacecraft [Kilter and Karlsson 2004 [18]].

The development of plasma thrusters has been the subject of considerable interest in space engineering and by 2003, at least 15 different research institutions in the United States were investigating electric thruster designs. Many establishments in different parts of the world are presently conducting similar research and development programs. While much of the development of these devices has been conducted by engineers, physicists continue to produce new types of plasma thrusters based on phenomena that, like Michael Faraday's first electric motor, may produce effects not at first apparent from a particular arrangement of magnetic fields and electric currents.

The aim of the work reported in this thesis has been to explore arrangements of magnetic fields and electric currents to create novel plasma thrusters that are more efficient and less complex than existing designs.

Two original devices are discussed, firstly a thruster that uses a magnetic nozzle in combination with a High Power Impulse Magnetron Sputtering source (HiPIMS) to produce a jet of copper plasma and secondly, a thruster that uses the phenomena of magnetic reconnection that occurs between opposing magnetic fields in a plasma to produce a plasma jet. While HiPIMS has been normally employed to create thin films, the use of a solenoidal magnetic field to accelerate and focus the ions produced by that source has not been previously investigated as a means of creating a thruster.

Similarly, magnetic reconnection has been studied for decades by geophysicists interested in the interactions between the solar wind and the Earth's magnetosphere and by astronomers investigating solar flares and related occurrences. Despite that effort, so far there has been little interest in exploiting the phenomena as a means of producing high-speed plasmas in a thruster despite the evidence of jets in those environments.

Isaac Newton wrote that "It is not number of experiments but weight [of those experiments] to be regarded and where one will do, what need of many?" In contrast, the experimental reports of his older Royal Society colleague, Robert Boyle, were produced in such excruciating detail that his readers could be regarded as "virtual witnesses" to his experiments with the purpose that his accounts might "keep the reader from distrusting" the outcomes. I hope that this work, one of delving into the physics of plasma thrusters, strikes a balance between those extremes.

2 Plasma thruster metrics

A description of the principal metrics used in comparing the performance of plasma thrusters.

Various metrics are employed to enable comparisons to be made between thrusters that use different operating principles. Thrust is the most obvious metric although not necessarily the most informative and several other measures that relate more directly to mission requirements often have greater relevance. The most significant metrics are discussed in the following sub-sections: thrust, specific impulse, thrust efficiency, specific mass, propulsive efficiency and the mission difficulty parameter together with thruster lifetime, the advantage enjoyed by electrodeless thrusters.

2.1 Thrust F_t

Spacecraft are propelled by the directed expulsion of high velocity particles, typically in the form of a gas or plasma. According to Newton's Second Law, thrust is defined as the instantaneous force on a spacecraft that is proportional to the vector sum of the time rate of change of the momenta of the expelled propellant particles *i*. If the instantaneous rate of expulsion of propellant is $\dot{m}_p$ and the propellant is expelled at a velocity v_e, relative to the spacecraft, then the thrust is given by:

$$F_t = -\sum_i \dot{m}_p v_e \qquad \text{Eq. 2}$$

Where F_t is the thrust in Newtons.

2.2 Specific impulse I_{sp}

Specific impulse, I_{sp}, is usually considered to be the primary figure of merit of a thruster [Ahedo 2011 [19]] and is defined as the value of the thrust divided by the weight of propellant expelled in unit time. Specific impulse is a measure of the capacity of a propulsion system to impart a velocity increment Δv to a spacecraft and through Tsiolkovsky's rocket equation (Eq. 1) and the exhaust velocity v_e, specific impulse largely determines the practicality of a mission.

$$I_{sp} = \frac{F_t}{\dot{m}_p\, g_0} = \frac{v_e}{g_0}(s) \qquad \text{Eq. 3}$$

Where g_0 is the acceleration due to gravity at Earth's surface.

For example, a spacecraft producing a thrust of 9.81 newtons consuming 1 kilogram weight of propellant in 450 seconds will have an I_{sp} of 450 seconds.

An $I_{sp} \geq 3000s$, corresponding to an energy of 4.5eV per atomic mass unit of propellant, is considered to be a minimum requirement for many remote planetary missions [Cohen et al 2006 [20]].

2.3 Thrust efficiency η_t

The thrust efficiency η_t of a rocket or thruster is the secondary figure of merit and is a measure of the effectiveness of the propulsion system in converting the energy input (chemical, electrical or thermal) to the directed kinetic energy of the exhaust jet. Thrust efficiency is less important than specific impulse as a performance metric for electric thrusters since propellant mass rather than energy, typically produced by solar photovoltaic panels, is usually a mission's limiting factor.

$$\eta_t = \frac{directed\ kinetic\ energy\ in\ jet}{energy\ from\ power\ supply} \qquad \text{Eq. 4}$$

Simple devices such as Teflon pulsed plasma thrusters may have a low thrust efficiency (typically 5%) but are still regarded as useful because of their simplicity and high I_{sp} (up to 760s) compared to chemical thrusters [Markusic et al 2005 [21]]. The following table summarizes typical specific impulse, thrust efficiencies and thrusts and impulses of some deployed and developing electric thrusters (Table 1). Note that the specific impulse for the most powerful chemical thrusters (H_2-O_2) is limited to approximately 450s [Rapp 1990 [22]].

Thruster type	**Electrodes**	**I_{sp}(s)**	**Thrust efficiency η_t**	**Thrust or impulse**	**Reference**
Pulsed plasma (Teflon)	Y	240-760	2-9%	0.1 mN-s	Markusic et al 2005 [21]
Gridded ion	Y	7650	77%	0.43N	Patterson et al 2009 [23]
Hall	Y	1600	50-60%	2.5-12 x 10^{-3} N	Smirnov et al 2002 [24]
Magneto-plasma-dynamic	Y	3670	38.8%	~250 x 10^{-3} N	Krulle et al 1998 [25]
Inductively heated arcjet (TIHTUS)	Y	2000	29%	6.0 N	Bohrk and Auweter-Kurtz 2005 [26]
Cathodic arc	Y	>1000	-	-	Neumann et al 2009 [27]
Mini Helicon	N	1000 - 4000	~20%	~10 x 10^{-3} N	Batishchev 2009 [28]
Pulsed Inductive	N	5500	50%	75.5 mN-s	Polzin and Reneau 2009 [29]
Magneto-plasma (VASIMR)	N	3400	56%	3.6±0.2 N	Longmier et al 2011 [30]
Electron Cyclotron Resonance	N	429 (Xe)	3.5%	0.86 x 10^{-3} N	Jarrige et al 2013 [31]
Electrodeless Lorentz Force (ELF)	N	1000-6000	50+%	1.0 N (average)	Slough et al 2009 [32]

Table 1 Specific impulses, thrust efficiencies and thrusts or impulses of contemporary electric thrusters, with and without electrodes, deployed and experimental.

2.4 Specific mass

Specific mass is given as kg/kW and is the ratio of the mass of a propulsion system (including components such as the fuel system and tanks, solar panels, power supply and the thruster itself) to the power delivered to the exhaust. Although a propulsion system may have a high specific impulse and thrust efficiency, a high specific mass will negate those advantages by reducing the proportion of the total mass of a spacecraft that can be used for payload and structures.

2.5 Propulsive efficiency ε_p

The propulsive efficiency ε_p of a rocket is the ratio of the rate of increase of the kinetic energy delivered to the rocket by the thrust of its engine, (i.e. the thrust power P_t) to the total power that includes the power lost to the exhaust jet P_e, that is:

$$\varepsilon_p = \frac{P_t}{P_t + P_e} \qquad \text{Eq. 5}$$

The thrust power, P_t is the work done on the rocket in unit time and is given by the rate of expulsion of the propellant mass, $\dot{m}_p$ multiplied by the velocity of the expelled propellant, v_e, relative to the rocket and by the velocity of the rocket, v_r, relative to the frame of reference.

$$P_t = \dot{m}_p v_e v_r \qquad \text{Eq. 6}$$

A low propulsive efficiency that results when the exhaust velocity is high relative to the rocket in the rocket's frame of reference means that most of the energy produced by a power supply in an electric thruster is lost to the exhaust rather than being imparted to the spacecraft. A high propulsive efficiency which results from a low exhaust velocity relative to the rocket in the rocket's frame of reference is not necessarily an advantage since Tsiolkovsky's rocket equation (Eq. 1) shows that a low exhaust velocity limits the maximum velocity increment or payload mass.

Since the thrust power P_t is a function of the rocket's velocity it is therefore dependent on the rocket's frame of reference so is not a mission-independent measure of performance. For example, as the rocket passes from the frame of reference of the Earth to the frame of reference of the Sun, the thrust power changes.

The exhaust power P_e lost as energy in the exhaust is the kinetic energy in the exhaust expelled per unit time and is given by:

$$P_e = \frac{1}{2}\dot{m}_p (v_e - v_r)^2 \qquad \text{Eq. 7}$$

The propulsive power P_p is then:

$$\begin{aligned} P_p &= P_t + P_e = \dot{m}_p v_e v_r + \frac{1}{2}\dot{m}_p (v_e - v_r)^2 \\ &= \dot{m}_p v_e v_r + \frac{1}{2}\dot{m}_p (v_e^2 + v_r^2 - 2 v_e v_r) \\ &= \frac{1}{2}\dot{m}_p (v_e^2 + v_r^2) \end{aligned} \qquad \text{Eq. 8}$$

The propulsive efficiency ε_p is then:

$$\varepsilon_p = \frac{thrust\ \ power}{propulsive\ \ power} = \frac{P_t}{P_p} = \frac{\dot{m}_p v_e v_r}{\frac{1}{2}\dot{m}_p({v_e}^2 + {v_r}^2)} = \frac{2(v_r/v_e)}{1+(v_r^2/v_e^2)} \qquad \text{Eq. 9}$$

Or

$$\varepsilon_p = \frac{2S_p}{1+S_p^2} \qquad \text{Eq. 10}$$

Where $S_p = \frac{v_r}{v_e}$ is the ratio of the rocket velocity to the exhaust velocity in the same frame of reference.

The variation in propulsive efficiency with the velocity ratio is shown in the following chart (fig. 2) calculated from Eq. 10 [Rathore 2010 [33]].

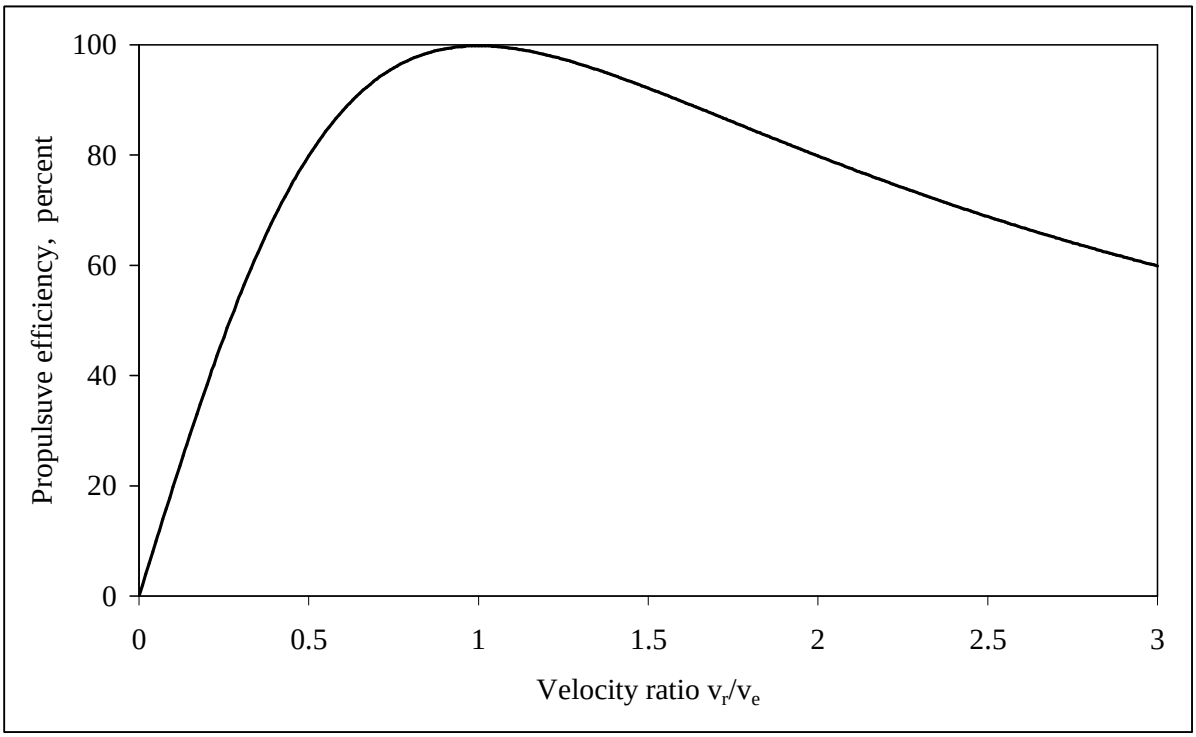

Figure 2 Variation of propulsive efficiency with velocity ratio v_r / v_e calculated using Eq. 10. The chart shows that the propulsive efficiency (P_t/P_p) is at a maximum when the magnitudes of the velocities of the exhaust jet and the rocket are equal ($|v_e| = |v_r|$) in the same frame of reference. Although a rocket has no kinetic energy at lift-off from the Earth's surface and the propulsive efficiency is zero, the energy input produces a force that accelerates the rocket and the propulsive efficiency improves as the rocket gains velocity.

When $|v_e| = |v_r|$ in the same frame of reference, the residual kinetic energy and the velocity of the jet v_e with respect to the frame of reference is zero and the exhaust gases stand still in space. (fig. 3), [Sutton and Biblarz 2001 [34]].

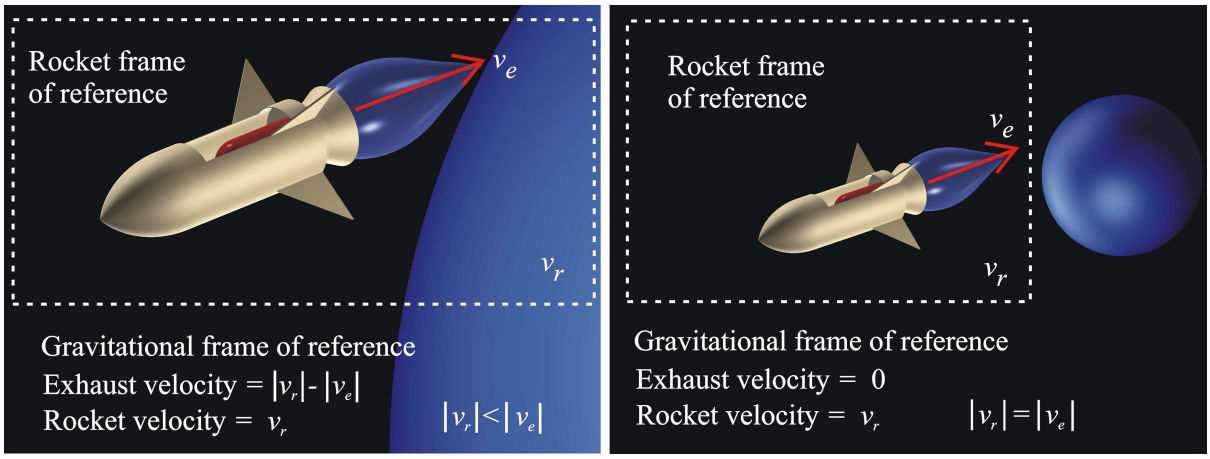

Figure 3 The rocket moves as an independent frame of reference (dotted outline) with the expelled propellant moving away from the rocket at a velocity v_e relative to the rocket. As the rocket accelerates, the velocity v_r of its frame of reference increases with respect to the gravitational frame of reference of the relevant gravitating body. When $|v_r| < |v_e|$ the exhaust moves with respect to the gravitational frame of reference at a velocity $|v_r| - |v_e|$ and power that would otherwise drive the rocket is lost to the exhaust. When $|v_r| = |v_e|$ the velocity of the exhaust with respect to the gravitational frame of reference is zero, no power is lost to the exhaust and all of the energy in the exhaust propels the rocket.

When $|v_e| >> |v_r|$, in the same reference frame, the propulsive efficiency is low and since much of the energy produced by the power supply is absorbed by the propellant and not imparted to the spacecraft, a large power supply is required to produce sufficient thrust to accelerate the vehicle. Designers of interplanetary missions that start in low earth orbit and are equipped with plasma thrusters with a high exhaust velocity relative to the spacecraft face that difficulty. In that situation, a large proportion of the energy generated by the propulsion system is lost in the exhaust until the rocket reaches a velocity comparable to the absolute magnitude of the exhaust velocity in the same frame of reference. The VASIMR (Variable Specific Impulse Magnetic Rocket) is an attempt to partly overcome this problem by varying the exhaust velocity [Arefiev and Breizman 2004 [35]] . For an interplanetary mission, VASIMR would operate at a thrust level sufficient to escape Earth's gravitational influence and by increasing v_e after escape, increase I_{sp} and reduce the consumption of propellant for the duration of the mission.

2.6 The rocket equation for power limited thrusters.

Using specific impulse I_{sp}, (Eq. 3), the ideal rocket equation (Eq. 1), can be expressed in exponential form as [Gilland et al 2004 [36]]:

$$\frac{m_f}{m_i} = e^{-\frac{\Delta v}{g_0 I_{sp}}} \qquad \text{Eq. 11}$$

This relationship is true for any propulsion system and demonstrates that for a given Δv, a high I_{sp} (a characteristic of most plasma thrusters) enables the construction of spacecraft with a high ratio $\frac{m_f}{m_i}$ of final mass – including payload - to initial mass. The relationships between this ratio, the velocity increment Δv and the specific impulse I_{sp} are illustrated in fig. 4. Five velocity increments are shown as lines on the plot. These lines show that for a mission with a high mass ratio $\frac{m_f}{m_i} \to 1$ and a large velocity increment Δv, a high specific impulse is required. Also illustrated are points corresponding to the mass ratios of selected missions with plasma propulsion systems as a function of specific impulse together with the velocity increments of those missions.

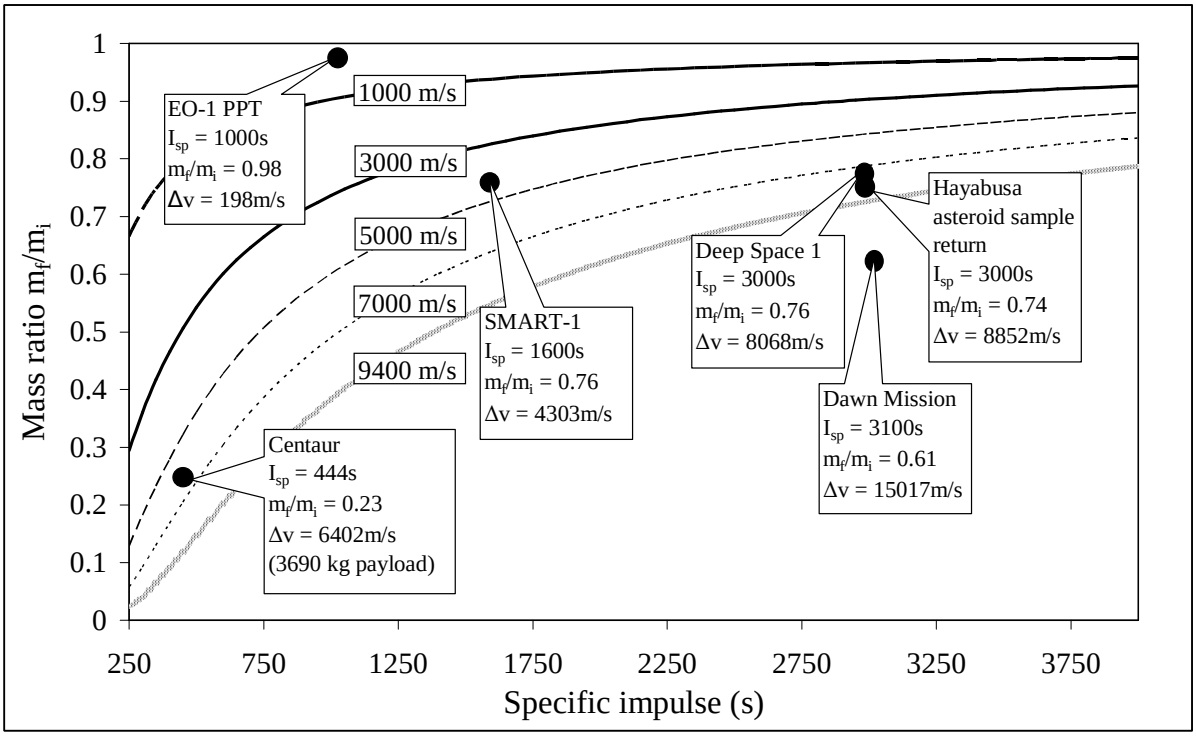

Figure 4 The curves show the mass ratios m_f/m_i as a function of specific impulse for different velocity increments Δv (1000, 3000, 5000, 7000 and 9400m/s (low – earth orbit)) (calculated with Eq. 11). Shown are SMART-1 (Hall thruster) [Foing et al 2003 [37]], Deep Space 1 (gridded ion) [Rayman et al 2000 [38]], Hayabusa (gridded ion) [Yoshikawa et al 2006 [39]], Dawn (gridded ion) [Brophy et al 2006 [40]], EO-1 (Pulsed Plasma Thruster) [Benson et al 1999 [41]] and for comparison, a chemical rocket, the Centaur (H_2-O_2 in vacuum) [Dawson and Bowles 2004 [42]].

2.7 The mission difficulty parameter *J*

The ideal rocket equation (Eq. 1) for a rocket with a constant exhaust velocity, such as a typical plasma thruster, may be expressed in exponential form as:

$$m_f = m_i e^{-\frac{1}{v_e}\int_0^t a_r\, dt} \qquad \text{Eq. 12}$$

Where a_r is the acceleration imparted to the vehicle and $\Delta v = \int_0^t a_r\, dt$ is the velocity increment.

While the thrust developed by plasma thrusters is limited by the maximum power produced by their power supplies, typically solar photovoltaic panels, the velocity increment Δv may be significantly greater than that achievable with chemical rockets because of the much higher exhaust velocity of plasma thrusters. In addition, plasma thrusters are not constrained by a fixed supply of energy. The rocket equation for such power-limited spacecraft operating with constant power P_s, over a propulsion time t_p, may be derived by combining the equation for the thrust of a rocket [Melbourne 1961[43]]:

$$F_t = -\dot{m}_p\, v_e \qquad \text{Eq. 13}$$

With the equation for the power in the exhaust:

$$P_e = \frac{1}{2}\dot{m}_p v_e^2 \qquad \text{Eq. 14}$$

And with the relationship between the power in the exhaust P_e and the output of the power supply P_s:

$$P_e = \varepsilon_i P_s \qquad \text{Eq. 15}$$

The power delivered to the propellant mass is a function of the kinetic energy of the jet and of the time t and is given as:

$$P_e(t) = \frac{1}{2}\dot{m}_p v_e(t)^2 \qquad \text{Eq. 16}$$

The momentum imparted to the propellant produces a thrust F_t which results in an acceleration given by:

$$a_r(t) = -\frac{F_t(t)}{m_r(t)} = -\frac{\dot{m}_r v_e(t)}{m_r(t)} \qquad \text{Eq. 17}$$

Note that $\dot{m}_r$ is negative so that the direction of the acceleration is positive provided that the minus sign is introduced in Eq. 17. Note that $\dot{m}_r = \dot{m}_p$ since there is no other loss of mass from the rocket.

Equations 16 and 17 may be combined to eliminate the exhaust velocity v_e to give:

$$\frac{a_r^2(t)}{2P_e(t)} = -\frac{\dot{m}_r}{m_r(t)^2} = -\frac{dm_r}{dt}\frac{1}{m_r^2(t)} = -\frac{d}{dt}\left(\frac{1}{m_r(t)}\right) \qquad \text{Eq. 18}$$

Integrating this between 0 and t_p, the propulsion time, gives:

$$\frac{1}{m_r(t_p)} = \frac{1}{m_r(0)} + \frac{1}{2P_e(t)}\int_0^{t_p} a_r^2\,dt \qquad \text{Eq. 19}$$

A rocket propelled by a plasma thruster consists of a payload mass m_{pl}, a power supply mass m_{ps}, a structural mass m_s and a propellant mass m_p. The initial mass of the rocket $m_r(0)$, is the sum of these components:

$$m_r(0) = m_i = m_{pl} + m_{ps} + m_s + m_p \qquad \text{Eq. 20}$$

After a time t_p when the propellant mass m_p has been expelled, the final rocket mass $m_r(t_p)$ is:

$$m_r(t_p) = m_f = m_{pl} + m_{ps} + m_s \qquad \text{Eq. 21}$$

Using this result in Eq. 19 and setting P_e constant we have:

$$\frac{1}{m_f} = \frac{1}{m_i} + \frac{1}{2P_e}\int_0^{t_p} a_r{}^2\,dt = \frac{1}{m_i} + \frac{J}{2P_e} \qquad \text{Eq. 22}$$

Where the integral $J = \int_0^{t_p} a_r^2\,dt$ is termed the *mission difficulty parameter*.

This result shows that for a power limited system operating with constant power, it is desirable to minimize the time integral of the square of the acceleration [Edelbaum 1969 [44]].

A relationship between J and Δv can be derived from the exponential form of the rocket equation which can be rewritten as:

$$m_i - m_f = m_f \left(e^{\Delta v / v_e} - 1 \right) \qquad \text{Eq. 23}$$

Eq. 22 may be written as:

$$\frac{1}{m_f} - \frac{1}{m_i} = \frac{m_i - m_f}{m_i m_f} = \frac{1}{2P_e} \int_0^{t_p} a_r{}^2 dt = \frac{J}{2P_e} \qquad \text{Eq. 24}$$

And then combined with Eq. 23 to give:

$$J = \frac{2P_e}{m_i} \left(e^{\Delta v / v_e} - 1 \right) \text{ m}^2/\text{s}^3 \qquad \text{Eq. 25}$$

J may be used to evaluate the ratio R of distance versus trip time for a mission in terms of the total trip time T and the propulsion time T_p [Moeckel 1972 [45]].

1. Flyby: $R = \sqrt{\frac{J}{T_p}} \left(T_p T - \frac{1}{2} T_p^2 \right)$

2. Rendezvous: $R = \frac{1}{2} \sqrt{\frac{J}{T_p}} \left(T_p T - \frac{1}{2} T_p^2 \right)$

3. Round trip: $R = \frac{1}{8} \sqrt{\frac{J}{T_p}} \left(T_p T - \frac{1}{2} T_p^2 \right)$

J may be plotted as a function of velocity increment and exhaust velocity for a spacecraft of arbitrary mass and power (fig. 5).

The plot demonstrates the advantage of the high exhaust velocity produced by plasma thrusters as a means of reducing the mission difficulty parameter.

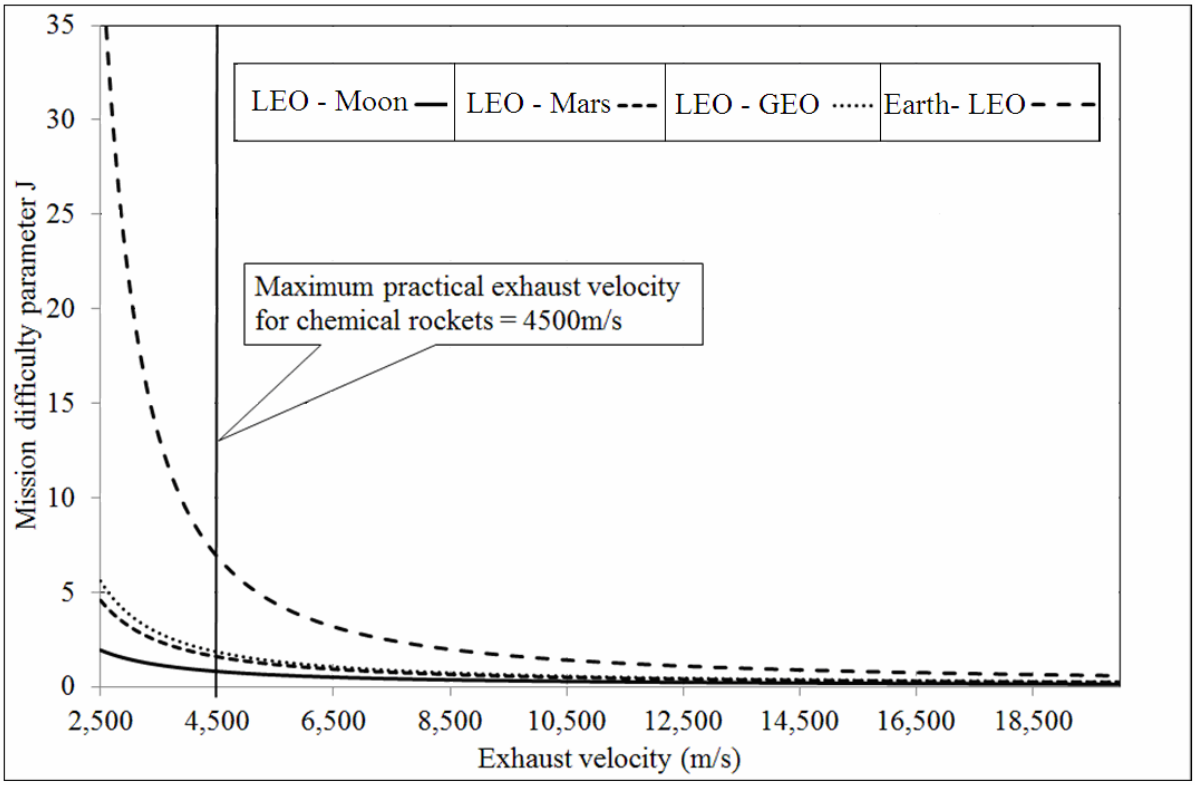

Figure 5 Plot of mission difficulty parameter *J* as a function of exhaust velocity for various missions: From low Earth orbit (LEO) to the Moon (Δv = 2.7km/s [Ward 2010 [46]]), from LEO to Mars Transfer (Δv = 4.3km/s [Woodcock 1995 [47]]) , from LEO to Geosynchronous orbit (GEO) (Δv = 4.72km/s [Newton's formula]) and from the Earth's surface to LEO (Δv = 9.3 km/s [Sutton and Biblartz 2001[34]]). In this example, the spacecraft has an exhaust power of 500 watts and a mass of 1000kg.

2.8 Plasma thruster lifetime

Sputtering causes grid erosion in gridded ion thrusters, electrode erosion in magneto-plasma-dynamic thrusters and wall erosion in Hall and other types of thrusters. Sputtering also erodes the cathodes that provide the electrons that neutralize the exhaust in thrusters that produced charged ion beams. That erosion gradually degrades the performance of those devices as well as limiting their maximum lifetimes (Table 2). At the power levels presently employed – several kilowatts – erosion has not caused serious problems but as missions that require higher power and greater thrust as well as longer duration are contemplated, grids, walls and cathodes will be exposed to more intense ion fluxes as larger masses of propellant are accelerated. Electrodeless thrusters will become more important since erosion is not the life-limiting factor in such devices.

Thruster type	Power (kW)	Lifetime (hours)	Reference
Gridded ion (NSTAR)	2.3	~30,000	Rovey and Gallimore 2008 [147]
Hall (BPT-4000)	4.5	10,400 ("zero" erosion)	de Grys et al 2010 [48]
Applied Field Magnetoplasmadynamic	30	8,000-10,000	Gorshkov et al 2007 [49]

Table 2 Reported durability of typical plasma thrusters with electrodes.

2.9 The effect of specific impulse on the mass ratio of a mission $\frac{m_f}{m_i}$

Although the specific impulse of plasma thrusters is generally much larger than those of chemical thrusters that have a maximum specific impulse of approximately 450 seconds, (see Table 1), the thrust of such devices (0.01 to about 1.0N) is often orders of magnitude less than that of chemical rockets. That limits the use of plasma thrusters to spacecraft that have been boosted to orbital or escape velocity by chemical rockets. Nonetheless, plasma thrusters have significant advantages over chemical rockets as a space propulsion system as can be seen in the following analysis.

Using specific impulse I_{sp}, (Eq. 3), the ideal rocket equation (Eq. 1), can be expressed in exponential form as [Gilland et al 2004 [50]]:

$$\frac{m_f}{m_i} = e^{-\frac{\Delta v}{g_0 I_{sp}}} \qquad \text{Eq. 26}$$

This relationship is true for any propulsion system and demonstrates that for a given Δv, a high I_{sp} (a characteristic of most plasma thrusters) enables the construction of spacecraft with a high ratio $\frac{m_f}{m_i}$ of final mass – including payload - to initial mass. The relationships between this ratio, the velocity increment Δv and specific impulse I_{sp} are illustrated in fig. 6. Five velocity increments are shown as lines on the plot. These lines show that a high specific impulse enables a mission with a high mass ratio, $\frac{m_f}{m_i} \to 1$, and a large velocity increment Δv. Also illustrated are points corresponding to the mass ratios of selected missions with plasma propulsion systems as a function of specific impulse together with the velocity increments of those missions. Shown are SMART-1 (Hall thruster) [Foing et al 2003 [51]], Deep Space 1 (gridded ion) [Rayman et al 2000 [12]], Hayabusa (gridded ion) [Yoshikawa et al 2006 [52]], Dawn (gridded ion) [Brophy et al 2006 [13]], EO-1 (Pulsed Plasma Thruster) [Benson et al 1999 [53]] and for comparison, a chemical rocket, the Centaur (H_2-O_2 in vacuum) [Dawson and Bowles 2004 [54]].

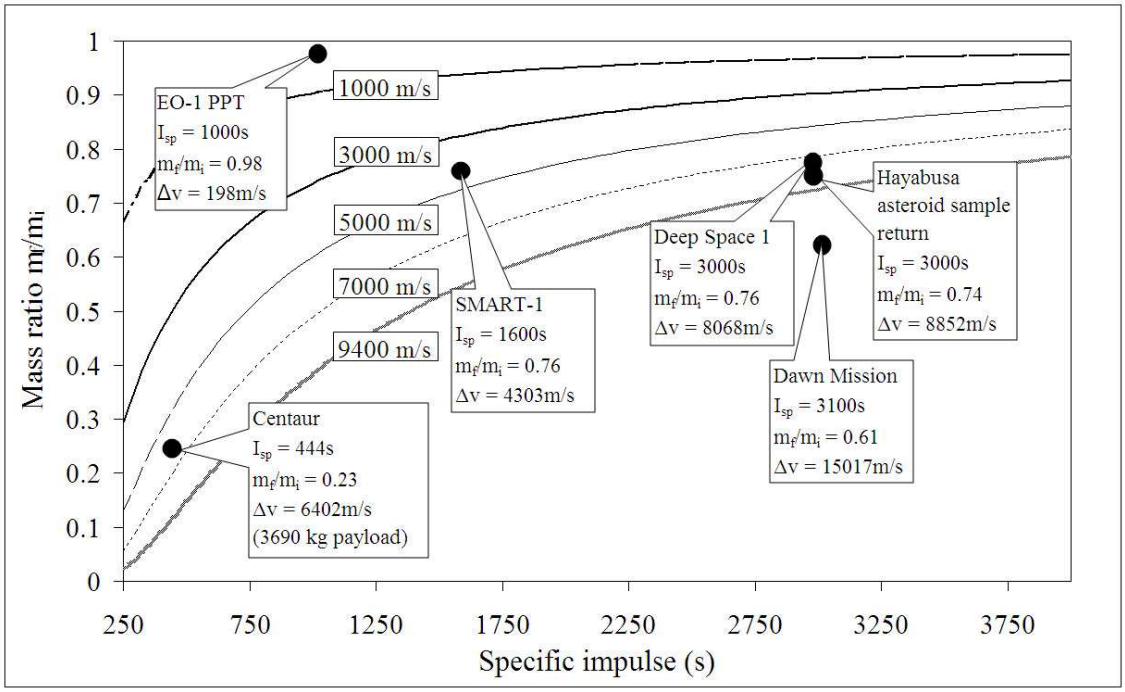

Figure 6 The curves show the mass ratios m_f/m_i as a function of specific impulse calculated from equation 28 for different velocity increments Δv , 1000, 3000, 5000, 7000 and 9400 m/s (9400 m/s = low – earth orbit)

2.10 Trade-offs between metrics

For any mission the orbital requirements are (1), the required velocity increment Δv , (2), the time to complete an orbital manoeuvre Δt and (3), the payload mass m_{pl}. For a propulsion system, the principal determining metrics are: thrust F_t,, specific impulse I_{sp}, propulsion system power P_s and thrust efficiency η_t which can be expressed as:

$$\eta_t = \left(\frac{g_0}{2}\right)\left(\frac{F_t}{P_s}\right) I_{sp} \qquad \text{Eq. 27}$$

While the orbital manoeuvre time which can be expressed as:

$$\Delta t = \left(\frac{m_{pl}}{P_s}\right)\left(\frac{(g_0 I_{sp})^2}{2\eta_t}\right)\left(e^{\left(\frac{\Delta v}{g_0 I_{sp}}\right)} - 1\right) \qquad \text{Eq. 28}$$

These relationships between the mission parameters and those of the spacecraft propulsion system show that there is a capacity for trade-offs between the various parameters and it is possible to optimise factors such as transit time, specific impulse and payload mass for a particular mission. [Brown et al 2009 [55]].

3 Basic physics of plasma thrusters and related devices

A discussion of the mechanisms underlying the operation of plasma thrusters.

Plasma thrusters may use electrostatic forces, as in gridded ion thrusters, magnetic forces as in magneto-plasma-dynamic thrusters or a combination of magnetic and electrostatic forces as in Hall thrusters. The mechanism of a plasma thruster involves two distinct processes: (1) The creation of the plasma and (2), its acceleration and detachment. These processes are discussed in the following sections.

3.1 Plasma creation

Plasma for thrusters may be produced by a variety of mechanisms:

1. Through the effect of Faraday's Law ($e = -N \, d\Phi/dt$) where a changing magnetic flux Φ induces an electric field e that can ionize a low-pressure gas by stripping electrons from atoms and molecules. Radio frequency energy is typically used with various kinds of antennae and this process is a useful electrodeless mechanism for producing plasma from gaseous propellants. Helicon Plasma thrusters, Pulsed Inductive thrusters, Inductive Thermal thrusters and other devices exploit this mechanism which is the most commonly used means of producing plasmas in electrodeless plasma thrusters (fig 7).

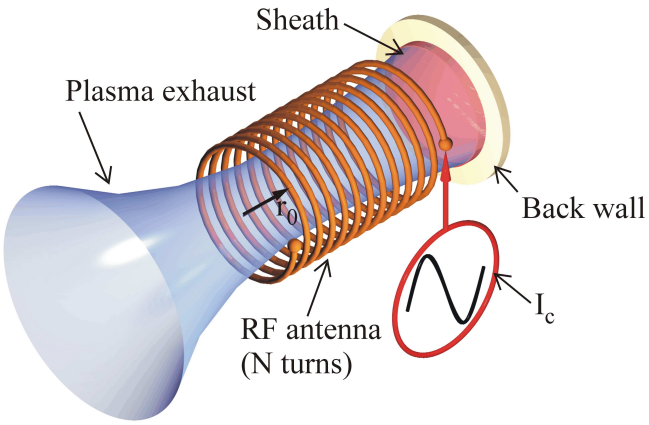

Figure 7 Simple open-ended plasma thruster showing RF antenna of N turns, RF input current I_c, sheath, back wall, and plasma exhaust. Thrust is produced by the reaction of the plasma through the sheath against the back wall which may be eroded by ion bombardment [Fruchtman 2008 [56]] although the device does not have electrodes that may also be subject to erosion.

2. Electron Cyclotron Resonance (ECR) ion sources are electrodeless devices that produce ions by the application of Faraday's law but increase its effectiveness by feeding microwaves at the cyclotron resonant frequency into a gas in a solenoidal magnetic field [Jarrige et al 2013 [31]]

(fig. 8). Electrons are heated to high temperatures and gyrate around the magnetic field lines at a resonant frequency ω_{ce} given by:

$$\omega_{ce} = \frac{eB}{m_e} \qquad \text{Eq. 29}$$

Where e = electron charge, B = magnetic field strength and m_e = electron mass.

The electrons then collide inelastically with neutral gas atoms or molecules and that process leads to the ionization of the gas.

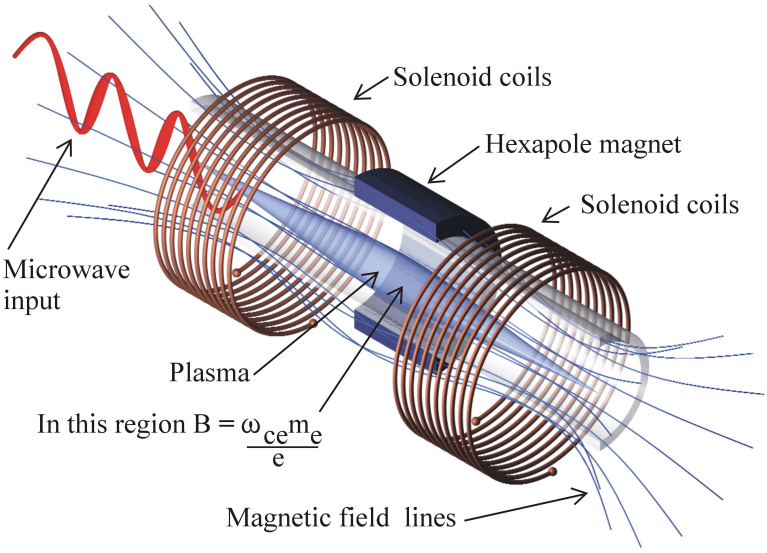

Figure 8 Sectioned electron cyclotron resonance plasma source. The electrons are heated to a high temperature by resonant heating by the microwave beam and collisions between electrons and neutrals lead to a high ionization ratio. Plasma produced by this electrodeless mechanism can be accelerated by Lorentz forces in a magnetic nozzle or by a traveling magnetic field.

3. By a DC potential to produce a low current density discharge known as a glow discharge where plasma is produced by the bombardment of a gas by electrons and ions that are accelerated by the potential between electrodes. Ion sources for gridded ion thrusters may use this mechanism that requires electrodes.

4. By a high current density discharge or arc that may be initiated when the cathode becomes sufficiently hot that it emits electrons thermionically. Otherwise, an arc may be initiated as a glow discharge. Magneto-plasma-dynamic and cathodic arc thrusters are devices with electrodes that produce ions by this means.

3.2 Plasma acceleration

Once created, plasma has to be accelerated to produce thrust. There are a number of mechanisms that can be used for this purposes, some more practical than others. The following sections describe mechanisms that have been used or proposed as a means of accelerating plasma in electrodeless thrusters.

3.2.1 Lorentz forces

Aside from any thrust that may arise from the pressure of the plasma against the thruster structure, the propulsion force or thrust $\mathbf{F}_t$ is generated in the majority of plasma thrusters by body forces that are described by the Lorentz equation:

$$\mathbf{F}_t = q\mathbf{E} + q(\mathbf{v} \times \mathbf{B}) \qquad \text{Eq. 30}$$

Where q = the charge on ions, $\mathbf{E}$ = the electric field, if any, $\mathbf{v}$ = the ion velocity and $\mathbf{B}$ = the magnetic field where present that is typically produced by current in a coil.

The mechanism is detailed in the following analysis assumes that (1), there is a plasma present when the current starts flowing in the thruster coil and (2), that there is no magnetic field trapped in the plasma. Given these assumptions, the plasma is driven away from the coil by an increase in magnetic pressure that arises from the $\mathbf{j} \times \mathbf{B}$ Lorentz force acting between an induced plasma current I_p and the axial magnetic field $\mathbf{B_z}$. The interaction produces a magnetic pressure that compresses the plasma and a magnetic tension that together drive the plasma from the coil. Using Ampere's Law in differential form to obtain the force density exerted by the field $\mathbf{B_z}$ on the plasma current I_p we have:

$$\mathbf{F} = \mathbf{j} \times \mathbf{B} = (\nabla \times \mathbf{B}) \times \frac{\mathbf{B}}{\mu_0} \qquad \text{Eq. 31}$$

Using the vector identity:

$$\frac{1}{2}\nabla(\mathbf{B} \cdot \mathbf{B}) = \mathbf{B} \times (\nabla \times \mathbf{B}) + (\mathbf{B} \cdot \nabla)\mathbf{B} \qquad \text{Eq. 32}$$

Gives:

$$\mathbf{F} = \mathbf{j} \times \mathbf{B} = \frac{1}{\mu_0}(\mathbf{B} \cdot \nabla)\mathbf{B} - \nabla(\frac{B^2}{2\mu_0}) \qquad \text{Eq. 33}$$

The first term on the right represents a magnetic tension force[1] of magnitude $\frac{B^2}{\mu_0}$ that is parallel to $\mathbf{B}$ and the second term represents a magnetic pressure of magnitude $\frac{B^2}{2\mu_0}$ that is perpendicular to $\mathbf{B}$ and parallel to the field gradient. The process may be seen in the following example – a linear theta pinch thruster that produces high velocity plasma jets by driving a large current of short duration through a single turn coil. If of sufficient intensity, the rapidly changing axial field $\mathbf{B_z}$ produced by the current

[1] Magnetic tension force acts to straighten curved magnetic field lines.

pulse induces an electric field in the theta or azimuthal direction that ionizes a gas. Otherwise, a separate source of ionized gas provides the plasma propellant.

The plasma is heated and compressed by the Lorentz force produced by the increasing magnetic field and is expelled from the ends of the coil as jets (fig. 9) [LaPointe 2000 [57]].

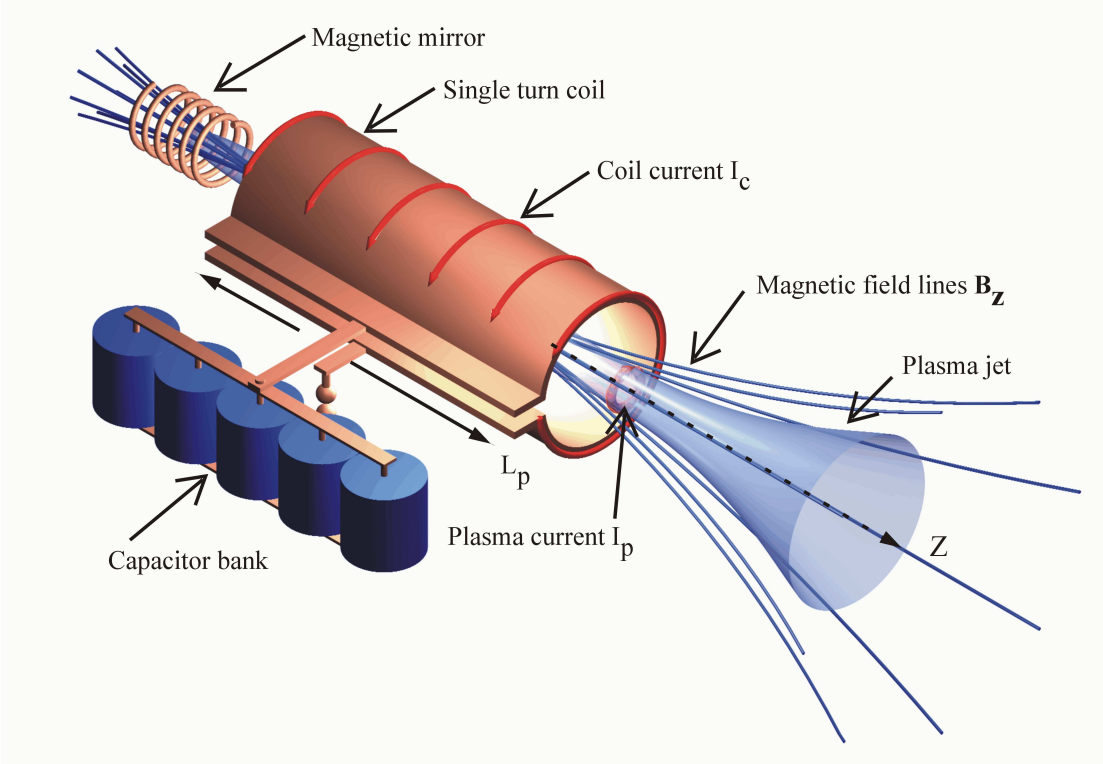

Figure 9 Linear theta pinch thruster basic configuration showing a plasma jet that is heated and compressed by the magnetic field $\mathbf{B_z}$ produced by a large transient current I_c that passes through a single turn coil of length L_p from the capacitor bank. A magnetic mirror may be employed to reverse the direction of the plasma jet emerging from the spacecraft end of the thruster.

3.2.2 Magnetic nozzles

Magnetic nozzles are formed whenever a solenoidal field is used to confine plasma and can be used to direct and accelerate plasma by interactions between the plasma and the magnetic field (fig. 10). Although there are functional similarities between the operation of a conventional convergent-divergent de-Laval nozzle in a chemical rocket and a magnetic nozzle, the processes in an electric thruster can supply more energy to the propellant than is possible in a chemical rocket. In general, magnetic nozzles may be regarded as electrothermal devices where the plasma may be produced by a number of different mechanisms and magnetic and thermal forces together with ambipolar acceleration that balances an electron pressure gradient drive the plasma from the nozzle [Arefiev and Breizman 2008 [58]].

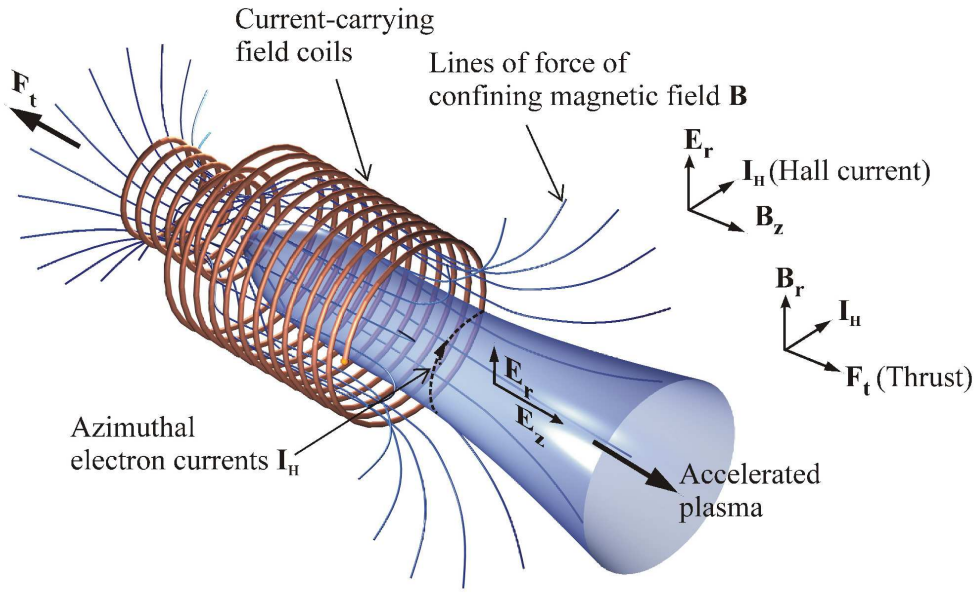

Figure 10 A magnetic nozzle showing the magnetic field strength along the axis of the nozzle. E_r and E_z are the components of the electric field that is the result of the electron pressure gradient produced by the diverging magnetic field. Currents in the field coils generate the magnetic field **B** that interacts with the electric field to produce azimuthal electron Hall currents $\mathbf{I_H}$, (produced in the E_r x B_z direction when an electric field is applied to a conductor containing a magnetic field). Those currents then create magnetic forces that accelerate the plasma and produce thrust $\mathbf{F_t}$.

Early work [Andersen et al 1968 [59]] demonstrated that a magnetic nozzle could produce steady supersonic plasma flows with Mach numbers of the order of 3. Those experimental results showed a relation between the magnetic nozzle area A_n (z), and the measured Mach number $M(z)$, both expressed as a function of distance z along the nozzle in accordance with the fluid equation for isothermal ions and electrons:

$$\frac{M^2-1}{M}\frac{dM}{dz}=\frac{1}{A_n}\frac{dA_n}{dz} \qquad \text{Eq. 34}$$

Since that time, considerable effort has been expended in the development of a theoretical understanding of the processes that occur within a magnetic nozzle as well as in the construction of experimental and practical devices.

For instance, the following analysis shows that the loss of plasma through cross field drift in a magnetic nozzle can be reduced by increasing the field strength [Takahashi et al 2013 [60]]. Starting with the plasma momentum equation (eq. 35), the presence of a pressure gradient or an electric field in a plasma gives rise to cross field drifts [Inan and Golkowski 2010 [61]]:

$$m_s n_s\left[\frac{\partial \mathbf{u}}{\partial t}+(\mathbf{u}\cdot\nabla)\mathbf{u}\right]=-\nabla p_f+qn_s(\mathbf{E}+\mathbf{u}\times\mathbf{B}) \qquad \text{Eq. 35}$$

Where **u** is the mean fluid velocity, n_s is the number density of the species, m_s is the mass of the species, p_f is the plasma pressure and q is the charge.

The LHS of Eq. 35 can be set to zero since drift velocities are much smaller than the average particle velocity, ∇ points in the radial direction and the current created by the drift is azimuthal so that $\nabla \cdot \mathbf{u} = 0$. We then have:

$$0 = -\nabla p_f + qn_s(\mathbf{E} + \mathbf{u} \times \mathbf{B}) \quad \text{Eq. 36}$$

Taking the cross product of this equation with **B** and using the vector triple product identity gives:

$$0 = -\nabla p_f \times \mathbf{B} + qn_s(\mathbf{E} \times \mathbf{B} + \mathbf{B}(\mathbf{u} \cdot \mathbf{B}) - \mathbf{u}(\mathbf{B} \cdot \mathbf{B})) \quad \text{Eq. 37}$$

Which, since **u** and **B** are at right angles leads to:

$$\mathbf{u} = \frac{\mathbf{E} \times \mathbf{B}}{B^2} - \frac{\nabla p_f \times \mathbf{B}}{qn_s B^2} = \mathbf{u}_E - \mathbf{u}_D \quad \text{Eq. 38}$$

The first term $\mathbf{u}_E$ is the $\mathbf{E} \times \mathbf{B}$ drift while the second term $\mathbf{u}_D$ is the diamagnetic drift, which, since it depends upon the sign of the particle charge, in the case of electrons gives rise to a diamagnetic current that produces a field opposite to the applied field. Increasing the applied field strength therefore reduces the drift losses and the diamagnetic electron current. Experimental work supports this theoretical analysis and demonstrates that an increased magnetic field strength inhibits cross-field diffusion while maintaining a constant plasma density and electron temperature [Takahashi et al 2013 [60]].

A simple analytical model of the thrust developed in a plasma in an expanding magnetic field has been developed that assumes axi-symmetric plasma, negligible electron inertia, negligible radial ion inertia and cold ions [Takahashi et al 2013 [60]]. In this model the thrust produced by the axial momentum imparted to the plasma is given as:

$$T_{total} = T_s + T_w + T_B \quad \text{Eq. 39}$$

Where:

$$T_s = 2\pi \int_0^{r_s} r p_e(r, z_0) dr \quad \text{Eq. 40}$$

(T_s is the integral of the electron pressure p_e that acts on the back plate of the thruster via ion acceleration in the sheath that converts electron pressure into momentum of the ions.)

$$T_w = -2\pi \int_{z_{end}}^{0} r_s m_{ion} n_w u_r(r_s, z) u_z(r_s, z) dz \quad \text{Eq. 41}$$

(T_w is the integral of the axial momentum produced by ions lost to the thruster wall.)

$$T_B = -2\pi \int_0^z \int_0^{r_p(z)} r \frac{B_r(r,z)}{B_z(r,z)} \frac{\partial p_e(r,z)}{\partial r} dr dz \quad \text{Eq. 42}$$

(T_B is the integral of the Lorentz force produced by the cross product of the radial magnetic field component B_r and the azimuthal electron diamagnetic drift current $B_z^{-1} \partial p_e / \partial r$. **)**

Where r_s, r_p, z_0, n_w, u are the source tube radius, plasma radius, axial position of maximum electron pressure, ion density at the radial wall boundary and the ion velocity respectively.

Following this model, measurements made of the effect of a magnetic nozzle on plasma [Takahashi et al 2013 [60]] show that:

(1) In the absence of a magnetic field, the electron pressure in the back wall sheath produces all of the thrust. In the presence of an axial magnetic field, the thrust produced by the back wall sheath remains constant,

(2) The side wall makes no significant contribution to the thrust and in the absence of an axial magnetic field, the thrust contributed by the wall is negative,

(3) In the presence of an axial magnetic field, thrust is produced by the Lorentz force resulting from the interaction of the radial magnetic field component B_r and the azimuthal electron diamagnetic drift current $B_z^{-1}\,\partial p_e / \partial r$. It increases linearly with the field strength and adds to the thrust produced by the back wall sheath.

A recent review [Ebersohn et al 2012 [62]] covered the most significant aspects of the physics of magnetic nozzles and showed that there are three key processes required for the production of thrust:

1. Plasma must detach from the magnetic field of the nozzle to produce thrust and to prevent damage to the spacecraft by the return of charged particles along the nozzle field lines.
2. Momentum has to be imparted to the spacecraft by the forces on the expelled plasma. The process is mediated by the Lorentz force, the resultant of the sum of the magnetic pressure and the magnetic tension force:

$$\mathbf{F}_t = \mathbf{j} \times \mathbf{B} = -\nabla \frac{\mathbf{B}^2}{2\mu_0} + \frac{1}{\mu_0}(\mathbf{B} \bullet \nabla)\mathbf{B} \qquad \text{Eq. 43}$$

   Where the first term on the right corresponds to the isotropic magnetic pressure, the second term corresponds to the magnetic tension force, present only for curved field lines and $\mathbf{j}$ is the current density.
3. Energy must be transferred from the power supply to the kinetic energy of the propellant.

A later 2-D theoretical analysis of the supersonic expansion of a plasma in a diverging magnetic field [Martinez 2013 [63]] demonstrated that:

1. The ambipolar electric field converts the energy of the electrons into directed energy of the ions,
2. A diamagnetic electron Hall current is responsible for the radial confinement and axial acceleration of the plasma. Thrust is the result of the reaction of this current on the currents in the field windings,

3. Prevailing theories for plasma detachment resulting from resistivity, electron inertia and plasma induced magnetic fields are inadequate explanations and detachment relies upon ion inertia and gradual demagnetisation.

In addition, the analysis showed that the formation of a double layer did not result in an acceleration of plasma.

In another study, MHD simulations of magnetic nozzles show that the addition of the Hall term generates an azimuthal current. Results obtained from this simple resistive model do not agree well with experimental observations and a suggestion is made that other computational methods such as hybrid PIC methods should be considered for the future study of magnetic nozzle physics [Ebersohn et al 2013 [64]].

In summary, these investigations demonstrate that incorporating a magnetic nozzle into the design of a plasma thruster makes possible the use of a variety of different plasma sources that by themselves may not efficiently produce a directed high velocity jet.

3.2.3 A note on Hall thrusters, end Hall ion sources and magnetic nozzles.

Hall thrusters, industrial end-Hall ion sources and magnetic nozzles employ crossed electric and magnetic fields to generate directed ion beams. In Hall thrusters and end-Hall ion sources, the magnetic field is radial to the axis of the device. The effect of the crossed fields in Hall thrusters is to retard electrons from flowing towards the anode in order to increase the strength of the electric field that is aligned with the axis of the device and within the plasma. The electric field accelerates the plasma and Hall thrusters and end-Hall ion sources are regarded as grid-less electrostatic devices (Oudidi et al 2011 [65]).

In contrast, in a magnetic nozzle the magnetic field is aligned with the axis of the device and diverges at the exit. The effect of the divergent magnetic field on the electrons is to produce an electric field and the radial component of that electric field crossed with the axial magnetic field produces an azimuthal Hall current in the plasma that reacts against the coil current to produce thrust (fig. 11).

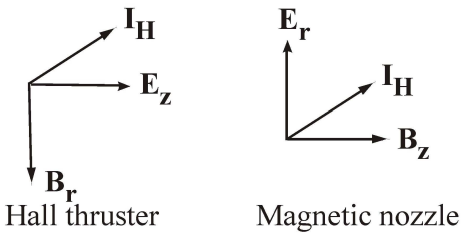

Figure 11 Hall currents ($\mathbf{I}_H$) arising from crossed electric and magnetic fields in Hall thrusters ($\mathbf{B}_r \times \mathbf{E}_z$) and in magnetic nozzles ($\mathbf{E}_r \times \mathbf{B}_z$).

3.2.4 Rotating magnetic field acceleration (RMF)

Rotating magnetic field (RMF) thrusters - also known as ELF or Electrodeless Lorentz Force thrusters - use rotating magnetic fields to heat and confine plasmas that are then expelled by Lorentz force. The use of rotating magnetic fields to drive currents in plasmas has been investigated since the 1950s and is a special case of the more general non-linear $\mathbf{j}\times\mathbf{B}$ Hall current drive [Jones 1999 [66]]. The rotating magnetic field is the resultant of the vector sum of two sinusoidally varying components that are 90° out of phase and supplied to antennas that are physically oriented at 90° to each other located outside the axial magnetic field coils. Penetration of the rotating magnetic field into the plasma drives azimuthal electron currents that reverse the direction of the solenoidal field and result in the formation of an electrically neutral field-reversed closed poloidal field plasmoid. The plasmoid can be accelerated to produce thrust and since it is electrically neutral, an RMF plasma thruster does not require a cathode to produce charge-neutralizing electrons.

The mechanism of plasma confinement and heating in these devices is shown in the following figure (fig. 12) and described in the following text.

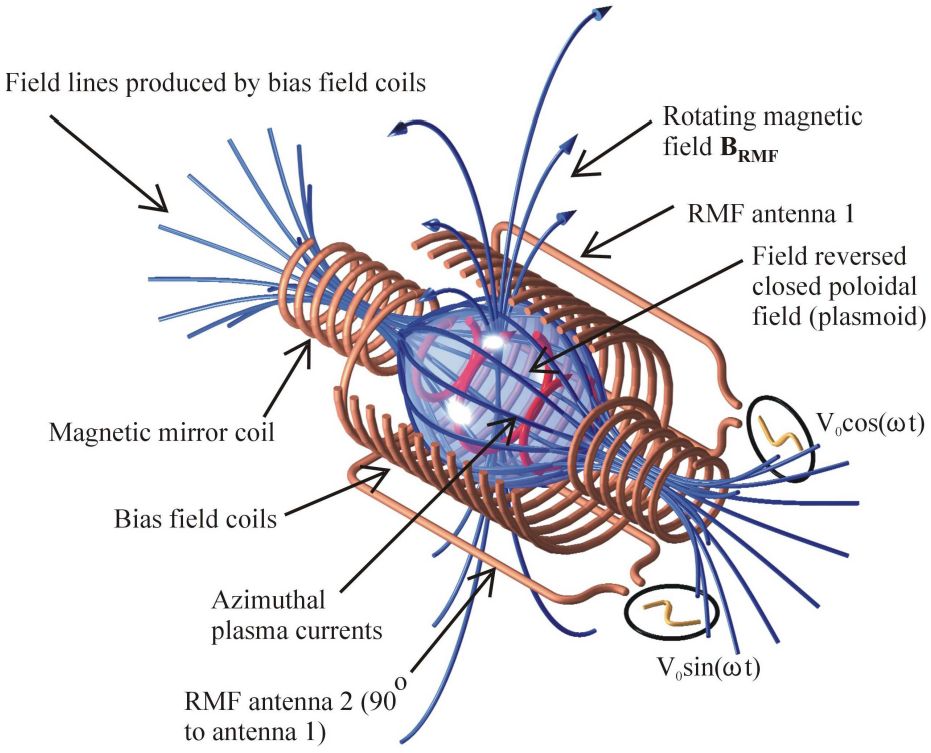

Figure 12 RMF components showing magnetic fields, current drive, azimuthal currents and field reversed closed poloidal field plasmoid that develops in rotating magnetic field driven plasmas. The figure shows the surrounding confining bias field coil, the two orthogonal antennae that produce a rotating field and the azimuthal plasma currents (red) induced in the plasma by the rotating magnetic field B_{RMF} resulting from AC currents in the RMF antennae.

3.2.4.1 RMF plasma current drive mechanism

In this analysis the ions form an immobile, uniformly distributed background of positive charge in which the electrons are regarded as an inertia-less, pressure-less negatively charged fluid.

Given this approximation, the current drive may be understood from the starting point of the generalized Ohm's law [Slough and Miller 2000 [67]]:

$$\mathbf{E} = \eta_p \mathbf{j} + \frac{1}{n_e e}(\mathbf{j} \times \mathbf{B}) = \eta_p \left[\mathbf{j} + \frac{\omega_{ce}}{\nu_{ei}} (\mathbf{j} \times \mathbf{e}_B) \right] \qquad \text{Eq. 44}$$

Where $\mathbf{E}$ is the electric field strength, η_p is the plasma resistivity, $\mathbf{j}$ is the current density, n_e is the electron number density, e is the electron charge, $\mathbf{B}$ is the magnetic field vector that has oscillating components B_r and B_θ at the RMF frequency ω_{RMF} and $\mathbf{e}_B$ is the magnetic field unit vector**.** In this equation $\omega_{ce} = \frac{eB}{m_e}$ is the electron cyclotron frequency and $\nu_{ei} = \eta_p \frac{n_e e^2}{m_e}$ is the electron-ion collision frequency where m_e is the electron mass. $\eta_p \mathbf{j}$ is the resistive term and $\frac{1}{n_e e}(\mathbf{j} \times \mathbf{B})$ is the Hall term.

If the term $\frac{1}{n_e e}\mathbf{j} \times \mathbf{B} << \eta_p \mathbf{j}$ then $E_\theta = \eta_p j_\theta = -\frac{d\Phi}{dt}$ is negative and flux leaves the plasmoid. Screening currents arise in the outer layers of the plasma that prevents the rotating magnetic field from penetrating the plasma (fig. 13).

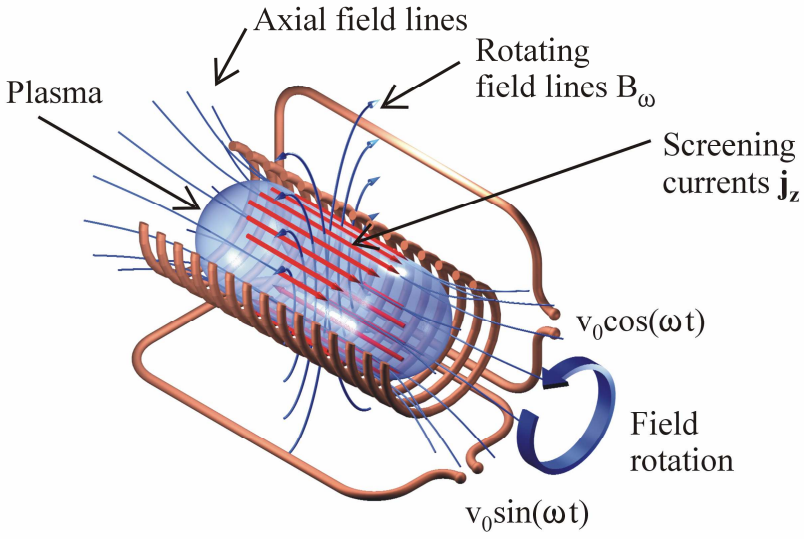

Figure 13 RMF plasma column with screening currents j_z arising from the induced electric field E_z produced by the application of a rotating magnetic field B_ω [after Jones 1999 [66]]. The effect of the screening currents is to prevent the penetration of the rotating magnetic field into the plasma that drives the electron currents.

If $\frac{1}{n_e e}\mathbf{j}\times\mathbf{B} >> \eta_p \mathbf{j}$ and $j_z B_r$ is large and negative (where the current j_z is driven by an induced axial electric field produced by the rotating field), then the Hall term has the opposite sign to $\eta_p \mathbf{j}$ and E_θ can be negative. Under those conditions, the flux enters the plasmoid and field reversal grows, the electrons are magnetized and the rotating field penetrates the plasma producing azimuthal electron currents that create a magnetized plasmoid that forms a reversed field configuration that can be expelled to create thrust (fig. 14) [after Jones 1999 [66]].

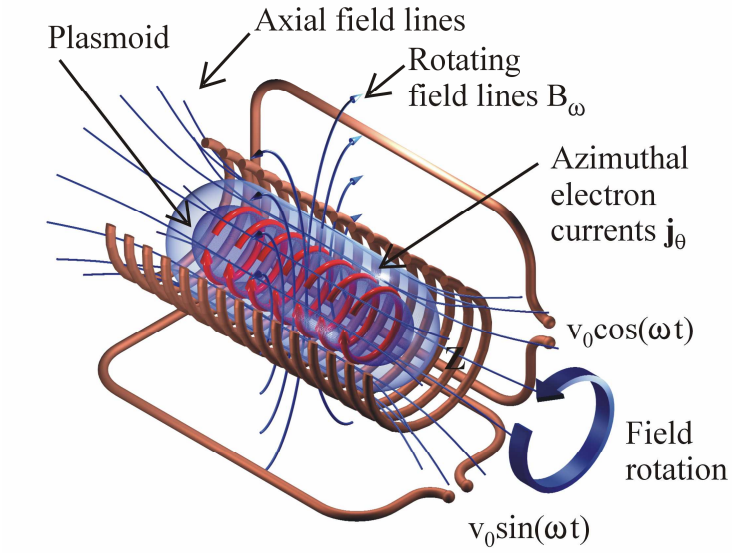

Figure 14 RMF plasma column with a field reversed plasmoid embedded in the plasma column. A plasmoid is created by the effect of the azimuthal electron currents produced by the rotating magnetic field. The plasmoid forms a separate magnetic domain within the plasma that by a suitable arrangement of magnetic fields can be expelled to produce thrust.

As can be seen from Eq. 44, $\nu_{ei} << \omega_{ce}$ is a requirement if the magnetic field is to penetrate into the plasma while the angular frequency ω_{RMF} of the applied field must be in the range $\omega_{ci} < \omega_{RMF} < \omega_{ce}$ to ensure that the ions do not co-rotate with the rotating field.

In addition, Eq. 44 shows that the electron density n_e and the electron-ion collision frequency ν_{ei} determine the extent to which the resistive term dominates the Hall term.

In the absence of plasma, the r and θ components of the rotating field $\mathbf{B}_\omega$ have the form:

$$B_r = B_\omega \cos(\omega t - \theta) \qquad \text{Eq. 45}$$

$$B_\theta = B_\omega \sin(\omega t - \theta) \qquad \text{Eq. 46}$$

Where B_ω is the amplitude of the rotating field and θ is the azimuthal cylindrical coordinate.

In the presence of plasma the axial components can be determined by introducing the magnetic vector potential **A** where:

$$\mathbf{B} = \nabla \times \mathbf{A} \qquad \text{Eq. 47}$$

And by taking the limit where $\eta_p \mathbf{j} \cong 0$ so that Ohm's law assumes the form:

$$\mathbf{E} = \frac{1}{n_e e}(\mathbf{j} \times \mathbf{B}) \qquad \text{Eq. 48}$$

It can then be shown that the following equations are exact solutions of Ohm's Law:

$$A_z = -B\omega r \sin(\omega t - \theta) \qquad \text{Eq. 49}$$

$$B_z = B_{axial} - \frac{1}{2} ne\omega\left(r_p^2 - r^2\right) \qquad \text{Eq. 50}$$

Where B_{axial} is the axial magnetic field strength and r_p is the plasma diameter.
The azimuthal current density, j_θ is given by:

$$j_\theta = -\frac{1}{\mu_0}\frac{\partial B_z}{\partial r} = -n_e e \omega_{RMF} r \qquad \text{Eq. 51}$$

This result indicates that the plasma electrons rotate synchronously with the rotating field where the electron drift velocity at any radial position *r* is given by $r\omega$.
Electromagnetic theory indicates that the RMF will not penetrate the plasma beyond the resistive skin depth δ_s, the distance below the surface of a conductor where the current falls to 0.37 of the surface current. Resistive skin depth is approximated by:

$$\delta_s = \sqrt{\frac{2\eta_p}{\mu_0 \mu_r \omega}} \qquad \text{Eq. 52}$$

However when an RMF is applied to a plasma, the electrons rotate with the RMF and in that frame of reference, the RMF appears stationary and the field can penetrate the plasma to the axis of symmetry. In order to penetrate the plasma, the RMF must exceed a threshold value and it has been shown [Hoffman et al 2006 [68]] that the RMF magnetic flux density must exceed a value $B_{\omega RMF}$ such that:

$$B_{\omega_{RMF}} > \sqrt{\frac{\mu_0}{2}} e n_e r \sqrt{\eta_p \omega_{RMF}} \qquad \text{Eq. 53}$$

If the condition is satisfied, the RMF penetrates the plasma and the penetration is maximized when the electrons rotate in synchrony with the rotating field.

3.2.4.2 Thrust produced by the RMF

Thrust produced by the effect of the RMF current drive is similar to that produced by a magnetic nozzle where, independent of the generating mechanism, the induced azimuthal electron current in the presence of the diverging magnetic field creates the axial component of the thrust.

If the radial magnetic field B_r is expressed as $B_r \cong B_z\left(r/2R_{coil}\right)$ and assuming that the electron density is spatially uniform then the thrust can be estimated as:

$$F_t = L_A \int_0^{r_p} j_\theta B_r (2\pi r) dr = \frac{\pi r_p}{4R_{coil}} e n_e L_A \omega_{RMF} B_z r_p^3 \qquad \text{Eq. 54}$$

Where R_{coil} is the axial coil radius, L_A is the length of the accelerating region and r_p is the plasma radius.

For typical values of $\omega_{RMF} = 6 \times 10^6$ s^{-1}, $R_{coil} \cong r_p = L_A = 5cm$, $n_e = 10^{12}$ cm^{-3}, and $B_z = 500$ G, Eq. 54 yields F_t =100 mN [Shinohara et al 2014 [69]].

3.2.5 Rotating electric field acceleration (REF)

The use of rotating electric fields (REF) as a means of accelerating plasma was first reported in 2003 [Toki et al 2003 [70]]. In this device, a plasma produced by a helicon discharge is electromagnetically accelerated using a rotating electric field in the presence of a diverging static magnetic field [Nakamura et al 2012 [71]]. The Lissajous thruster consists of a helicon plasma source with two pairs of parallel plates at the outlet energised by sinusoidal voltages with a phase difference of 90 degrees in the same manner as the RMF thruster. The resulting rotating electric field induces an azimuthal current in the plasma and the reaction of this current with the radial component of the diverging solenoidal field accelerates the plasma (fig. 15).

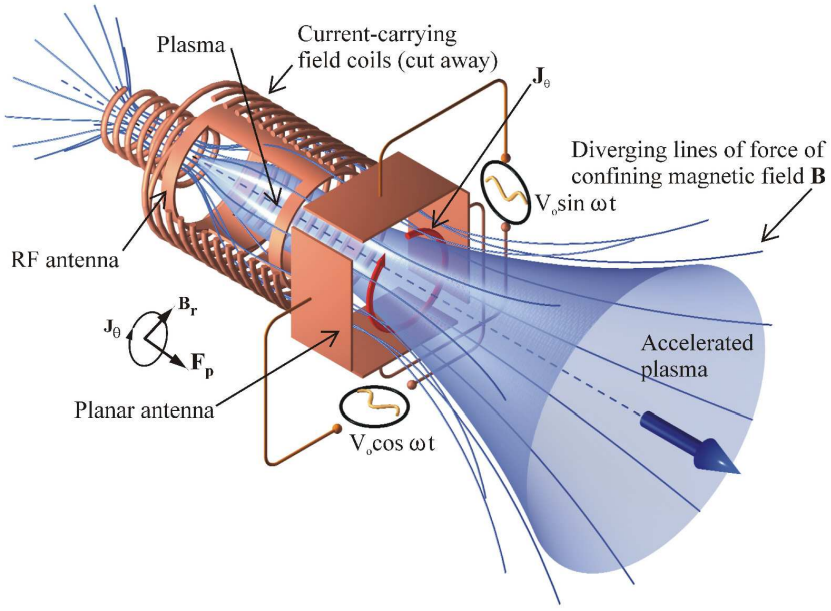

Figure 15 In the Lissajous thruster the rotating electric field created by planar antennae drives an azimuthal current $\mathbf{J}_\theta$ that interacts with the radial component of the solenoidal field $\mathbf{B}$ to produce a Lorentz force $\mathbf{F}_t = \mathbf{J}_\theta \times \mathbf{B}_r$ that provides a component of the thrust. Thrust is also produced by the effects of the magnetic nozzle that is formed by the diverging magnetic field.

3.2.5.1 Thrust produced by the REF

Assuming that $R_L << R_G << r_0$, where $R_L = \frac{v_\perp}{\omega_{ce}}$ is the Larmor radius, $R_G = \frac{E_0}{B_z \omega}$ is the gyration radius of electrons moving at the azimuthal cross-field drift velocity under the influence of the REF and $v_{ions} << v_{electrons}$, the theoretical thrust F_t can be obtained by integrating $j_\theta(r) \times B_r(r)$ with $B_r(r) = B_z r / 2r_m$ to give:

$$F_t = \frac{\pi}{4} e\beta n_0 L \frac{r_t^2}{r_m}\left(\frac{E_{p0}^2}{\omega_{REF} B_z} + \frac{v_\perp m_e}{r_t}\right) \quad \text{Eq. 55}$$

Where e is the electron charge, β is the rate of decline of plasma density, n_0 is the initial electron number density, L_A is the axial length of the acceleration section, r_0 is the radius of the thruster, r_m is the radius of the magnetic coil and ω_{REF} is the rotating electric field frequency. B_z is the axial magnetic field strength, $v_\perp$ is the plasma perpendicular velocity, m_e is the electron mass and E_{p0} is the amplitude of the REF penetration into a uniform magnetized plasma that is given by:

$$E_{p0} = \left(1 - \frac{1}{\mu_0}\left[\varepsilon_a - \sqrt{\varepsilon_a^2 + \mu}\right]^2\right)\frac{V_0}{2r_0} \quad \text{Eq. 56}$$

Where $\varepsilon = 1 - \frac{\omega_{REF}^2}{\omega_{ce}^2} \approx 1$ and $\mu = \frac{2eV_0\omega_{pe0}^2}{m_e r_0^2 \omega_{ce}^4}$.

3.2.6 Ponderomotive force thrusters.

Ponderomotive force thrusters exploit the non-linear ponderomotive force $\mathbf{F}_{pf}$ that acts on a charged particle that is proportional to the negative gradient of the intensity of an inhomogeneous oscillating electromagnetic field in the presence of a magnetic field (fig. 16). The particle oscillates at the field frequency ω_f and drifts towards the weaker field in a direction that is independent of the polarity of the particle's charge.

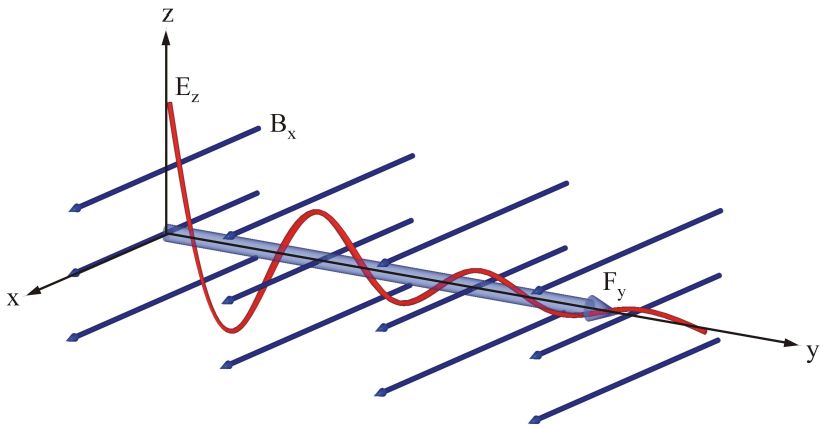

Figure 16 In a ponderomotive force thruster, the force F_y on a charged particle is produced by an inhomogeneous oscillating electromagnetic field of frequency ω_f with an electric field component E_z in the presence of a magnetic field B_x.

3.2.6.1 Thrust produced by the ponderomotive force

In a spatially varying oscillating electric field:

$$\mathbf{E} = \mathbf{E}_0(\mathbf{r}) \cos \omega_f t \qquad \text{Eq. 57}$$

Where the electric field amplitude $\mathbf{E}_0(\mathbf{r})$ is approximated by:

$$\mathbf{E}_0(\mathbf{r}) = \mathbf{E}_0(\bar{\mathbf{r}}) + \Delta\mathbf{r}(t) \bullet \nabla \mathbf{E}_0(\bar{\mathbf{r}}) \qquad \text{Eq. 58}$$

And where $\bar{\mathbf{r}}$ is the time average over the oscillation period $2\pi/\omega_f$ and $\Delta\mathbf{r}(t)$ is the oscillating component then the ponderomotive force arises along the gradient of $\mathbf{E}_0(\mathbf{r})$ and is given by:

$$\mathbf{F}_{pf} = -\frac{q^2}{4m_e\omega_f^2} \nabla |\mathbf{E}_0(\bar{\mathbf{r}})|^2 \qquad \text{Eq. 59}$$

In a non-magnetized plasma, the force is directly proportional to the gradient in Eq 59 however the force is modified when the oscillating electric field $\mathbf{E}(t)$ has a component perpendicular to an applied magnetic field **B**. The direction of the force is determined by the relative strengths of the electric and magnetic fields (fig. 16).

In a magnetized plasma the ponderomotive force on an electron is given by:

$$\mathbf{F}_{magnetized} = -\frac{q^2}{4m_e} \frac{1}{\left(\omega_f^2 - \omega_{ce}^2\right)} \frac{\partial E_{0z}^2}{\partial \bar{z}} \qquad \text{Eq. 60}$$

Where $\omega_{ce} = \dfrac{qB}{m_e}$ is the electron cyclotron resonant frequency.

In the presence of a magnetic field the direction of the ponderomotive force depends upon the sign of the denominator in Eq. 60, that is whether $\omega_f^2 > \omega_{ce}^2$ or $\omega_f^2 < \omega_{ce}^2$. This means that the strength of

the applied magnetic field and the frequency of the electromagnetic field can be used to control the direction of acceleration. Eq. 60 shows that the strength of the ponderomotive force is resonantly enhanced when ω_f approaches ω_{ce}. (fig. 17).

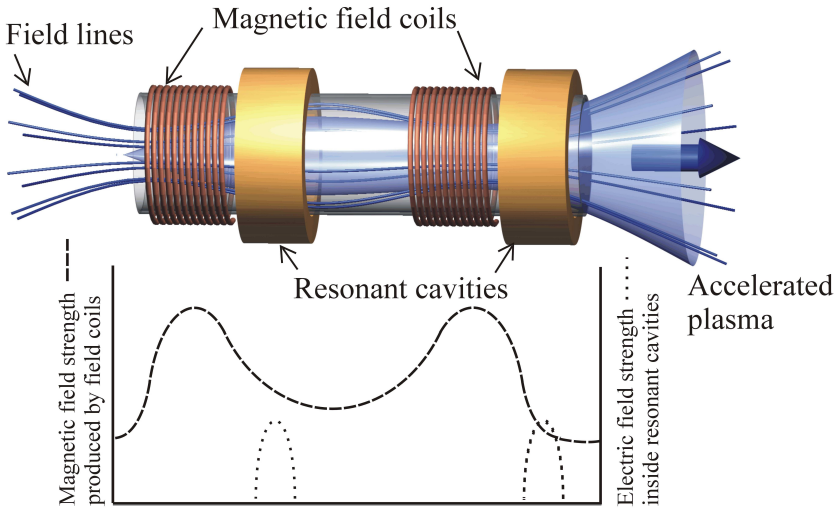

Figure 17 In the microwave driven ponderomotive force thruster the magnetic field windings create a magnetic bottle and a diverging magnetic field. The resonant cavities fed with microwave energy create a localized electromagnetic field with steep gradients that provides the conditions that produce the ponderomotive force acceleration [after Emsellem and Larigaldie 2007 [72]].

Ion cyclotron resonance heating of the plasma increases the energy of ions moving perpendicular to the axial magnetic field that are then accelerated by the nozzle that arises in the diverging magnetic field [Otsuka et al 2013 [73]].

3.2.7 Ponderomotive force thrusters using lasers.

The application of intense laser pulses to plasma to produce accelerated particles were first suggested in 1979 by Hooker [Hooker 2013 [74]]. Hooker's work showed that as an intense laser pulse propagates through a plasma, a trailing Langmuir wave with a group velocity equal to that of the pulse forms with a longitudinal electric field strength in the range of 1×10^9 to 1×10^{12} V/m. That electric field then accelerates charged particles in the plasma (fig. 18).

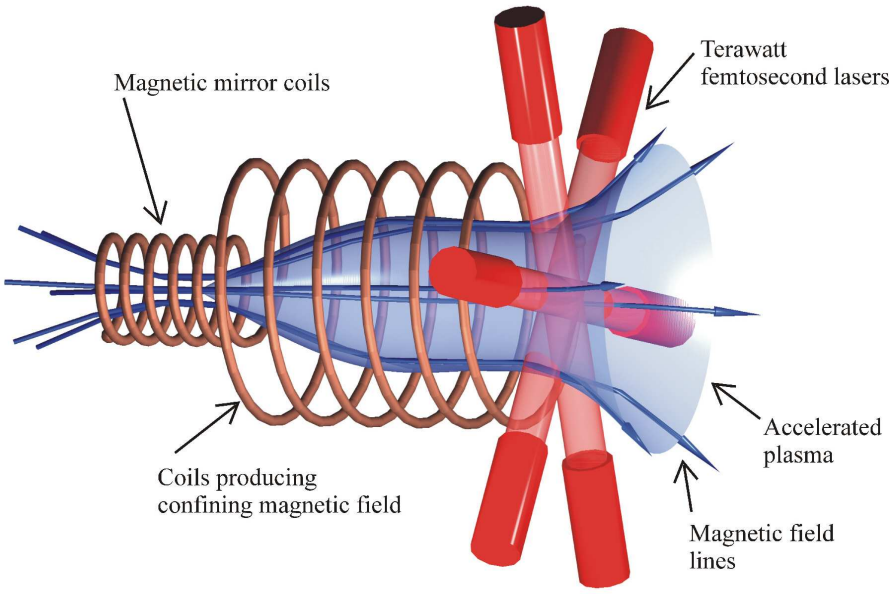

Figure 18 Laser driven ponderomotive force thruster employing femtosecond terawatt pulsed lasers to accelerate plasma confined by an axial magnetic field. A magnetic mirror is used to trap particles that are driven towards the rear of the thruster by the intense electric field produced by the laser pulse. Thrust is produced by the interaction of charged particles with the radial component of the magnetic field.

That work demonstrated that an intense electromagnetic pulse can create a wake of plasma oscillations through the action of the nonlinear ponderomotive force and later studies have shown that a specific impulse of $I_{sp} > 10^5$ s may be achieved with such a device employed as a thruster.

The maximum amplitude of the accelerating wave field is given by [Williams and Gilland 2009 [75]]:

$$E_{max} = 2.8 \times 10^4 \left(\frac{\lambda_L}{r_L} \right)^2 \frac{P_L}{\lambda_P} \quad 10^9 \text{V/m} \qquad \text{Eq. 61}$$

Where λ_L is the laser wavelength, r_L is the radius of the laser beam spot size, P_L is the laser power (1012 W) and λ_P is the plasma wavelength.

3.2.8 Helicon double layer acceleration

Evidence that charged particles are accelerated in plasmas that contain an electric double layer (DL) is well established and it is widely accepted that electric double layers, in which an electric field arises between two oppositely charged space charge layers, can form in plasmas. Double layers can form as a result of anisotropies in the pitch angle of ions and electrons in a plasma in a diverging magnetic field [Alfven and Falthammar 1963 [76]]. Double layers may also be produced by the effect of temperature on the velocities of ions and electrons in an expanding plasma [Block 1977 [77]]. Separation is maintained by a balance between electrostatic and inertial forces and the potential difference between the layers is

given by $|\Phi_{DL}| \geq {k_B T_e}/{e}$ where k_B is Boltzmann's constant, T_e is the electron temperature and e is the electron charge. A DL is said to be strong if $e\Phi_{DL} >> kT_e$.

The acceleration of electrons and ions in such plasmas has been observed in laboratories and in astrophysical objects and more recently experimenters have measured the acceleration of ions in a plasma containing a current-free DL in a helicon discharge [Charles and Boswell 2003 [78]] (fig. 19).

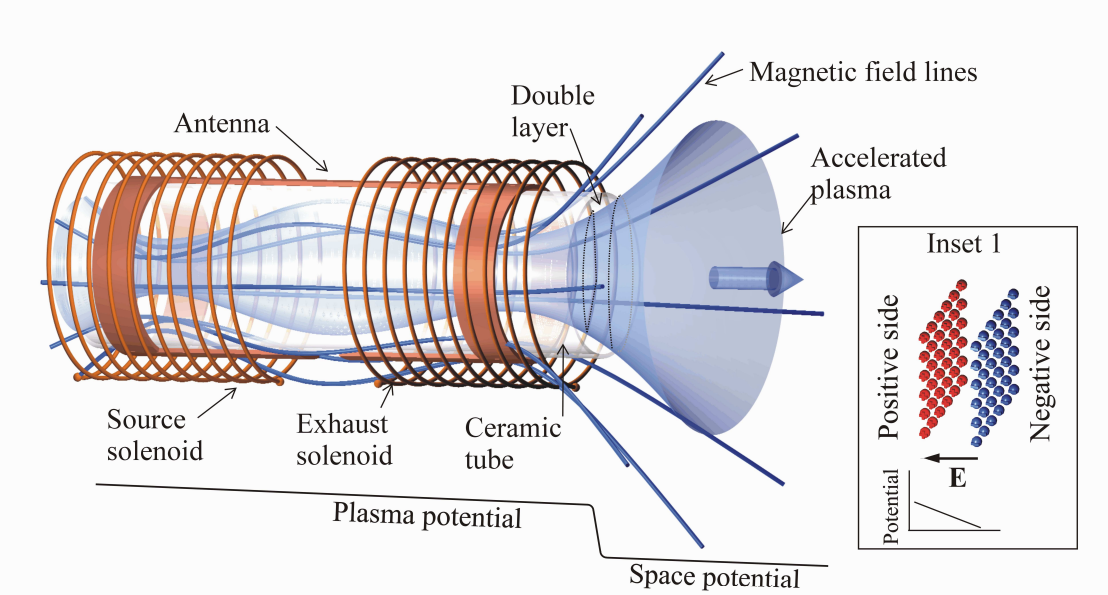

Figure 19 An inductive helicon thruster showing the profile of the axial plasma potential in an expanding plasma containing an electric double layer. Inset 1 shows the structure of the DL that arises from anisotropies of the pitch angles of ions and electrons in the diverging magnetic field in the expanding plasma.

Recent work with an inductive collisionless high-power (900W) helicon plasma in argon has demonstrated the production of an ion beam that appears to have been accelerated across a double layer like structure that has a time averaged plasma potential difference of 80V. The ion energy distribution of the beam had a bi-modal Maxwellian form with 77% of the accelerated ions having an energy greater than 65eV while the energy of the remaining ions peaked at 15eV, near the plasma potential [Sung et al 2016 [79]]. Despite that finding, the role of the double layer in the net acceleration of the ions remains uncertain. For instance, the following one-dimensional analysis shows that the net momentum delivered to the plasma by the electric field as it crosses the entire DL region is zero - assuming that the boundaries of DLs in real plasmas have no net charge [Fruchtman 2006 [80]]:

Multiplying the differential form of Gauss's law by the electric field gives:

$$\varepsilon_0 \nabla \bullet \mathbf{EE} = \rho_n \mathbf{E} \qquad \text{Eq. 62}$$

Where $\mathbf{E}$ is the electric field, ρ_n is the net charge density and ε_0 is the permittivity of free space.

In one dimension the integral form of this equation becomes:

$$\frac{\varepsilon_0}{2}\left[E(z_2)^2 - E(z_1)^2\right] = \int_{z_1}^{z_2} \rho_n E dz \qquad \text{Eq. 63}$$

This equation shows that since the electric field at the DL boundaries (z_1 and z_2) are zero, the electric force on the charge density ρ_n is also zero. In a DL, the force exerted on the ions driven in one direction is balanced by the force exerted on the electrons in the opposite direction and although in a DL in a divergent magnetic field the magnetic pressure can produce a net force since the DL is very narrow, that force is negligible [Fruchtmann and Makrinch 2009 [81]]. One and two-dimensional studies have shown instead that the acceleration of plasma results from magnetic field pressure arising in a diverging magnetic field that occurs in a magnetic nozzle rather than electrostatic forces in a DL [Fruchtman 2006 [80], Takahashi et al 2011 [82]]. Others have suggested that the acceleration of the bulk plasma may be caused by a directed coupling of the plasma electrons with the helicon wave field and the acceleration of the ions by the resulting ambipolar electric field [Ziemba et al 2005 [83]] or by a pre-sheath acceleration of ions [Chen 2006 [84]]. A more recent analysis of the processes occurring in current-free DLs concluded that while the DLs are produced by the thermodynamic effects of high energy electrons, they make no contribution to the thrust [Ahedo and Sanchez 2008 [85]].

Even though a DL may be present in a magnetized plasma, it may not be the only or even the main source of acceleration of ions. Further investigation is required to resolve the acceleration mechanism in these thrusters.

3.2.9 Acceleration by beating electrostatic waves (BEW).

Observations of the acceleration of ions in the topside ionosphere at an altitude of 1000km were made in the late 1970s although the mechanism was unclear. A 1998 study subsequently demonstrated that ions could be accelerated by a spectrum of electrostatic waves that propagate orthogonally to a magnetic field provided that there are waves with frequencies separated by an integer multiple of the cyclotron frequency [Benisti et al 1998 [86]].

Laboratory experiments [Vail and Choueiri 2014 [87]] supported that work by showing that a magnetized plasma can be efficiently heated by the interaction of two electrostatic waves in the plasma where the beat frequency between the waves with angular frequencies ω_1 and ω_2 is equal to the ion cyclotron frequency, Ω_{ni}:

$$\omega_2 - \omega_1 = \Omega_{ni} \qquad \text{Eq. 64}$$

Plasma heating by single electrostatic waves (SEW) relies upon a resonant transfer of energy with ions that have a velocity near to the phase velocity of the wave while beating electrostatic waves (BEW) have been shown to heat plasma by the exchange of energy with non-resonant ions that have thermal velocities lower than the phase velocity of the waves. Ions accelerate stochastically until they reach a velocity that is near to the phase velocity of the wave at which point resonant coupling between the wave and ions imparts greater acceleration. It has been shown that BEW heating is more effective than SEW heating only if the total wave energy density exceeds a threshold value [Jorns and Choueiri 2012

[88]]. Analysis shows that there are distinct regimes of electrostatic wave energy density in which either BEW or SEW will provide superior heating however, since BEW heating accelerates low energy ions, it is an efficient alternative to SEW heating and coupled to a magnetic nozzle, can form a component of an effective electrodeless plasma thruster. Experiments in the Electric Propulsion and Plasma Dynamics Lab at Princeton University have shown that the efficiency of SEW ion heating is ~50% while the efficiency of BEW heating is ~90% [Jorns and Choueiri 2009 [89]]. Enhanced heating of ions was observed even though the maximum energy density in that experiment was only 17% of the threshold at which BEW is expected to provide more efficient heating than SEW.

3.3 Magnetic mirrors

The simple plasma thruster (fig. 7) may be improved by using a magnetic mirror to prevent ions escaping through the sheath to the back wall (fig. 20). A magnetic mirror consists of a strongly converging magnetic field as viewed by a particle entering the mirror region. So long as the field gradient $\frac{\partial B_z}{\partial z}$ is almost constant compared to the gyro-radius scale, the magnetic moment of the particle, $\mu_m = \frac{1}{2} m_{ion} v_\perp / B$, is conserved and as the particle's perpendicular velocity $v_\perp$ increases as it moves into a region of stronger magnetic field. As a result, conservation of energy requires that the velocity parallel to the magnetic field $v_{||}$ decreases until it is reflected.

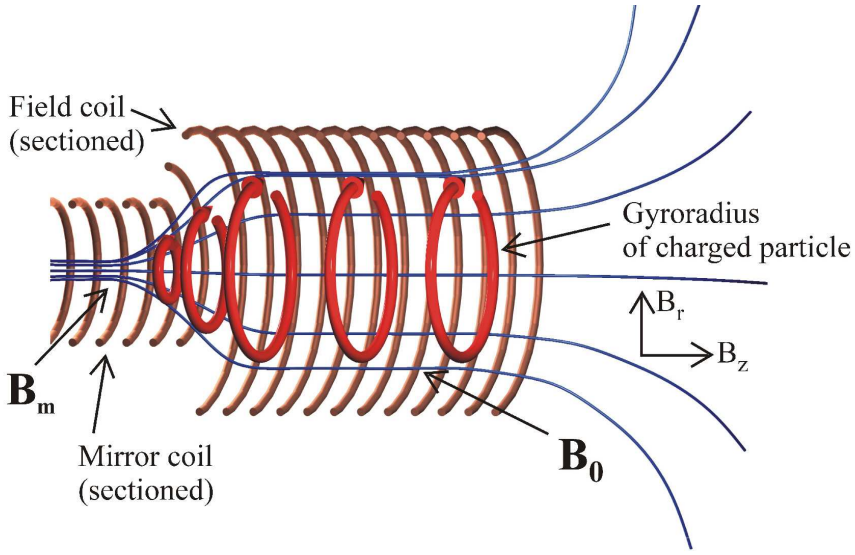

Figure 20 Drift of a particle in a magnetic mirror field B_m where B_0 = the solenoid flux density. The component B_r gives rise to a force that can trap a particle in a magnetic field through the conservation of the magnetic moment μ_m of the particle.

4 Electrodeless plasma thruster technology development

A description of the current state of electrodeless plasma thrusters and an analysis of the state of development of the most commonly reported devices.

The development of electrically powered thrusters did not receive serious intention until chemical rockets were able to launch suitable platforms into orbit in the 1960s. Since that time, a plethora of electric propulsion systems have been developed with many either under test or deployed.

The performance of a number of well-documented electrodeless plasma thrusters can be compared on the basis of the following figures of merit that determine the capacity of each type of thruster to enable a specified mission. Those figures of merit are: specific impulse I_{sp} (s), thrust efficiency η_t, thrust F_t (N) and lifetime (h), where published. Note that while figures for the first three figures of merit are commonly available, figures for lifetime of experimental electrodeless thrusters are not although the developers of electrodeless commonly claim that the absence of electrodes endows their devices with an extended durability despite the absence of confirming measurements.

The factors that limit the achievement of high exhaust velocities v_e and resulting high specific impulse I_{sp} in chemical propulsion systems are primarily the enthalpy of the hot propellant and secondly the maximum temperature that the materials of the rocket combustion chamber and nozzle can withstand. Electric propulsion systems overcome the enthalpy constraint by imparting more energy into a unit mass of the propellant, and in electrodeless thrusters and magnetically shielded Hall thrusters, the material temperature constraint is overcome by the use of magnetic fields that isolate the thruster structure from the hot propellant. Much higher specific impulses and consequently greatly reduced fuel consumption may be achieved compared to a chemical rocket. To date, all deployed plasma thrusters have used electrodes yet since those thrusters have been devices with power supplies that deliver at most a few kilowatts. For example, in the NSTAR thruster in the Deep Space 1 mission (input power 2100W [Rayman et al 2000 [12]]), erosion of the electrodes has not caused significant problems and nor has the space charge limited thrust density of approximately 440 N/m^2 for gridded ion thrusters been an impediment [Jahn 1968 [90]].

As missions require more powerful thrusters, electrode erosion will become an important consideration, one that can be answered by magnetic shielding or by electrodeless designs. Electrodeless designs do not have thrust density limits, are less sensitive to propellant purity and commonly do not require a charge neutralizer. To date (2017), no electrodeless plasma thrusters have been used in operational spacecraft although the design and construction of prototypes of various devices has been an active area of investigation for decades. The following discussion examines the electrodeless plasma thrusters that have been realised or have been shown by the number of publications to be devices of considerable interest.

In particular, the VASIMR (Variable Specific Impulse Magnetic Rocket), an electrodeless device that uses a helicon plasma source, ion cyclotron resonance heating and a magnetic nozzle, has been extensively discussed elsewhere [Squire et al 2016 [91]] and is therefore not mentioned here. Ongoing testing that will include integration of the components and high power firing is expected to bring the VX-200SS prototype to NASA's Technology Readiness Level 5 (TRL-5) in preparation for 100 hours of hot steady state continuous operation at 100 kW by February 2018.

4.1 Rotating magnetic field thrusters

4.1.1 The Electrodeless Lorentz Force (ELF) thruster

The ELF thruster (fig. 21) uses a rotating magnetic field to produce a plasmoid using the RMF drive mechanism where the plasmoid is driven from the thruster by $j_\theta \times B_r$ forces produced either by a conical magnetic field gradient or by sequencing currents in an array of flux coils [Slough, Kirtley and Weber 2009 [92]]. Since the magnetic field of the plasmoid is closed, detachment of the plasmoid from the thruster magnetic field is complete and as the plasmoid is uncharged, charge neutralization of the departing plasmoid is not required.

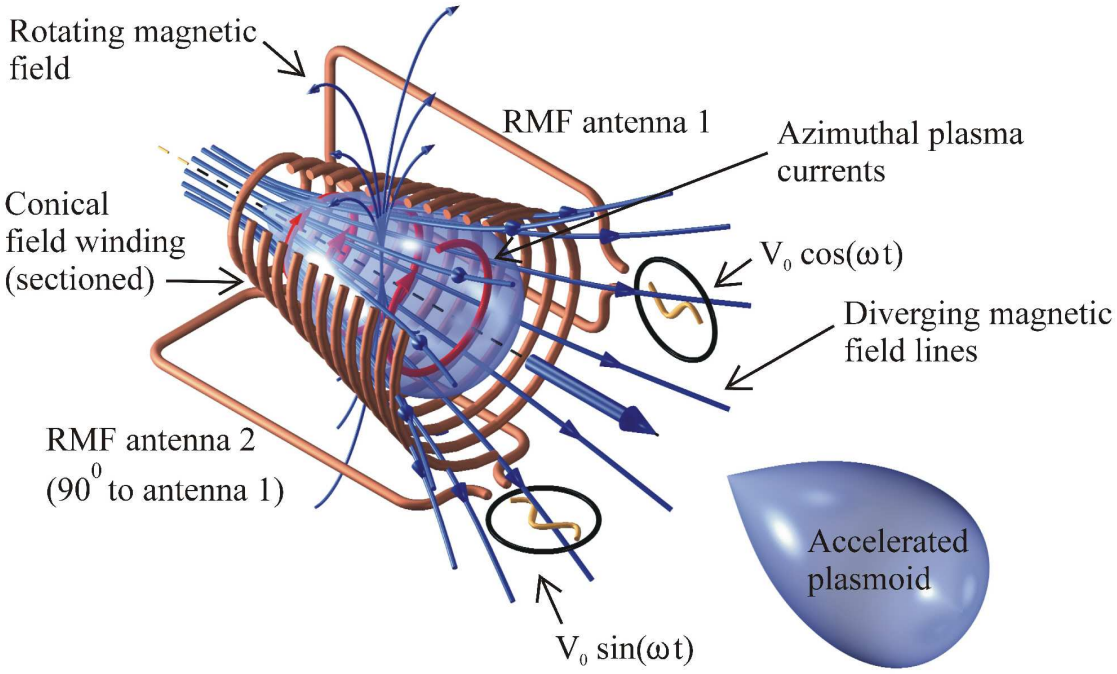

Figure 21 ELF rotating magnetic field thrusters expel a field reversed plasmoid that is accelerated by the Lorentz force produced by a conical solenoid surrounding the plasma. The diverging magnetic field acts as a magnetic nozzle that further accelerates the plasmoid and converts a proportion of the thermal energy of the plasma into directed kinetic energy that propels the spacecraft [Slough, Kirtley and Weber 2009 [92]]. The performance of this device is shown in table 3.

4.1.1.1 Lorentz force on the plasmoid in the ELF thruster

The plasmoid in the ELF thruster is subject to a constant acceleration by the magnetic field produced by the conical solenoid that surrounds the plasma.

In contrast, the force on the plasma in a pulsed inductive thruster that uses the Lorentz force between a current induced in the plasma and the magnetic field produced by a current in a planar coil decreases as the inverse of the square of the distance between the plasma and the planar coil. (Fig. 22). While the figure appears to show that the ELF thruster is more effective in accelerating a plasma than a pulsed inductive thruster, the creation of the radial magnetic field in the ELF thruster that heats and compresses the plasma absorbs energy that may however be recovered in expansion through the magnetic nozzle.

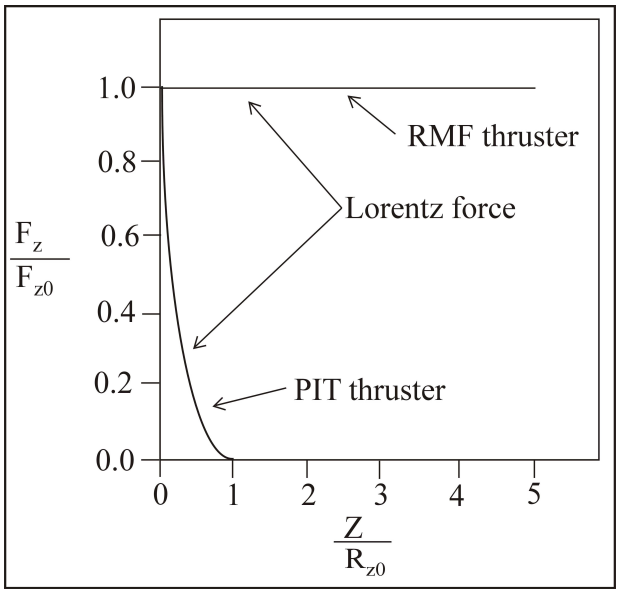

Figure 22 The normalized Lorentz body force on the plasmoid in an ELF thruster and on the plasma sheet in a pulsed inductive thruster (PIT) as a function of the axial distance in units of initial radius Z/R_{z0} (after Fig. 8 Slough, Kirtley and Weber 2009 [32]). The force on the plasmoid or plasma sheet is normalized to the initial maximum F_0 at a small initial separation.

Studies of various propellants show that RMF acceleration contributes 80% of the directed kinetic energy of the thruster while thermal expansion accounts for 16%. The thrust efficiency, η_t, for a 30kW thruster when operating on water or 95% carbon dioxide mixed with 2% nitrogen and 3% argon is calculated from measurements and approximations and reported to be 85+% [Kirtley et al 2012 [93]]. A later study of a sample return mission from the minor planet Ceres with a similar device (ELF-160A) gives a thrust efficiency of 60% when operating on xenon for the outbound voyage to Ceres and a thrust efficiency of 55% when using water obtained from Ceres for the inbound voyage to Earth [Pancotti et al 2015 [94]].

4.1.1.2 Erosion of walls in the ELF thruster

In experiments where the ELF thruster was fired for 3000 discharges no erosion of the thruster walls were detected [Kirtley et al 2011 [95]]. While these measurements suggest that erosion of components in ELF thrusters is not likely to be a life-limiting factor in the operation of these devices, much longer duration testing is required to verify that claim.

4.1.1.3 Further developments

Other work on ELF thrusters has been aimed at optimising the geometry and materials of the RMF antennae and improving the plasma loading whilst reducing unwanted resistive coupling [Waldock et al 2013 [96]].

4.1.1.4 Martian atmosphere and water used as ELF thruster propellants

Carbon dioxide (the principal component of the Martian atmosphere) and water vapour have been shown to be practical propellants for ELF thrusters [Kirtley et al 2012 [93]]. The operation of the ELF thruster with both carbon dioxide and water vapour produced plasmoids with velocities in excess of 15km/s.

Compared to operation with Xenon, the thruster required a greater input energy and formed weaker, lower pressure, and slower-moving plasmoids. However, the report states that the thrust efficiency η_t was not reduced although the coupling of energy into the plasmoid declined from 85% with Xenon to 20-50% with carbon dioxide and water vapour. A specific impulse in the range of 400 to 4000 s was obtained with carbon dioxide and injection, pre-ionization, and plasmoid formation was demonstrated with a steady flow of gas without coking, formation of deposits, erosion, or clogging.

4.1.1.5 Current status of ELF thrusters

Although the original intent of the development of ELF thrusters was to produce a working fusion rocket and reactor [Miller, Slough and Hoffman 1998 [97]], that goal has receded. Instead, a practical thruster that uses a rotating magnetic field driven from an external power supply to heat and accelerate a plasmoid has been produced [Slough, Kirtley and Weber 2009 [92]]. The following table (Table 3) shows reported values for the figures of merit.

Parameter	**Measured value**
Specific Impulse I_{sp} (s)	1000 – 6000 (N_2, Air and Xe)
Thrust efficiency η_t	50+%
Thrust (N)	Up to 1.0 mN-s per impulse bit
Lifetime (h)	Not stated

Table 3 Reported performance parameters for an ELF thruster [Slough, Kirtley and Weber 2009 [92]].

4.2 Rotating magnetic field thrusters with a helicon plasma source

The HEAT (Helicon Electrodeless Advanced Thruster) project has investigated the use of rotating magnetic fields and an alternating axial magnetic field to accelerate plasma produced by a helicon plasma source [Kuwahara et al 2015 [98]] (fig 23).

In the rotating magnetic field experiment, the RMF is generated by pairs of coils that are supplied with AC currents that have a phase difference of 90°. An azimuthal plasma current j_θ produced by the effect of the rotating magnetic field reacts with the radial component of the axial field to produce thrust through the Lorentz force $F_t = j_\theta \times B_r$. The RMF was found to accelerate the plasma by 19% compared to the plasma velocity produced by a simple helicon plasma thruster [Furuawa et al 2016 [99]].

In the m = 0 mode in a helicon plasma the current density is at a maximum at the centre of the RF coil and has azimuthal symmetry, an obvious advantage in a thruster. When an AC current is applied to the m = 0 coil that is collinear with the axial field coil (fig 16), it generates an alternating axial magnetic field that, through Faraday's Law, induces an azimuthal plasma current j_θ that reacts with the radial component of the axial field to produce thrust in alternating axial directions. The thrust produced by one-half cycle accelerates the plasma out of the thruster, the accelerated plasma produced by the opposite half cycle collides with the rear wall of the discharge tube.

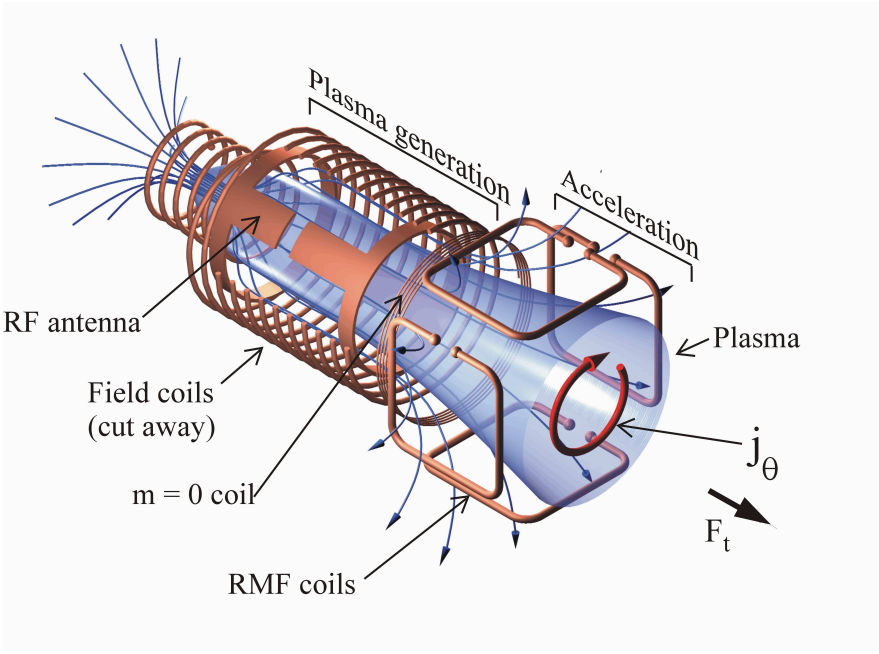

Figure 23 Helicon plasma source with an RMF accelerator (after Kuwahara et al 2015 [98]). The performance of this device is shown in table 4.

Parameter	**Measured value**	
Specific Impulse I_{sp} (s)	Argon	2000
	Xenon	1500
Power efficiency η_P (mN/kW)	Argon	8.3
	Xenon	16
Thrust (mN)	Argon	21
	Xenon	41
Lifetime (h)	Not stated	

Table 4 Reported best performance parameters for a helicon plasma source with an RMF and an m = 0 RF accelerator.

4.3 Rotating electric field thrusters (Lissajous thrusters)

Although a theoretical analysis of the Lissajous plasma accelerator indicated that such a device would produce a specific impulse of 10,000 [Matsuoka et al 2011 [100]], in practice the measured performance has been much less promising.

Work on an experimental thruster that used a rotating electric field to accelerate plasma that had been produced by a helicon source in an expanding magnetic field found that the thrust – if any - produced by the rotating electric field was below the noise signal generated by the thrust stand [Matsuoka et al 2011 [100]]. A later study found that the REF produced a thrust of 4.95μN and concluded that such a value was not useful for practical applications [Nakamura et al 2012 [101]].

Those experimental results show a weak dependence of the ion velocity as a function of the phase difference of the voltages applied to the antenna plates. That result indicates weak electromagnetic acceleration of the plasma and it is considered that most of the power is consumed in ionizing and heating the plasma while the plasma acceleration is mainly due to expansion of the plasma through the magnetic nozzle formed in the diverging field.

4.4 Pulsed inductive plasma accelerators (PIT thrusters)

Pulsed inductive plasma accelerators are spacecraft propulsion devices that store energy in a capacitor and produce thrust by coupling that energy into a propellant by induction from a rising current in a coil that is in close proximity to the propellant [Polzin et al 2007 [102]]. In some devices the electric field that arises from the time varying magnetic field according to Faraday's law ($E = -\frac{d\Phi}{dt}$) ionizes the propellant. In others, the propellant is ionized separately but in both cases the Lorentz force between an induced plasma current and the magnetic field produced by the coil current accelerates the ionized propellant.

Two inherent physical effects have obstructed the development of efficient devices. Firstly, any delay in the ionization of the propellant means that instead of coupling into the ionized gas, energy is dissipated in the coil. Secondly, the maximum amount of energy has to be transferred into the ionized gas before it is driven away from the face of the coil since the coupling between the coil and the ionized gas is a function of mutual inductance that is strongly determined by their separation. The effect is quantified by the Lovberg criterion [Dailey and Lovberg 1993 [103]] that states that the thrust efficiency η_t of pulsed inductive thrusters is limited by the ratio of the total change in circuit inductance ΔL to the initial circuit inductance L_0. That is:

$$\eta_t \leq \frac{\Delta L}{L_0} \qquad \text{Eq. 65}$$

The ratio $\frac{\Delta L}{L_0}$ is maximised when the plasma forms as closely as practical to the surface of the inductor without causing damage to the coil.

The delay in ionization may be addressed by pre-ionizing the propellant with a separate mechanism since pre-ionization permits current sheet formation at lower voltages and discharge energies than in pulsed inductive thrusters that rely solely upon a rapidly changing magnetic field to ionize the propellant. The effect of declining mutual inductance as the plasma sheet moves away from the coil is not so easily resolved and remains a limitation [Jahn 1996 [90]].

In investigations dating back to the 1960s and 70s planar devices were constructed that had thrust efficiencies that ranged from 5% (20cm coil, I_{sp} = 1200s) to 18% (30 cm coil, I_{sp} = 1470s). Larger devices developed in the 1980s were found to have greater thrust efficiencies and specific impulse (1 meter coil, η_t = 42% at I_{sp} = 1540s and η_t = 50% at I_{sp} = 2240s) [Lovberg and Dailey 1981 [104]]. Further investigations using a thrust stand revealed that the figures for the specific impulse and thrust efficiency for the larger device that were calculated from measurements of current density and magnetic fields were overstated by 24% and 42% respectively and demonstrated a fact often overlooked in engineering projects: direct measurements are more reliable than indirect calculations based on unvalidated assumptions.

Since that time engineering developments such as increasing the rate of current rise (dI/dt) and the replacement of spark-gap switches with solid-state devices have led to significant improvements in the performance of these thrusters although up until 2011 the PIT Mark Va developed in the early 1990s remained the most efficient and best performing pulsed inductive thruster (η_t = 55%, I_{sp} = 6000s [Polzin 2007 [102]] (Table 5).

More recent developments that utilize ion cyclotron resonance ionization of the propellant at the face of a conical theta pinch coil are intended to improve the thrust efficiency of these devices [Hallock and Polzin [105]]. Interestingly, a recently developed model [Martin 2016 [106]] that produced a qualitative

agreement with results from tests of the PIT Mk V thruster showed that the optimum coil angle is 90°, that is, a flat plate although a PIT with a coil angle of 60° may have some advantages in propellant utilization that could compensate for any loss in thrust efficiency.

4.4.1 Planar pulsed inductive thrusters without pre-ionization

PIT thrusters without pre-ionization utilize a single inductive coil for both plasma generation and electromagnetic acceleration (fig. 24-1) [Feldman and Choueiri 2011 [107]]. Capacitors deliver a current pulse to the primary coil windings that through Faraday's law ionizes the propellant at the same time as it is injected across the face of the coil (fig 24-2). The reaction between the magnetic field in the coil and the plasma current generates a Lorentz force ($\mathbf{F}_p = \mathbf{J}_{plasma} \times \mathbf{B}_{field}$) that expels the plasma producing a thrust that propels the spacecraft (fig 24-3).

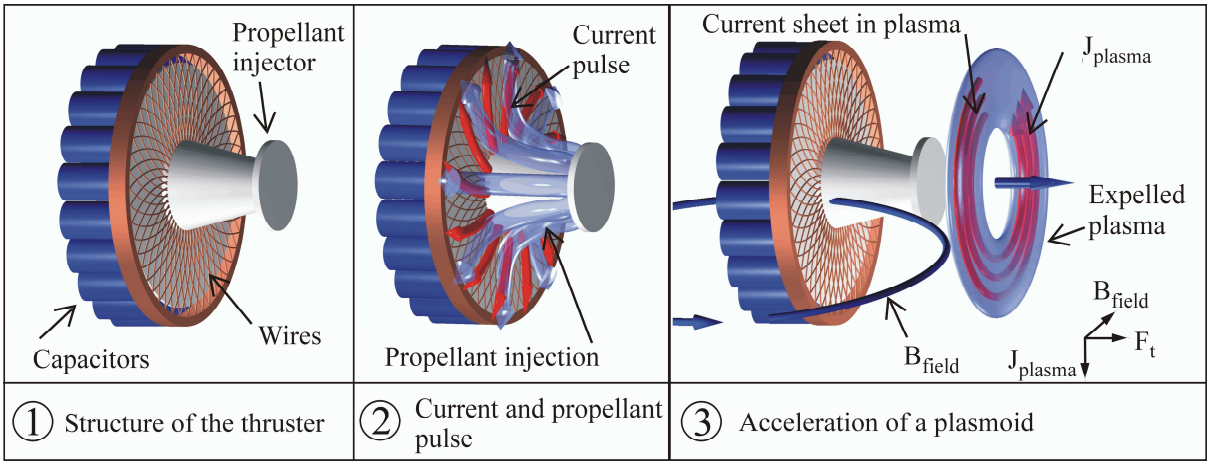

Figure 24 The three phases in the operation of a typical planar pulsed inductive thruster without pre-ionization. Gaseous propellant is ionized by the electric field produced by the rapidly changing magnetic field and the resulting plasma is driven from the thruster by the Lorentz force. The performance of several devices of this design are shown in table 5.

4.4.2 Planar pulsed inductive thrusters with pre-ionization

The FARAD (Faraday Acceleration with Radio-frequency Assisted Discharge) thruster developed in 2004 is a device that typically uses Argon as a propellant, although water vapour, Ne, He, Kr, H_2, O_2, CO_2,Cl, F and Xe are also possible propellants (fig. 25).

The propellant is ionized by a Helicon discharge and the resulting plasma then guided by a magnetic field to flow radially outwards across the face of an inductive coil. In operation, a large azimuthal current, J_{coil}, is pulsed through the coil at a rate $\frac{dJ_{coil}}{dt} \geq 10^{10}\ A/s$.

A current pulse of this magnitude induces a current sheet in the plasma and the induced azimuthal current J_{plasma} in the current sheet interacts with the applied magnetic field, B_{field}, resulting in a Lorentz body force, $J_{plasma} \times B_{field}$ on the plasma.

The resulting force has two components, $j_\theta B_r$ which is axial and accelerates the plasma, and $j_\theta B_z$ which is radial and confines the plasma thereby minimizing damage to the surrounding wall of the thruster.

Thrust is produced by the Lorentz force between the magnetic field produced by the coil current and the induced plasma current sheet [Choueiri and Polzin 2004 [108]].

Reports of the performance of a 100 J per pulse FARAD laboratory thruster have been disappointing. Stated reasons for this outcome were that most of the propellent was not ionized sufficiently for the coil currents to couple to the plasma or was too far from the coil face and in addition, the current sheet was not magnetically impermeable which also reduced the acceleration of the propellant [Polzin, Rose and Miller, 2008 [109]].

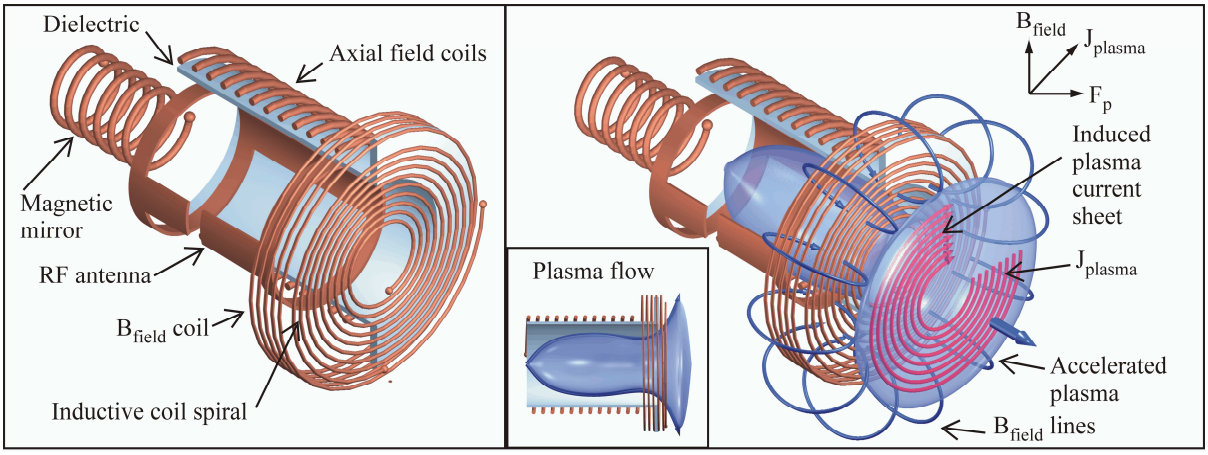

Figure 25 FARAD (Faraday Acceleration with Radio-frequency Assisted Discharge) thruster that uses the $\mathbf{j} \times \mathbf{B}$ force developed by the interaction between an induced plasma current, J_{plasma} produced by a changing current J_{coil} in the inductive coil spiral and a magnetic field, B_{field} produced by the B_{field} coil. Magnetic pressure pushes the plasma away from the coil. The performance of this device is discussed in the preceding text. [after Choueiri and Polzin 2004 [108]].

Later designs have employed an electrodeless Electron Cyclotron Resonance (ECR) pre-ionization scheme that, by a suitable arrangement of permanent magnets, produce a seed plasma which is further ionized by a current pulse through the inductive coil. By employing ECR pre-ionization, Microwave Assisted Discharge Inductive Plasma Accelerators (MAD-IPA) reduce the need for high voltages and a current rise-time sufficient to ionize the cold propellant [Hallock and Polzin 2010 [110]].

4.4.3 Conical PIT thrusters

The single stage FARAD [Feldman and Choueiri 2011 [107]] thruster (SS-FARAD) consists of a single conical antenna coil through which both the ionization and acceleration pulse is applied to the gaseous propellant (fig. 26). The SS-FARAD thruster eliminates external magnetic fields as well as secondary

antennas required for plasma generation and other components required for ionization so is lighter and less complex than previous designs, significant advantages for a compact spacecraft thruster. Recent results indicate that thrusters of this type with smaller conical angles produce greater thrust in contradiction to the predictions of a previous model [Hallock et al 2012 [111]]. Initial measurements made on a conical thruster with a half angle of 20^{o} and an applied voltage of 5kV produced a maximum impulse of 0.097 mN-s with an Argon flow rate $90 < \dot{m} < 150$ mg/s. The investigators suggested that the low thrust of these devices was attributable in part to a large inductive voltage drop in the transmission line from the capacitors to the coil. Other possibilities were a premature current sheet decoupling caused by radial current sheet motion or by an initially radially-displaced current sheet formation point in the thruster.

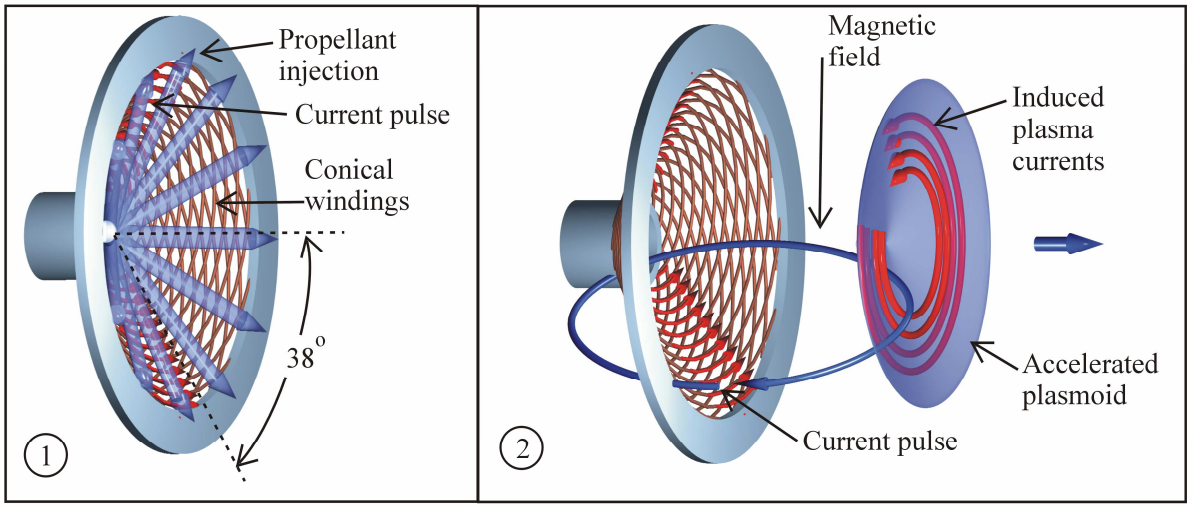

Figure 26 Conical pulsed inductive thrusterwith a 38^{0} half-angle. In frame 1 propellant gas is released over the surface of the conical windings that are assembled in two layers such that the current flows from the smaller radius at the base of the cone to the front of the thruster and then returns in the same azimuthal direction through the lower winding. The windings are separated by an insulating cheet. The rapidly rising current ionizes the propellant through the electric field that arises from the rapidly changing magnetric field according to Faraday's Law. In frame 2 the induced currents in the ionized gas react with the magnetic field produced by the coil currents and that interaction expels the plasma at high velocity. No other ionization process is required [After Hallock et al 2013 [112]]

4.4.4 Erosion of components in the PIT thruster

The lifetime of thrusters that use induction to accelerate plasmas is not limited by erosion of electrodes and contamination of other spacecraft components by the products of erosion is said by the developers not to be an issue in these thrusters although this is an assumption only in the absence of extended testing.

4.4.5 Martian atmosphere used as a PIT propellant.

Investigations have been conducted to examine the possibility of using the components of the Martian atmosphere, primarily carbon dioxide, as PIT thruster propellants derived from in situ resources [Polzin 2012 [113]]. These studies have shown that carbon dioxide derived from the Martian atmosphere could be used as a propellant offering the possibility of using Martian resources to reduce the return journey propellant mass required to be transported from Earth.

4.4.6 Current status of PIT thrusters

Thruster	I_{sp} **(s)**	**Thrust efficiency** η_t	**Energy (J) per pulse**	**Reference**
Plasmoid thruster experiment (PTX)	500 to 4300	0.4 to 49%	280	Eskridge and Martin 2007 [114]
30 cm PIT*	1470	18%	675	Polzin 2011 [115]
1 meter PIT	1236	25.4%	4840	Polzin 2011 [115]
PIT Mk 1 (NH_3)	1360 (worst)	21.3%	4840	Dailey and Lovberg 1993 [116]
	2766 (best)	31.9%	5760	
PIT Mk Va (NH_3)	6000	~55%	~4000	Polzin 2011 [115]
PIT Mk VI	2750	18.9%	4050	Polzin 2011 [115]
Conical Theta Pinch PIT	1500 to > 4500 (Ar), 1000 - 2500 (Xe)	5% (single pulse)	500	Hallock et al 2015 [117]

Table 5 Reported performance parameters for PIT thrusters. *Values calculated from field measurements are probably an overestimate (section 4.4).

4.5 Helicon thrusters

Helicon thrusters consist of a helicon-type antenna providing energy to a plasma source attached to a magnetic nozzle that transforms the randomized thermal energy of the plasma into directed kinetic energy (fig 27).

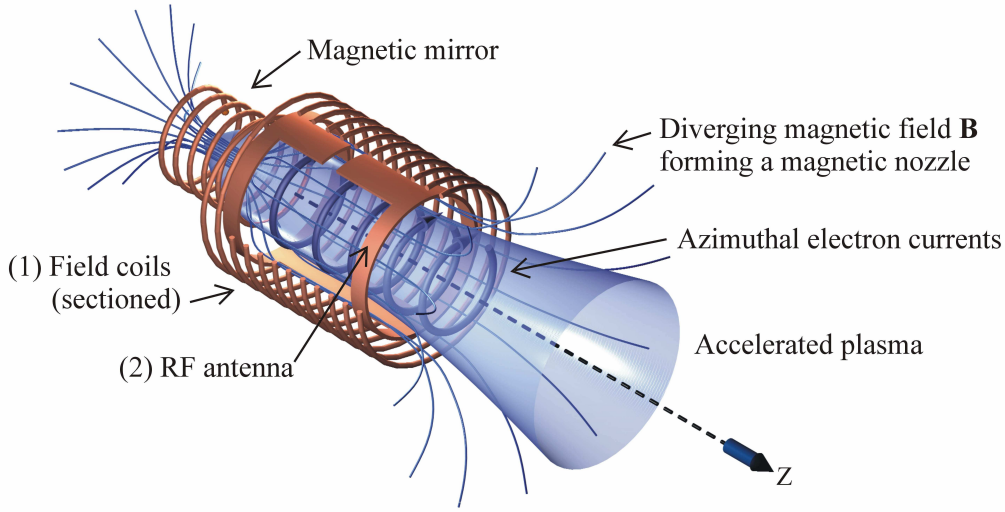

Figure 27 Generalized Helicon type thruster showing the principal components: The field coils that produce the magnetic field **B** that forms the confining field and the magnetic nozzle and the helicon antenna, usually placed inside the field coils, that supplies the RF power that provides the energy to the generate the plasma from the propellant. The plasma is accelerated by the magnetic nozzle described in section 3.2.2. A magnetic mirror prevents plasma from flowing out of the rear of the plasma source.

In simple helicon-type thrusters, a significant part of the thrust is produced by plasma pressure that develops against the back wall of the thruster. Energy is lost from the plasma to the back wall of the thruster through the sheath and the bombardment of the back wall by the plasma causes damage by sputtering as well as a reduction in the thrust efficiency η_t. Since nearly all of the energy supplied to the thruster is consumed in ionizing the propellant, losses to the back wall are nearly equal to that lost to the plasma expelled from the exit, effectively halving the thrust efficiency. Plasma confinement by magnetic mirrors (section 3.3) is well understood and is an effective means of reducing plasma losses to the back wall and improving the thrust efficiency of a radio frequency heated plasma thruster.

The relatively low ion temperature of 0.3eV produced by helicon-type sources [Nakamura et al 2012 [71]] is another factor that reduces the effectiveness of simple helicon-type thrusters since, being effectively an electrothermal thruster, the specific impulse is proportional to the square root of the plasma energy and therefore its temperature. In the absence of other means of accelerating the plasma, the specific impulse I_{sp} of approximately 200s is not less than that of many chemical rockets [Cohen et al 2006 [20]].

A recent review [Navarro-Cavalle et al 2013 [118]] has summarised the performance of representative helicon-type thruster prototypes and highlighted the design parameters: The following table (Table 6) is an extract from that paper with some additions.

Prototype	Isp (s)	η_t (%)	Thrust	Life (h)	η_m (%)	Power	Ref.
Mini Helicon Thruster Experiment (mHTE)	1000 - 4000	18 to 20	10mN	Not given	90	700W to 1100W	Batishchev 2009 [119]
Helicon Plasma Hydrazine Combined Micro (HPHCOM)	1200	13	1.5mN	Not given	90	50W	Pavarin et al 2008 [120]
	422	13	0.5mN	Not given	-	8W	Trezzolani et al 2013 [121]
Permanent Magnet Expanding Plasma (PMEP)	500	1	3mN	Not given	<50	700W	Takahashi et al 2011 [122]
High Power Helicon Thruster (HPHT)	4750 (H_2)	-	-	Not given	-	30kW	Ziemba et al 2005 [123]
Helicon Double Layer Thruster (HDLT)	280	≤1	1 to 2.8mN	Not given	-	250W to 650W	Pottinger et al 2011 [124]
Permanent magnet helicon plasma thruster (PM-HPT)	2000	7.5	15mN	Not given	-	2kW	Takahashi et al 2013 [125]

Table 6 Summary of prototype helicon-type thrusters [Navarro-Cavalle et al 2013 [118] and others]. η_m is the propellant utilization efficiency. Values are given where available.

4.5.1 Helicon double layer thruster (HDLT)

In 2003 a group at the Australian National University, following earlier work [Hairapetiat and Stenzel 1991 [126]], reported that an electric double layer (DL) that formed in a plasma in a diverging magnetic field appeared to produce an ion beam, useful as a thruster [Charles 2003 [127]] (fig. 28). An RF antenna that was wave coupled to the propellant gas produced the plasma. A calibrated pendulum thrust stand whose displacement was determined by the deflection of a laser beam measured the thrust and a retarding field energy analyser (RFEA), in its basic form consisting of a grid and a plate, measured the axial velocity of the exhaust. The graph shows the step in the plasma potential created either by an electrical double layer [Charles 2003 [127]] or by a pre-sheath acceleration of ions [Chen 2006 [84]].

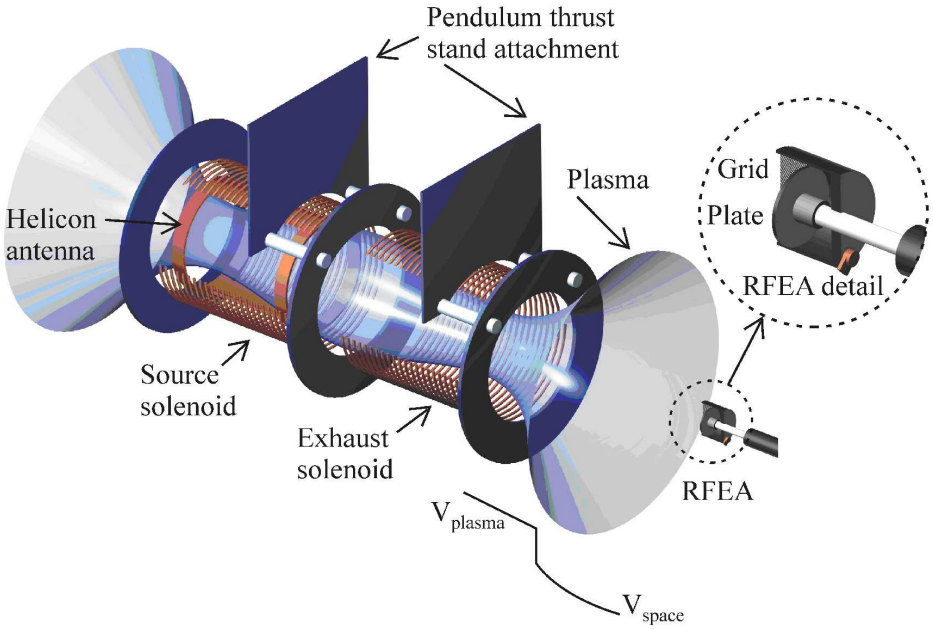

Figure 28 Helicon double layer plasma thruster showing the main components of the ANU experiment. The curve below the device shows the step in potential that occurs between the plasma and space as the plasma expands.

4.6 Plasma thrusters using traveling waves in a transmission line

Plasma can be accelerated by the Lorentz force associated with a moving magnetic field produced by travelling waves of voltage and current that propagate along transmission lines when either a pulse of current or a source of alternating current is applied to one end of the line. In either case, the propagation velocity is given by:

$$v_p = 1/\sqrt{LC} \qquad \text{Eq. 66}$$

Where L and C are respectively the inductance and capacitance of the elements of the line (fig 29).

In most systems the propagation velocity is of the order of 10^4 m/s to 10^5 m/s [Fabris and Capelli [128]].

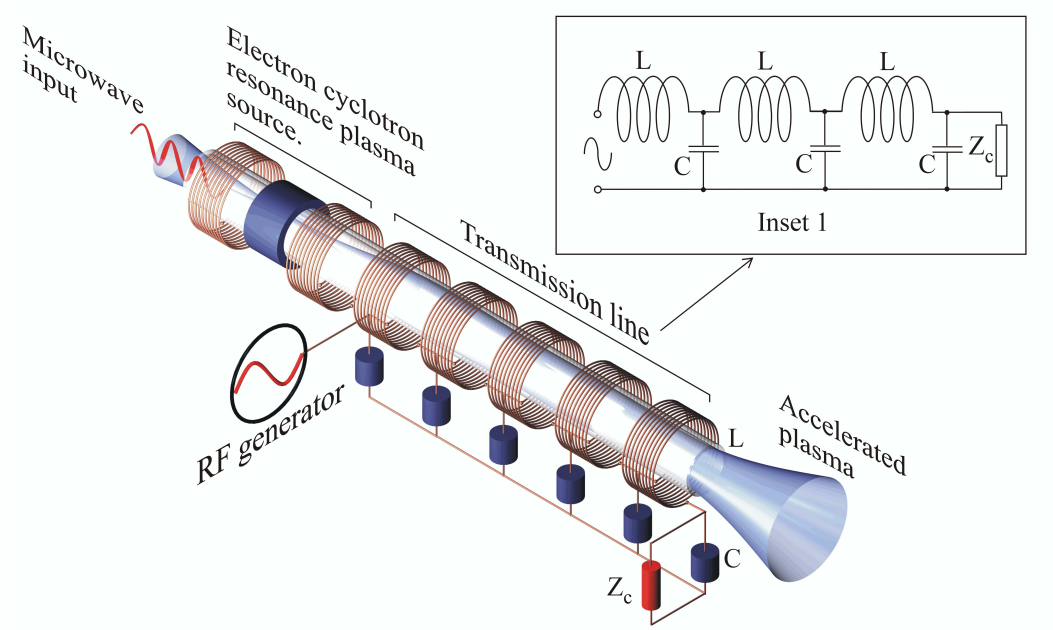

Figure 29 Traveling wave plasma accelerator. Plasma, generated for instance by an electron cyclotron resonance source, is accelerated by the traveling axial magnetic field produced by the waves that propagate along the transmission line when alternating current or a current pulse is fed into the line. To prevent reflections of the waves, the transmission line has to be terminated with a characteristic impedance Z_C (inset 1).

Transmission line accelerators using helium as a propellant were investigated in the 1960s [Helfinger et al 1965 [129]] however those were high power (160kW) devices that employed large currents to generate a magnetic field strength sufficient to accelerate plasma in a water cooled thruster tube. A slightly later investigation [Palmer and Jones 1967 [130]] reported lower efficiencies that were ascribed to the fact that the device was limited to operating at a much lower power (13kW) since the accelerator tube was not water cooled. In those experiments, the greatest thrust efficiency η_t (7.5%) was obtained when operating with argon as a propellant when the accelerator length corresponded to a ¼ wavelength of the RF input whereas when xenon was used the greatest thrust efficiency η_t (6%) was obtained with an accelerator length of one wavelength. The specific impulse obtained with argon was 2200 s and for xenon, 1200 s.

A low power device developed in a more recent investigation [Feraboli et al 2015 [131]] uses either an ion cyclotron resonance or helicon plasma source to produce an argon plasma. The plasma is accelerated by propagating magnetic fields with velocities from 5,000 m/s to 25,000 m/s that are produced by pulses applied to a sequentially switched series of coils at a repetition rate of 5Hz. The energy of the pulses delivered to each coil was 0.014J and the overall power was 9.8W.

An interaction between the plasma and the propagating magnetic field has been observed however, no measurements of specific impulse, thrust efficiency or thrust have yet been published.

4.7 Plasma thrusters using a HiPIMS ion source with a magnetic nozzle

The development of high power impulse magnetron sputtering discharge technology (HiPIMS) [Kouznetsova et al 1999 [132], Gudmundsson et al 2012 [133]] together with improvements in the understanding of the physics of magnetic nozzles [Takahashi et al 2014 [134]] has encouraged this investigation into the combination of these devices with the intention of producing a thruster with greater thrust efficiency and thrust than existing solid propellant plasma thrusters.

The HiPIMS thruster [Bathgate et al 2016 [135]] (fig. 30), utilizes ions of target material and has no electrodes that may be subject to ion bombardment (other than the metallic propellant mass). Copper was used in this device since it known to support self-sputtering [Anders and Andersson 2008 [136]]. That is, once sputtering has been initiated either with a pulse of gas or with a laser, the process will continue to produce thrust without the need to re-start sputtering and importantly for a spacecraft, the thruster will operate continuously in a high vacuum. At high power intensities the density of the sputtered copper atoms is so great that a considerable number of copper atoms are ionized by collisions with plasma electrons. These copper ions are accelerated by the cathode voltage and sputter the copper target even in a vacuum [Kukla et al 1990 [137]]. The emission of ions and electrons from the magnetron source is initiated by bombardment of the target with argon ions from a pulse of gas that is energized by a high intensity current pulse. Thrust F_t is produced by the acceleration of copper ions by the Lorentz force in the magnetic nozzle that are expelled from the target.

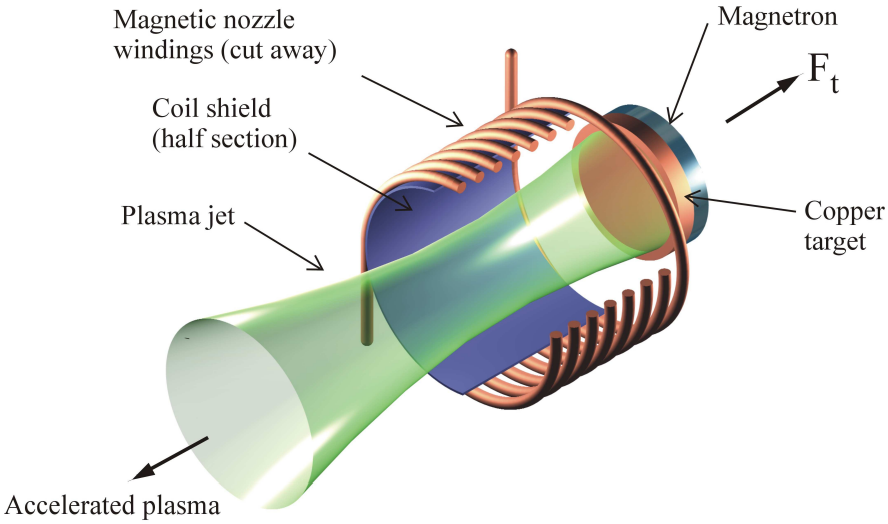

Figure 30 A HiPIMS plasma source located at one end of a current-carrying solenoid produces ions and electrons that are accelerated by the diverging magnetic field that exists at the ends of a solenoid.

Parameter	**Measured value**
Specific Impulse I_{sp} (s)	1543 (Copper)
Thrust efficiency η_t	6%
Thrust (N) @ input power	3.77μN @ 3.6kW
Lifetime (h)	Not evaluated

Table 7 Measured performance of a HiPIMS copper ion thruster [Bathgate et al 2016 [135]].

5 Power supplies for plasma thrusters

A description of the power supplies used to drive plasma thrusters and an analysis of the disposal to space of waste heat produced by those devices.

Unlike chemical rockets where the energy content of the propellant is fixed, the total energy available to a plasma thruster may be much greater since it is only limited by the durability of the power supply that generates the electrical energy needed to produce and accelerate the plasma. Presently, only nuclear reactors, radioisotope thermoelectric generators and solar photovoltaic cells are capable of generating electrical power for the length of time required to produce significant velocity increments for spacecraft propelled by plasma thrusters.

5.1 Nuclear reactors

Space rated nuclear power supplies have been developed and deployed in the past and NASA is currently developing a 100kW electrical generator based on a small fission reactor that has a mass of 512kg. The SAFE 400 (Safe Affordable Fission Engine) (Poston et al 2002 [138]), reactor is used as a heat source to drive a closed cycle gas turbine engine (Brayton cycle) that has a thermal efficiency of 25% [Russell and Cohen 2012 [139]]. The objective of the project is to demonstrate an integrated propulsion system that converts thermal energy from a nuclear heat source into jet power using a heat engine driving an electrical generator and a plasma thruster.

5.2 Radioisotope thermoelectric generators

Radioisotope thermoelectric generators have been employed as electrical power sources in United States spacecraft since 1961 [Rinehart 2001 [140]] and all have used the natural decay of the isotope Plutonium-238 as a source of heat that is converted to electrical energy through the Seebeck effect by an array of thermocouples. Recent missions including Galileo (to Jupiter), Ulysses (that orbited the Sun), Cassini (to Saturn) and New Horizons (to Pluto) employed the General Purpose Heat Source-RTG (GPHS-RTG) that generates a nominal 285 watts of electrical power with an efficiency of approximately 6%. To date no RTG power supplies have been employed as energy sources for plasma thrusters.

5.3 Solar photovoltaic power supplies

To date, the largest solar photovoltaic system deployed in space is the 260kW power supply installed on the International Space Station [Brophy et al 2011 [141]]. Larger systems suitable for missions beyond low Earth orbit are under consideration and investigators working for NASA's Human Exploration Framework Team (HEFT) have developed a conceptual design

of a 300-kW solar electric propulsion (SEP) system using state of the art equipment. The HEFT study concluded that the use of high-power SEP systems makes the architecture significantly less sensitive to mass growth in other in-space elements, improves mission flexibility, provides more graceful propulsion system failure modes, makes substantial power available at the destination and during coast periods and has the potential to be reusable [Brophy et al 2011 [141]].

The application of electrodeless thrusters is presently constrained by the large currents that are required to produce significant acceleration fields and are restricted to pulsed operation because of limitations in the output of power supplies driven by SEP systems.

In turn, the limited output of SEP power supplies requires that for a typical mission, the power train must be capable of producing more than 10^9 pulses [Dankanich and Polzin 2009 [142]].

5.4 Limitations on spacecraft power supplies imposed by radiator size.

Given that no power supply is 100% efficient, a proportion of the energy produced by a spacecraft power supply is lost as heat that has to be removed since the temperature of power supply and related components usually has to be kept below 70°C [de Grys et al 2005 [143]]. In space, waste heat can only be shed to space through a radiator and as the size of the power supply increases, the size of the radiator increases in proportion and eventually becomes a limiting factor [Semyonov 2014 [144]].

An ideal radiator emits thermal radiation with a black body spectral distribution where the radiated power P_b is given by Stefan's Law:

$$P_b = S_r \sigma_B T^4 \ \text{W/m}^2 \qquad \text{Eq. 67}$$

Where S_r is the area of the body, $\sigma_B = 5.67 \times 10^{-8}\,\text{W/m}^2/\text{K}^4$ is the Stefan-Boltzmann constant and T is the temperature.

So long as the radiator surface is orientated to minimise the effect of solar heating, the ambient radiation received by the radiator will be from the black body background of the universe that has a temperature of $T_{amb} = 2.7K$ [Hawking and Ellis 1968 [145]].

The area of an ideal radiator required to cool a power supply with an output P_s is then:

$$S_r = P_s(1-\varepsilon_i)/\sigma_B \varepsilon_r \left(T_r^4 - T_{amb}^4\right) \qquad \text{Eq. 68}$$

Where ε_i is the internal efficiency of the power supply, ε_r is the thermal emissivity of the radiator and T_r is the radiator temperature.

If a spacecraft's energy is produced by a heat source such as a 400kW (thermal) nuclear reactor like the SAFE 400 [Poston et al 2002 [138]], a heat engine is required to generate mechanical power and a radiator is required to dispose of the waste heat from that engine. This means that the size of the radiator is determined by the Carnot efficiency of the heat engine in

addition to the energy efficiency of the power supply that may be an alternator driven by the heat engine. The Carnot efficiency η_c is defined as:

$$\eta_c = \frac{T_{in} - T_{out}}{T_{in}} \qquad \text{Eq. 69}$$

Where T_{in} is the heat engine inlet temperature and T_{out} is the outlet temperature, in this case corresponding ideally to the radiator temperature T_r.

Since the Carnot efficiency of a heat engine is a function of the difference between the inlet and outlet temperatures and the inlet temperature T_{in} is limited by materials, making the outlet temperature T_{out} as low as possible is desirable. However, since the radiated power is proportional to T_r^4, the radiator size increases rapidly with falling radiator temperature so that a small gain in Carnot efficiency may require a large increase in radiator size. For instance, if a 100kW heat engine has an inlet temperature of 773K (500^{o}C), reducing the radiator temperature from 323K (50^{o}C) to 298K (25^{o}C) will increase the thermal efficiency from 58% to 61% however the radiator surface area will more than double from 161m^2 to 361m^2. The required radiator surface area thus becomes increasingly significant as the output of the power supply increases and places a practical limit on the size of the power supply. In practice, the radiator temperature varies from the inlet to the outlet as heat is lost so that the radiated power varies across the radiator surface. For example, a closed Brayton Cycle system [Harty et al 1994 [146]] has a radiator inlet temperature of 401K and an outlet temperature of 283K, a difference of 118K across the radiator. The following chart shows the effect of radiator temperature and internal energy efficiency ε_i (Carnot efficiency x power supply efficiency) on radiator dimensions (fig. 31).

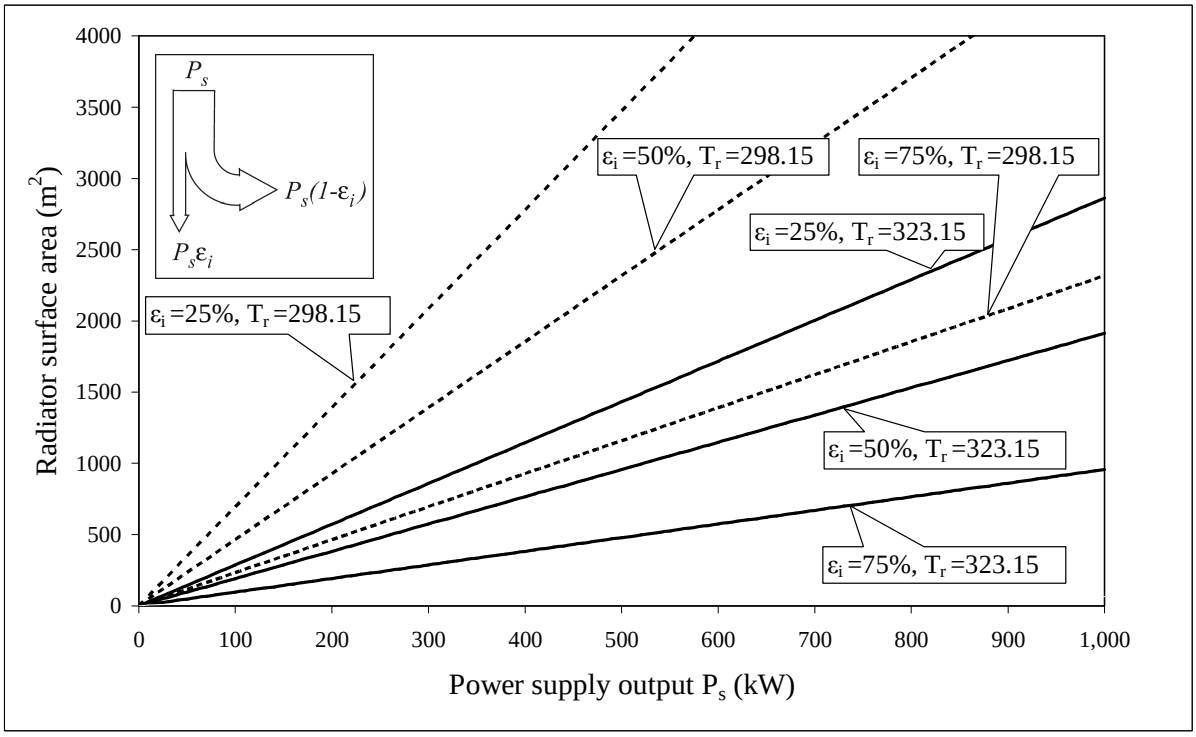

Figure 31 Surface area of a radiator used to cool a spacecraft power supply as a function of the power supply output for internal energy efficiencies ε_i of 25%, 50% and 75% at two different radiator temperatures, T_r = 298.15K and T_r = 323.15K Solid lines are for radiator temperatures of 323.15K (50°C). Dotted lines are for radiator temperatures of 298.15K (25°C). The emissivity $\varepsilon_r = 0.9$ and the black body temperature of space is 2.7K. The inset shows the proportion of output of the power supply $P_s(1-\varepsilon_i)$ that is lost as heat that has to be radiated to space.

6 Erosion in thrusters with electrodes

A description and analysis of the erosion of electrodes by sputtering in plasma thrusters with electrodes.

Erosion of electrodes is the primary factor that limits the life of gridded ion, Hall and MPD thrusters. As thruster powers grow and mission durations extend, electrodeless thrusters that are not limited by erosion of electrodes will become more important. Thrusters may be required to operate for as much as 120,000 hours while expelling 2000Kg of propellant [Rovey and Gallimore 2008 [147]], a requirement that exceeds the capacity of existing thrusters with electrodes (Table 2).

6.1 Erosion in gridded ion thrusters.

Low thrust gridded ion thrusters such as the type used in Dawn [Brophy et al 2006 [148]] must operate for tens of thousands of hours in order to achieve the velocity increment required. Although the grids are highly durable, significantly greater specific impulses required for extended missions will aggravate the known wear mechanisms of gridded ion thrusters. Of primary concern are the effects of charge-exchange ions that are generated between the screen grid and the accelerator grid. Subject to the strong inter-grid electric field, these ions achieve kinetic energies sufficient to erode the accelerator grid and their energies and those of charge-exchange neutrals are roughly proportional to the applied acceleration voltage V_B since the exhaust velocity v_e and hence the energy of the ions is a function of the square root of V_B :

$$v_e = \sqrt{\frac{2qV_B}{m_{ion}}} \qquad \text{Eq. 70}$$

I_{sp} is given by:

$$I_{sp} = \frac{1}{g_0}\sqrt{\frac{2qV_B}{m_{ion}}} \qquad \text{Eq. 71}$$

So that the required acceleration voltage V_B for a particular I_{sp} and ion mass m_{ion} is then:

$$V_B = \frac{m_{ion}}{2q} g_0^2 I_{sp}^2 \qquad \text{Eq. 72}$$

Erosion of the accelerator grid by charge-exchange ions is one of the major failure mechanisms that limit the life of gridded ion thrusters and since the energies of charge-exchange ions increase with V_B, damage to the accelerator grid grows as the square of the specific impulse I_{sp} (Eq. 72) [Brophy et al 2002 [149]] (fig. 32).

Measurements show that the erosion rates of grid materials are either linear with V_B or fit a polynomial of power approximately 1.4 V_B [Duchemin et al 2000 [150]]. Other reports state that to operate thrusters with molybdenum grids for more than a few thousand hours, the beam

current densities have to be operated at levels much less than the maximum possible because the grid erosion rate increases with beam density [Meserole 2001 [151]].

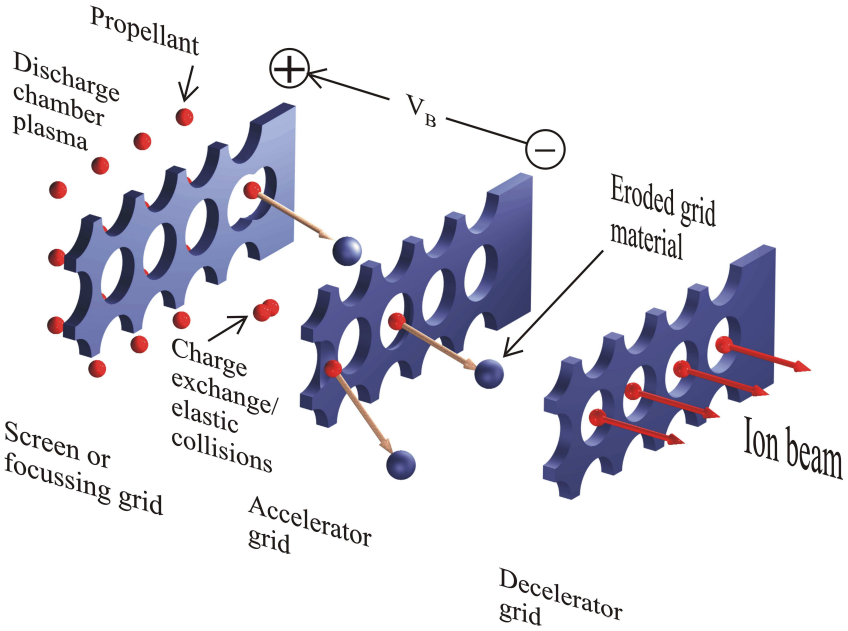

Figure 32 Erosion mechanisms in gridded ion thrusters. Particles (ions and neutrals) produced by charge exchange and elastic collisions in ion thrusters can be directed toward the accelerator and/or decelerator grid with very high energies. The impact of these particles erodes the grids and the end of life is reached when either the holes in the accelerator grid become so large that ion extraction is greatly affected by electron back streaming or structural failure occurs in the grid.

Electrodeless thrusters can, according to their developers, be operated at powers far greater than a few kilowatts and are inherently immune to this type of malfunction.

6.2 Erosion in Hall thrusters.

Hall thrusters generate thrust by the interaction of an electric current in a plasma with an applied magnetic field that is radial and perpendicular to the discharge channel walls (fig. 33). This interaction creates an electric field that is mostly parallel to the walls of the discharge channel and it is this electric field that accelerates the ions to high velocities and produces the thrust. Hall thrusters are effectively gridless ion thrusters. The plasma produces an electric field parallel to the radial magnetic field lines and this field accelerates ion towards the discharge chamber walls causing erosion by sputtering. Erosion of the covers protecting the magnetic circuit components from the discharge plasma is the principle failure mechanism of Hall thrusters [Cheng and Martinez-Sanchez 2007 [152]]

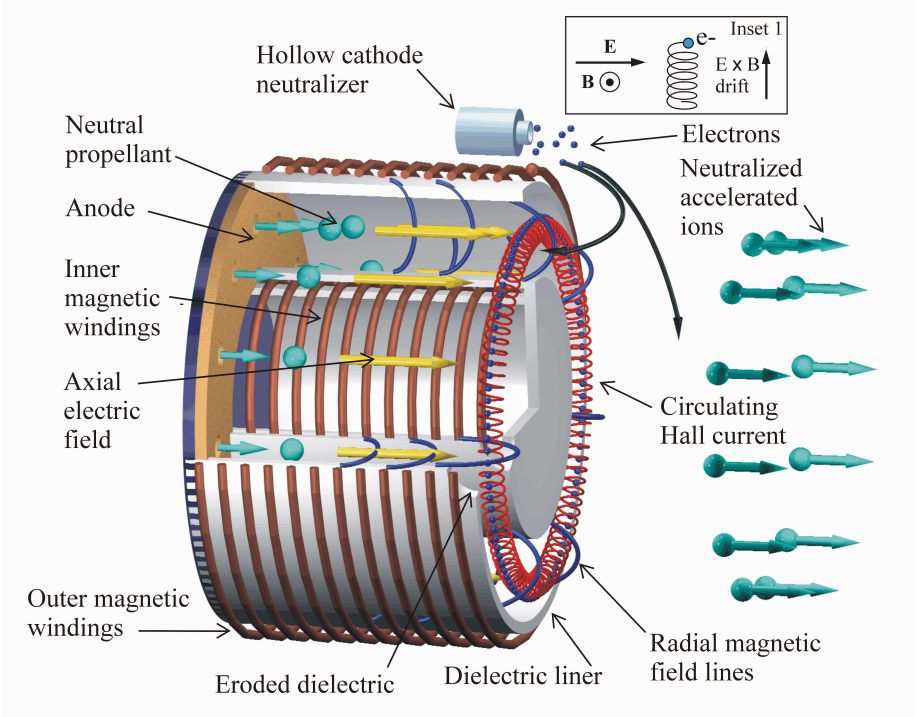

Figure 33 Section through a Hall thruster showing **E x B** drift of electrons in crossed electric and magnetic fields (Inset 1) and erosion of walls and exit rings that protect the magnetic components. In a Hall thruster, electrons are emitted from a cathode located at the exit of the thruster while neutral propellant is admitted into the base of the discharge chamber. Some of the electrons enter the discharge chamber and are trapped along the magnetic field lines and create a Hall current in the **E x B** direction. The resulting increase in electron residence time leads to an efficient ionization of the propellant and an increase of the axial electric field that accelerates the ions that are neutralized by other electrons emitted by the cathode.

Recent investigations have shown that a unique configuration of the magnetic field and channel geometry near the wall of Hall thrusters, called “magnetic shielding”, can be used to reduce wall erosion by orders of magnitude [Goebel et al 2013 [153]]. A Hall thruster with magnetic shielding and with a specific impulse of 3000 s operated for a wear test of 113 hours at a power density 50% higher than nominal without significant damage [Hofer et al 2013 [154]]. The use of magnetic shielding allows the replacement of ceramic walls in Hall thrusters with graphite or temperature resistant metals without significant performance penalties and may open the design space for lighter, higher-power, lower-cost Hall thrusters that are not significantly life limited by wall erosion [Goebel et al 2013 [153]]. Despite this advance, sputtering erosion of the cathodes may still limit the durability of Hall thrusters.

6.3 Erosion in Magneto Plasma Dynamic (MPD) thrusters

The development of early versions of magneto plasma dynamic thrusters was hampered by thermal and chemical erosion of the electrodes and walls of the devices (fig. 34).

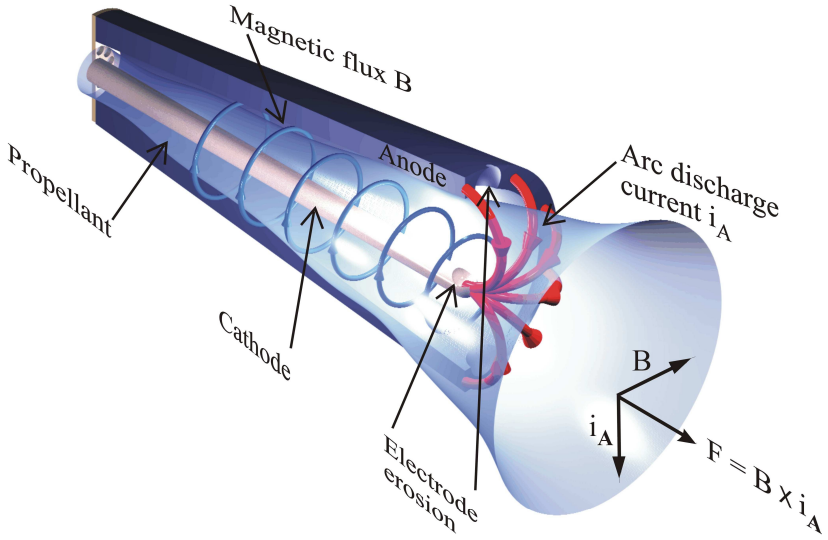

Figure 34 Section of a self –field MPD thruster showing erosion of the anode and cathode. Neutral propellant is introduced into the discharge chamber where it is ionized and then driven from the thruster at high velocity by the Lorentz force produced by the interaction of the ions and the magnetic field that results from the passage of a current between the anode and the cathode [After Sankaran et al 2003 [155]].

Since then, the development of MPD thrusters has been further hampered by poor efficiency primarily caused by energy being deposited into the anode by electrons accelerated into the anode surface by the anode fall voltage that develops in the region near the anode surface. Investigations have shown that the Hall term in Ohm's law causes depletion of the plasma near the anode surface which produces the anode fall voltage and current and voltage oscillations that are associated with rapid electrode erosion [Hoyt 2005 [156]].

The low thrust efficiency η_t that results from frozen flow losses and the large fraction of the input power that is dissipated as heat in the anode is compounded by the fact that the regime in which MPDs start to become efficient is also that in which cathode erosion rates tend to be prohibitive [Choueiri and Ziemer 2001 [157]].

Recent investigations that show that electrode erosion is not significant in MPD thrusters with thrust efficiencies of 6% to 12% may support these earlier findings [Boxberger et al 2012 [158]].

High power (~30 kW) applied-field MPD thrusters running on ammonia and lithium have been operated successfully for 100 and 500 hours respectively, although significant erosion was measured. There is some evidence that a modest applied magnetic field can reduce erosion and increase lifetime in high power MPDs [Kodys and Choueiri 2005 [49]].

7 Summary and conclusions

An analysis of the reported performances of the most promising electrodeless thrusters and a discussion of further developments.

The following table lists the performances of the electrodeless thrusters discussed in the previous section that have reached a stage of development where some may be considered for deployment (Table 8).

Thruster	I_{sp} **(s)**	**Thrust efficiency** η_t	**Thrust**	**Specific mass**
Electrodeless Lorentz Force thruster (ELF)	1000 to 6000	50+%	Up to 1.0 mN-s per impulse bit	0.7kG/kW (Brown et al 2010 [55]) scaled to 200kW
Pulsed Inductive Thruster (PIT) Mk Va	6000	55%	-	8kG/kW (Lovberg and Dailey 1996 [103])
Plasmoid thruster experiment (PTX)	500 to 4300	0.4 to 49%	-	-
Helicon Plasma Hydrazine Combined Micro (HPHCOM)	1200	13%	1.5mN	-
Conical Theta Pinch PIT	1500 to > 4500 (Ar), 1000 to 2500 (Xe)	5% (single pulse)	1.5mNs (Ar)	-

Table 8 Summary of electrodeless plasma thrusters ordered by performance with values that are given where available.

It is evident that the Electrodeless Lorentz Force Thruster has the greatest potential for near-term deployment since even though the specific mass of the thruster may have been reduced by the effect of scaling, it is approximately an order of magnitude better than the next best device, the PIT MkVa pulsed inductive thruster, developed in the 1990s that has a similar specific impulse. The development of the ELF has resulted in a useful device while progress in developing new forms of the pulsed inductive thruster with greater thrust efficiency have been hampered by difficulties in understanding the physics of those devices. That concern is exemplified by the results of tests of conical PIT thrusters while a recently published model has shown that the most thrust efficient PIT thruster is similar to the original flat plate devices

and suggests that attempts to improve conical PITs will prove difficult although the conical PITs may have some advantages in propellant utilization efficiency.

A similar device, the pulsed plasmoid thruster (PTX), achieves a thrust efficiency approaching that of the ELF although it is still in an early stage of development. Considering its similarity to conical PITs, the high thrust efficiency claimed for that device needs to be confirmed.

Much effort has been expended in the development of helicon thrusters that have the attraction of simplicity yet the low plasma temperature of those devices continues to impede their development. Some improvement in thrust efficiency has been achieved by adding an acceleration stage to the outlet of the device although at the cost of increased complexity. The electric double layer that forms in plasma in diverging magnetic fields was initially believed to be responsible for the acceleration of plasma yet an analysis has shown that the increase in velocity in plasma in the helicon double layer thruster is more likely caused by the effect of the magnetic nozzle that forms in the diverging field. Recent work with high power helicon plasmas has demonstrated the formation of a double layer that apparently produced an ion beam with energies in excess of 65eV suggesting that the double layer is responsible for some fraction of the observed acceleration. More work is required to establish these devices as useful thrusters.

Other electrodeless thruster mechanisms – such as travelling wave accelerators – may prove practical however much work will be required before those devices are able to challenge the most developed technologies.

Extended lifetime measurements are still required for each of these devices however the absence of electrodes that may be subject to erosion and the preliminary data available suggests that electrodeless plasma thrusters will predominate as mission durations extend and power levels increase.

As this investigation has shown, new technologies continue to be developed, with some building on progress in different fields such as the rotating magnetic field thrusters where the device was originally conceived as a means of heating and confining plasma for fusion. The HiPIMS thruster discussed in this thesis falls into that category of devices. Others, like the pulsed inductive thrusters, are part of a long-term process of improvement of an original design while at the same time entirely new devices such as the magnetic reconnection thruster discussed in this thesis have their origins in the investigation of phenomena that produce jets of high-speed particles in astrophysical objects.

And while the advent of a fusion rocket would remove electric thrusters from the role of primary thrust producers, until that time electric thrusters will continue to displace chemical thrusters for satellite station keeping and for interplanetary missions requiring a high specific impulse [Cassibry et al 2015 [159]].

8 A plasma thruster using a magnetic nozzle with a HiPIMS plasma source

A report on the development of a plasma thruster that uses high-power impulse magnetron sputtering (HiPIMS) together with a magnetic nozzle to produce a high velocity jet of ionized copper.

8.1 Introduction

Plasma thrusters that use solid propellants, such as the Teflon pulsed plasma thruster [Martinez-Sanchez and Pollard 1998 [160]], have been used for several decades to manoeuvre spacecraft. Although the thrust efficiency (η_t) and the thrust of such devices (F_t) [Markusic et al 2005 [161]] are low, their simplicity and reliability have made them useful for tasks such as station keeping and attitude control for communications satellites.

The development of high power impulse magnetron sputtering discharge technology (HiPIMS) [Kouznetsova et al 1999 [162], Gudmundsson 2012 [163]] together with improvements in the understanding of the physics of magnetic nozzles [Takahashi et al 2014 [164]] has encouraged this investigation into the combination of these devices with the intention of producing a thruster with greater thrust efficiency and thrust than existing solid propellant plasma thrusters. A HiPIMS plasma source produces a highly ionized flux of the sputtered material effectively coupling the propellant to a magnetic nozzle. Justifying the development of such devices, recently deployed plasma thrusters have demonstrated velocity increments (Δv) per kg of propellant defined as propellant efficiency (ε_p) 10 times that attainable with chemical thrusters. Laboratory experiments have shown that the incorporation of a magnetic nozzle into a plasma thruster may increase the specific impulse I_{sp} by as much as 30% by converting a proportion of the thermal energy of the jet into directed kinetic energy in a process analogous to the effect of a De Laval nozzle on the velocity of the propellant in chemical rockets [Winglee et al 2007 [165]].

This discussion is a report on the first evaluation of a prototype plasma thruster that combines a solid propellant HiPIMS plasma source, a device not previously employed as a thruster, with a magnetic nozzle (fig 35). A DC magnetron source coupled to a magnetic nozzle has been previously reported [Madocks 2006 [166]] however that device ionizes a gas flow instead of producing ions from the target. The aim of this investigation was to demonstrate the advantages of the HiPIMS thruster since it utilizes ions of a target material and has no electrodes that may be subject to ion bombardment (other than the metallic propellant mass) and to determine if it has a greater specific impulse than existing chemical thrusters.

A similar experiment measuring the effect of an axial magnetic field on the deposition of aluminium from a HiPIMS discharge has been previously reported [Bohlmark et al 2006 [167]]. Those measurements reported an increase in the deposition rate of 80% in the area of the substrate that was aligned with the axis of the solenoid and much lower deposition away from the axis. The aim of this investigation was to determine the characteristics of a thruster consisting of a HiPIMS ion source coupled with a magnetic nozzle that takes advantage of the axial concentration of the ion beam. Such a device has the advantage that it lacks electrodes (other than the metallic propellant mass) that may be subject to ion bombardment.

Copper was selected for this study since it known to support self-sputtering [Anders and Andersson 2008 [168]] although sustained self-sputtering was not attempted in this experiment since inadequate cooling made it impractical to run the discharge at the high average power levels required. In self-sputtering once sputtering has been initiated either with a pulse of gas or with a laser, the process will continue to produce thrust without the need to re-start sputtering and importantly for a spacecraft, the thruster will operate continuously in a high vacuum. At high power intensities the density of the sputtered copper atoms is so great that a considerable number of copper atoms are ionized by collisions with plasma electrons. These copper ions are accelerated by the cathode voltage and sputter the copper target even in a vacuum [Kukla et al 1990 169].

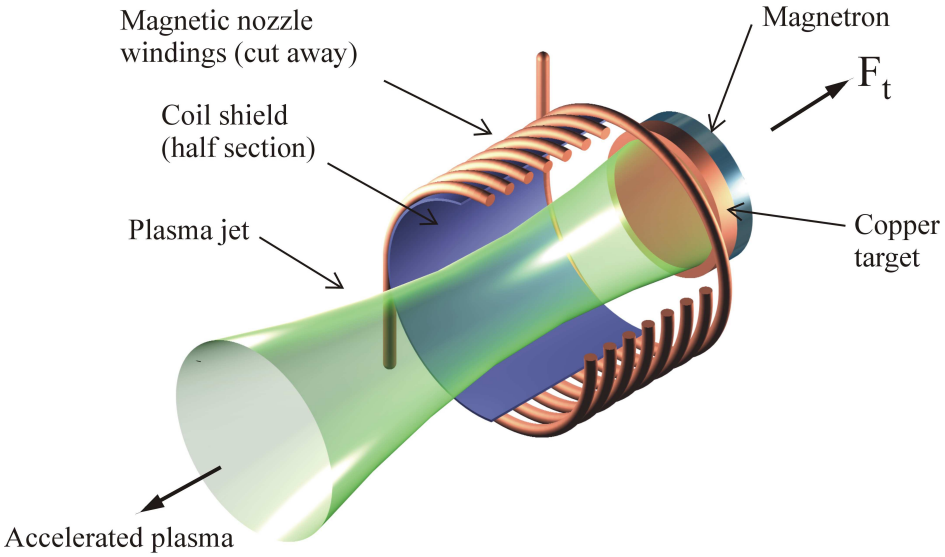

Figure 35 Schematic of the HiPIMS thruster. The magnetron source located at one end of a current-carrying solenoid produces ions and electrons that are accelerated by the diverging magnetic field. Plasma is initiated from a pulse of gas that is energized by a high intensity current pulse. Thrust F_t is produced by the acceleration in the magnetic nozzle of copper ions that are expelled from the target. The shape of the jet is an approximation derived from images of actual devices.

8.2 Methods

Copper ions were produced from a target in an AJA magnetron sputtering system using a chamber filled with argon at a constant pressure of 2.75mTorr. The copper target[2] was subjected to 200µS current pulses at 600V that were produced by a RUP-7 pulse generator at a frequency of 100Hz. The resulting ions were accelerated by the solenoid field and were detected by a simple retarding field energy analyser (RFEA) (fig. 36). The RFEA, mounted 25mm above the top of the solenoid, consisted of a 20mm diameter disc-shaped probe that was located 5mm behind a grid with a mesh aperture of approximately 50µm and mounted inside an enclosure that surrounded the probe. This type of particle energy analyser has been commonly used to measure ion energies in streams of charged particles although the physics are not completely understood [Simpson 1961 [170]].

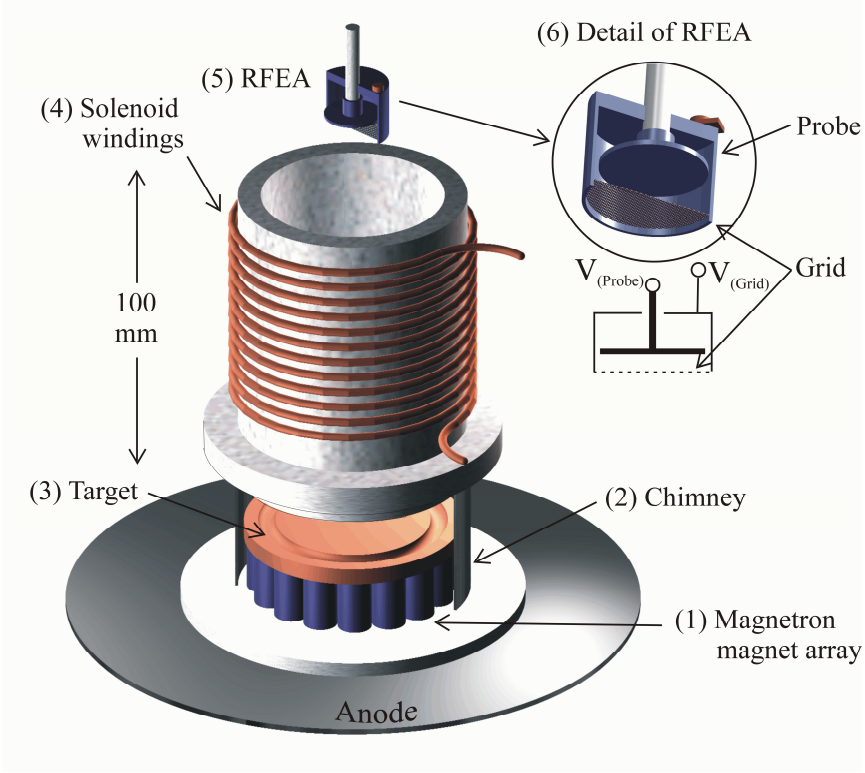

Figure 36. Schematic of the experimental apparatus showing (1) Magnetron magnet array, (2) Chimney (cut away to reveal magnetron magnets), (3) 3.00" diameter copper HiPIMS target, (4) Solenoid windings (12 turns), (5) Retarding Field Energy Analyser (RFEA), and (6) a tilted detail section of the RFEA. Target ions produced by the HiPIMS discharge were accelerated by the magnetic field of the solenoid windings and were detected by the RFEA probe. The walls of the chamber formed the anode. Ion energy was determined by varying the voltages applied to the RFEA grid and probe.

[2] Copper target, Cu, 99.999% pure, 3.00" diameter x 0.250" thick, Kurt J. Lesker Part #EJTCUXX503A4

The propellant flux was determined by measuring the deposition of metallic copper on a small silicon wafer attached to the probe inside the RFEA. During these measurements, the grid was grounded and the probe was either grounded in order to collect both neutral and ionized species or held at a voltage sufficient to repel ions. The repelling voltage of +100V was established from the measurements of current as a function of probe and grid voltages and set a lower limit for ion energy. Experimental conditions are summarised in the following table (Table 9)

Parameter	**Value**
Argon pressure	2.75mTorr
HiPIMS pulse repetition rate	100Hz
HiPIMS pulse length	200µS
RUP-7 pulse generator voltage	600V
HiPIMS peak current	6A
Target	Copper 99.999% pure, 3.00” diameter x 0.250” thick
Grid voltage	-160V
Distance of RFEA from coil	25mm

Table 9 Summary of experimental conditions.

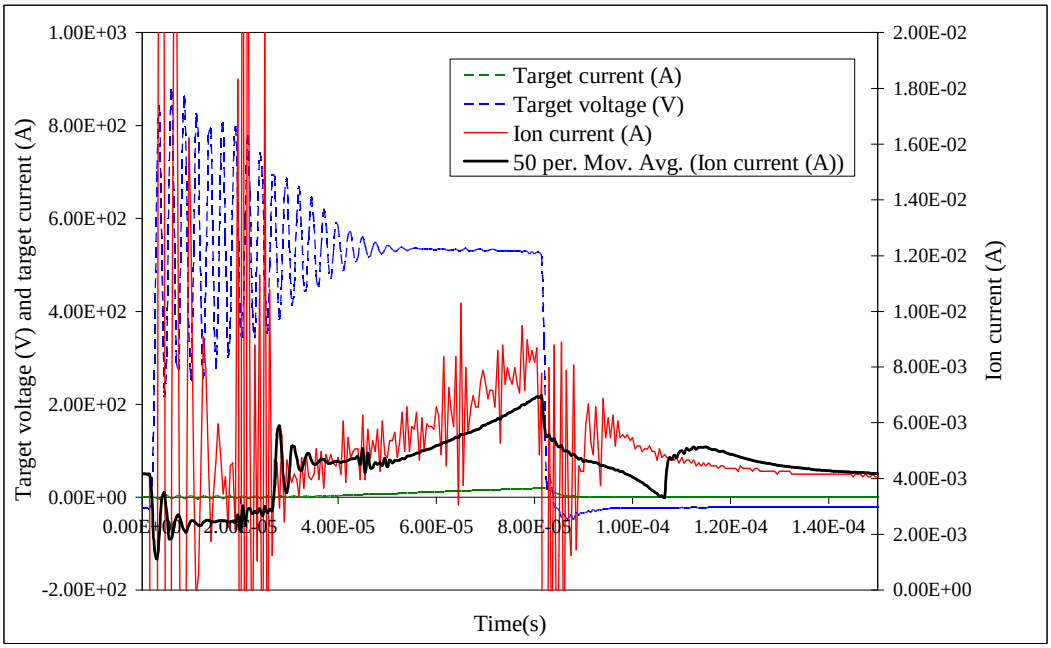

Figure 37 Experimental current and voltage waveforms measured for a copper HiPIMS discharge with RFEA grid voltage = 0V, probe voltage = -50V, coil current = 60A and a 600V pulse of 85µsec duration. The target current and target voltage are plotted on the same scale. A 50-point moving average filter was applied to the ion current data. The afterglow lasts for approximately 65uS.

8.3 Physics of a Retarding Field Energy Analyser (RFEA)

In this investigation particles with positive charge e are assumed to enter the analyser from below with kinetic energy $E = eV_0$. They are retarded by the axially directed electric field that forms between the grid and the probe plate where they are collected. If $V_{grid} = 0$ and $V_0 > V_{probe}$ then the charged particles will be collected and will appear as a current, i_{probe}. If $V_{grid} = 0$ and $V_0 < V_{probe}$, they will be repelled. Neglecting the work function of the probe (iron, 4.5eV), the total kinetic energy of the particles is $eV_{probe} = eV_0$. In the absence of a magnetic field and assuming a parallel beam, the limitation on the energy resolution of a simple RFEA such as that used in this investigation arises from the deviation of the particles from the axis of the beam by an angle θ.

The division of the momentum of the particles into axial and transverse components is described by the following relationship [Simpson 1961 [170]]:

$$\frac{transverse\ \ energy}{axial\ \ energy} = (tan\ \theta)^2 \qquad \text{Eq. 73}$$

Only the axial component of momentum overcomes the retarding potential however the divergence of particles from the axis of the beam and thus the transverse component may be reduced by applying an axial magnetic field. The effective angular aperture θ is then dependent upon the strength of the field as well as the dimensions of the physical aperture of the analyser.

When the RFEA is operated in an axial magnetic field the effect of the field is a reduction of the ion flux into the analyser through the analyser aperture. Depending on the field strength, ions with a certain momentum will be passed by the entrance aperture while ions with an axial momentum above and below that value will be rejected [Simpson 1961 [170]]. Here it is assumed that the ions of interest in this experiment – those with a high axial velocity and small radial velocity – were not obstructed by this effect.

In a RFEA a negatively biased entrance aperture separates ions from electrons by repelling the electrons. The measured energy of the resulting ion flux is reduced by (1) the retarding effect of a negative plasma potential outside the analyser and (2) by the presence of a repelling positive space charge between the entrance grid and the plate that is produced by the ions within the analyser [Grondona et al 2001[171], Rusteberg et al 1995 [172]]. Although a simple RFEA as used in this experiment does not suppress secondary electrons generated inside the RFEA, the secondary electron emission coefficient is small ($< 10^{-1}$) for ions with energies < 100eV [Grondona et al 2001 [171]] while the grid voltage (-160V) was sufficient to repel electrons accelerated by the magnetic nozzle. The probe and the grid were connected to

separate voltage sources and the probe voltage was varied in order to determine the ion current collected by the probe as a function of the probe and grid voltages.

Other investigators have shown that the voltage on the electron-repelling grid does not affect the measured ion energy [Ingram and Braithwaite 1998 [173]]. In that report the experimental apparatus consisted of a single grid RFEA that measured the ion energy in an argon plasma at the same time as the plasma potential was measured with a separate Langmuir probe. Both the maximum ion energy measured by the RFEA and the plasma space potential measured by the Langmuir probe were similar for gas pressures between 10^{-3} and 10^{-1} millibars and demonstrated that the ion energy measured with the RFEA was approximately equal to that imparted to the ions by acceleration in the plasma sheath surrounding the Langmuir probe.

The data were collected for a range of probe voltages as a function of current in the 12 turns of the solenoid that formed a magnetic nozzle (fig 36). Figure 37 shows experimental current and voltage waveforms.

8.4 Measurement errors in a simple RFEA

The limiting resolution if a simple RFEA is a function of the divergence of a particle beam as it passes through an entrance aperture of radius r_0 and is given by [Simpson 1961 [170]]:

$$\Delta E / E = \sin^2(r_0 / 4d) \qquad \text{Eq. 74}$$

In this experiment r_0 is the grid aperture (50μm) and d is the separation between the grid and the probe (0.005m). This gives a value for $\Delta E/E = 6.2 \times 10^{-6}$ which is negligible and could be discounted.

8.5 Measuring ion energy with a simple RFEA

The energy distribution of ions entering an RFEA may be determined from the probe current as a function of probe voltage for a fixed grid voltage. If the grid voltage is sufficiently negative to repel electrons then provided that the probe voltage relative to the grid is insufficiently positive to repel ions, a current will be measured (fig. 38).

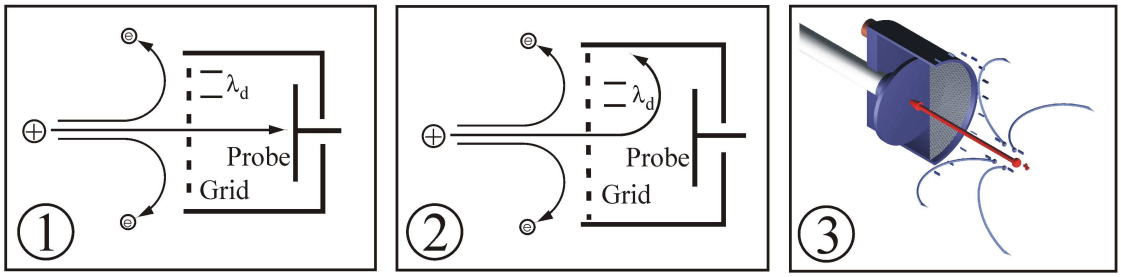

Figure 38**.** Electrons and ions in a RFEA. In frames **1** and **2**, the electrons are repelled by the negatively charged grid while ions either strike the grid wires or pass through. In **1**, the probe voltage with respect to the grid is insufficiently positive to repel ions and an ion current is detected. In **2**, the probe voltage with respect to the grid is sufficiently positive to repel ions and no current is detected. The probe – grid voltage difference where this occurs gives the ion energy. The grid wire spacing is less than or equal to the Debye length λ_d. Frame **3** shows a section through the analyser together with the paths of the electrons (curved) and ions (direct).

8.6 Physics of HiPIMS plasma sources

The high power impulse magnetron sputtering discharge (HiPIMS) is a contemporary addition to plasma sputtering techniques [Kouznetsova 1999 [162]]. High power unipolar current pulses are applied to a magnetron target with a duty cycle that keeps the time-averaged power about two orders of magnitude less than the peak power. The resulting plasma has a high density and ionization fraction that makes a HiPIMS discharge useful as an ion source for a plasma thruster (fig. 39).

Positive argon ions produced in the plasma are accelerated towards the cathode target producing a cloud of neutral and ionized metal atoms by sputtering. Magnetized secondary electrons are accelerated by the potential difference between the target and plasma and move along the magnetic field lines created by the ring of outer magnets and single inner magnet. Electrons spiral along the field lines until they collide with neutral argon atoms producing more ions. The un-magnetized ions have a Larmour radius R_L (Eq. 75) greater than the dimensions of the magnetron and so escape the magnetic field and produce a flux that can be used to produce thrust.

$$R_L = \frac{m_{ion} v_\perp}{|q|B} \qquad \text{Eq. 75}$$

Where $v_\perp$ is the velocity of the ion (with charge q and mass m_{ion}) perpendicular to the magnetic field B. In a vacuum, self-sputtering driven by copper ions sustains the process without the need for argon gas to reinitiate the copper ion flux.

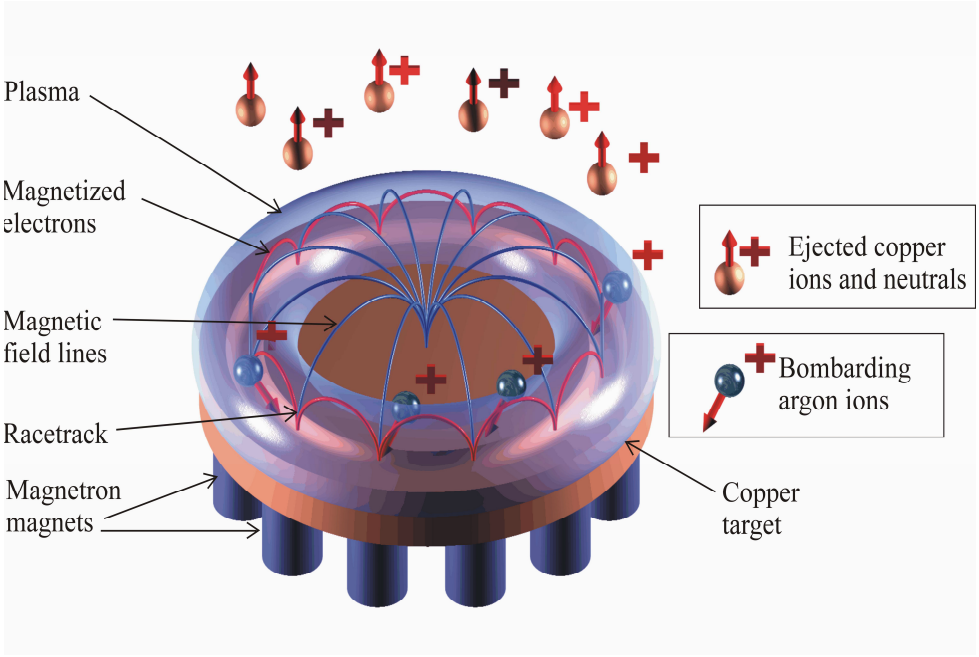

Figure 39 Schematic diagram of a HiPIMS plasma source in argon with a copper cathode target.

8.7 The magnetic field structure of the experimental apparatus.

The experimental apparatus consists of a magnetron plasma source and a solenoid located above the magnetron situated in a vacuum chamber.

The solenoid had 12 turns of 3 mm diameter copper wire mounted on a former of 104 mm diameter with a length of 100 mm. The first turn of the solenoid former was located 135 mm above the face of the magnetron magnets that were arranged in a circle in a 76.2 mm (3.00") diameter mounting. The 16 outer magnetron magnets each had a field strength of 0.2T with the north poles facing outwards while the single centre magnet had a field strength of 0.3T with the south pole facing outwards. A plot of the field lines (fig. 40) demonstrates that although the field of the solenoid had a significant effect on the magnetic field of the magnetron, it was not sufficient to disrupt the magnetron's operation. The calculated field strength at the centre of the face of the probe was 5.3 x 10-3 T and the maximum field strength inside the solenoid was 19.2 x 10-3 T.

The magnetic field lines were plotted using the Biot-Savart law to calculate the magnetic field strength arising at particular points from the current loops. A 4th order Runge-Kutta method was used to approximate the solution of the first order differential equation that describes the magnetic field.

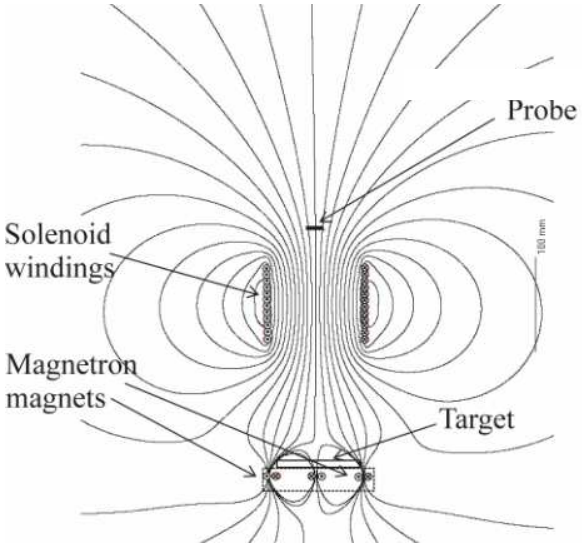

Figure 40 Experimental configuration: Magnetic field lines arising from a current of 120A in the solenoid interacting with the fields of the magnetron permanent magnets. The magnetron magnets are represented by single coils and the field lines were calculated with a 4th order Runge-Kutta iteration to determine the paths. Only the static field lines and relevant parts of the apparatus are shown.

A further plot of the field lines showed that if the solenoid field was reversed with respect to the magnetic polarity of the magnetron outer ring magnets, the magnetic field lines on the cathode surface near the racetrack region are vertical and therefore do not provide suitable conditions for electron confinement and hence magnetron sputtering. The observation that no plasma was produced during operation of the HiPIMS discharge when the solenoid field was reversed confirmed this finding.

8.8 Measuring the ionization fraction of copper

The ionization fraction of the copper reaching the RFEA was determined by measuring the thickness of the deposition of copper on a smooth silicon wafer attached by conducting tape to the probe plate mounted in the same arrangement that was used for ion current measurements. The HiPIMS plasma source and the solenoid (operating at a current of 120A) were operated for intervals of 15 minutes with the grid and probe plate grounded or with the grid grounded and the plate held at a voltage of +100V, sufficient to repel ions. The thickness of the deposited copper was measured with a profile meter and the difference between the deposits (40nm with grid and plate grounded, 6.1nm with the grid grounded and the plate held at +100V) was directly related to the ionization fraction which was determined to be 87%. This figure was a lower limit.

8.9 Results

The following figures show the results of measurements of copper ion currents produced by a HiPIMS discharge in argon. Figure 41 shows ion currents as a function of solenoid current and the voltage difference between the RFEA grid and the probe plate. Ion currents increase roughly in proportion with the solenoid current and become more stable as the solenoid current increases. The measurements were filtered with a 50 point low-pass finite impulse response filter with a cut off frequency of 50kHz and the maximum currents for each increment of voltage between the grid and the probe plate were plotted as points in Figure 41. In order to obtain a reasonable representation of the ion energy distribution, a 6th order polynomial was fitted to the plot of each ion current in order to reduce the noise in the ion current data (fig. 42). The resulting ion energy distribution function was plotted as the negative derivative of that data. The calibrated plot shows that an increasing solenoid current causes an increase in ion energy and a narrowing of the energy distribution (fig. 43) although non-linearities in the RFEA mean that the values determined for the ion energy are approximate rather than exact.

Note that the plate stopping potentials for all coil currents are less negative than the potential on the grid but still below ground potential. This is interpreted as indicating that the grid potential is not maintained across the openings in the grid. This effect was observed previously and it occurs when the grid wire spacing is greater than the Debye length of the plasma [Bilek et al 1996 [174]]. For plasma electron densities typical of HiPIMS the Debye length is less than distance between the grid wires in this experiment (50 μm) [Bohlmark 2006 [175]].

The ion energy distribution that was found when the coil current was zero was calibrated using measurements of ion currents from a HiPIMS source that were made under similar conditions [Vlcek 2007 [176]]. In that experiment, the ion energy distribution of the copper ions was determined from 350 individual values of ion energy that were measured with an energy-resolved mass spectrometer (EQP 300 Hiden Analytical). That data was digitized and those values were incorporated as a smoothed curve aligned with the measurements for the ion energy distribution made in the absence of a magnetic field.

Assuming reasonable linearity, the calibration was used to determine the approximate ion energy distributions arising from higher coil currents as shown in figure 43. Given that solenoid coil currents are known to lower the plasma potential, it is expected that the ion energy measurements are increasingly underestimated as the coil current increases, hence the values shown in the Figure are to be regarded as lower limits for the ion energies at non-zero coil currents [Bilek et al 1996 [177]].

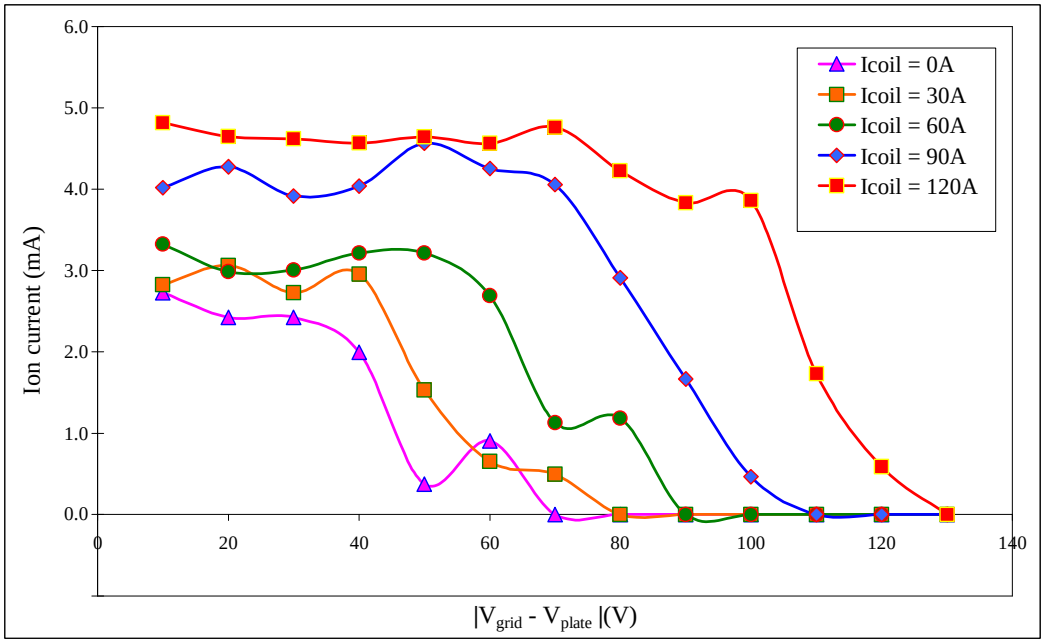

Figure 41 Copper ion currents from a magnetron copper target as a function of solenoid current and the voltage difference between the grid and the probe plate. The grid voltage was set at -160V. The ion current falls to zero when the plate potential with respect to the grid is sufficient to repel all the ions. The ion current as measured by the RFEA increases with the solenoid current showing that an increasing solenoidal magnetic field strength produces a larger ion current. 2500 samples per point were taken and smoothed with a 50-step finite impulse response filter.

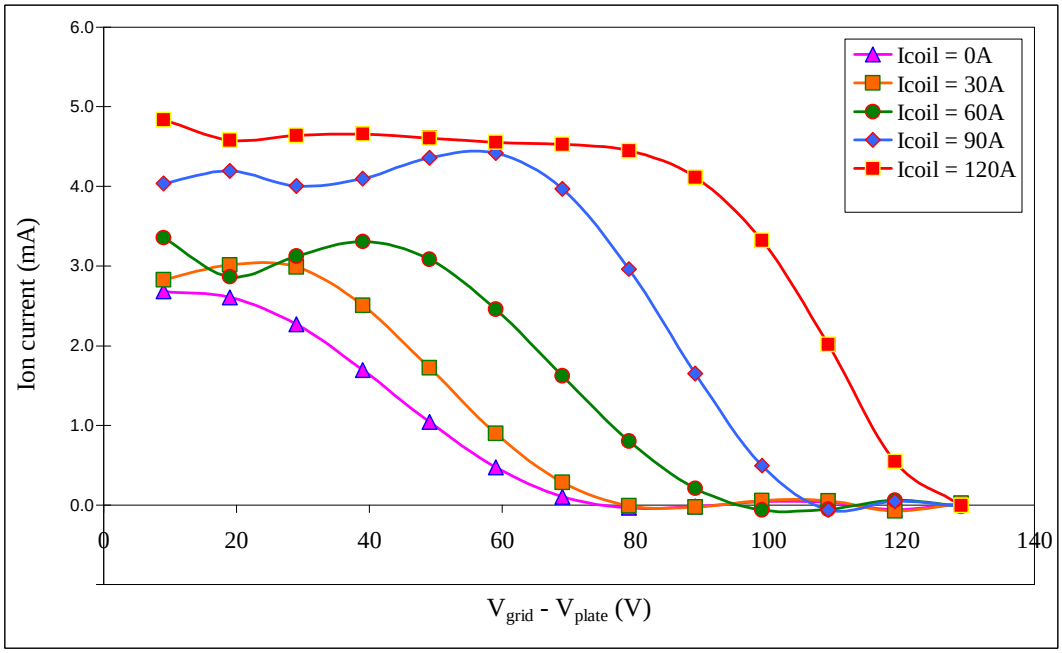

Figure 42 Copper ion currents from a magnetron copper target as a function of solenoid current and the voltage difference between the grid and the probe plate. A 6th order polynomial was fitted to the raw data shown in fig. 5 in order to make the results of the calculation of the derivatives less sensitive to irregularities in the measurements.

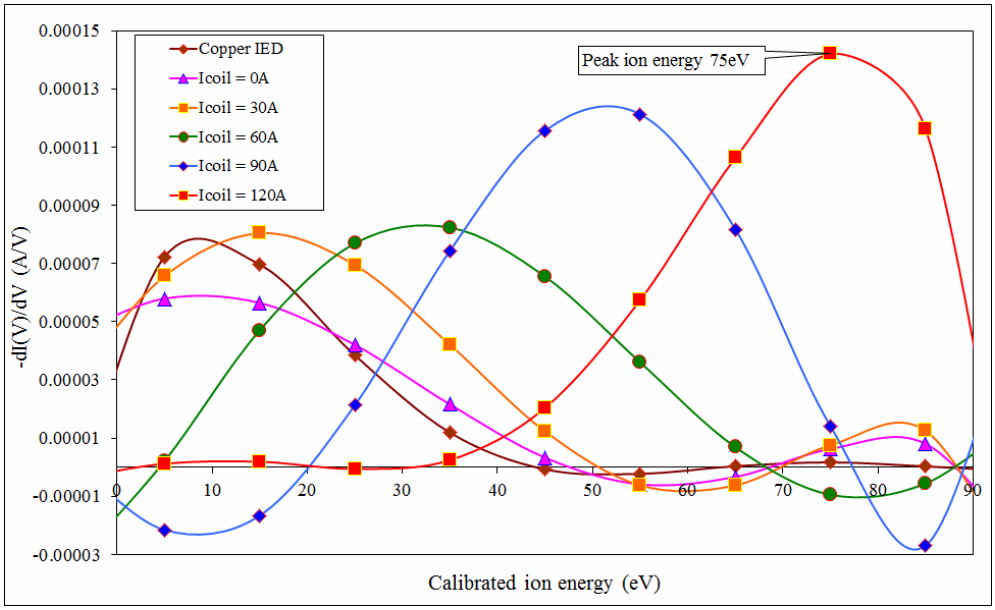

Figure 43 Calibrated copper ion energy distributions as a function of solenoid current and the voltage difference between the grid and the probe plate. The distribution function is the negative derivative of the ion currents shown in fig. 6. The width of the distribution functions is reduced and the height increased with larger solenoid currents demonstrating that the increasing solenoid magnetic field strength increases the directed energy of the ions and reduces the spread of their energies. The ion energy distributions are calibrated against a known ion energy distribution for copper (copper IED) obtained under similar conditions and in the absence of a magnetic field **[**Vlcek 2007 **[176]].**

The peak of the ion energy distribution for a coil current of 120A is 75 eV, corresponding to an ion velocity of 19.8km/s and a specific impulse of 2017s. A solenoid current of 120A, corresponding to a maximum field strength inside the solenoid of 19.2 x 10^{-3} T, increased the height of the ion energy distribution function by approximately 2.3 times compared to a solenoid field strength of zero.

8.10 Analysis

Maxwell-Boltzmann ion energy distribution curves were calculated for ions with energies similar to those measured in the experiments (fig. 44). An offset was added to each curve to account for the acceleration imparted to the ions by the magnetic nozzle with the result that the plotted curves closely resembled those calculated from the RFEA measurements (fig. 43). This outcome demonstrated that ions with a smaller energy distribution corresponding to lower ion temperatures were travelling at higher velocities. Further, it showed that the effect of the magnetic nozzle is analogous to that of a chemical rocket where the nozzle converts the thermal energy of the propellant into a gas with directed kinetic energy at a lower temperature.

The inset in figure 44 illustrates the decline in ion temperature with increasing velocity and shows that the ion flux is accelerated adiabatically by the magnetic nozzle.

Hecimovic et al 2008 [178], have demonstrated that the energy distribution of ions produced by a HiPIMS discharge is the sum of two Maxwell-Boltzmann distributions, one generated during the discharge that produces a high energy tail and another produced in the afterglow that contributes to the main peak. In contrast, the measurements reported here show that the effect of a magnetic nozzle produces ions with a single peak that has an energy principally determined by the acceleration produced by the magnetic nozzle. As the nozzle field increases, the ion energy distribution narrows while the ion velocity increases with the field strength. Equipment constraints limited the nozzle currents in this investigation to 120A. These results suggest that much larger nozzle currents may significantly increase the attainable ion velocity and hence the specific impulse.

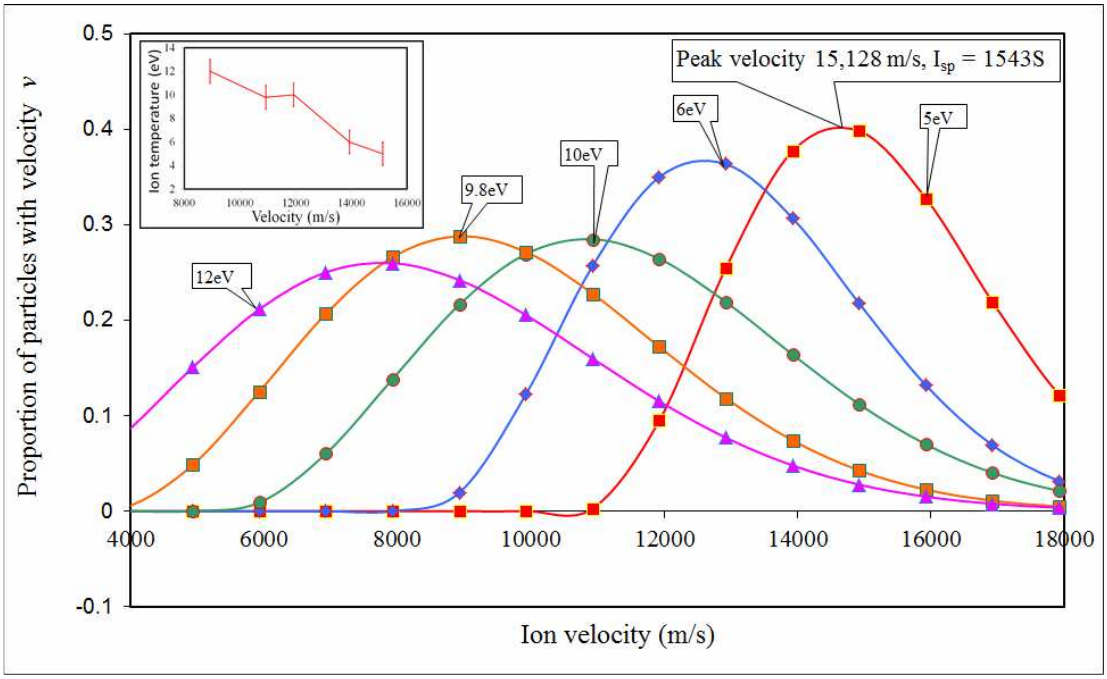

Figure 44 Maxwell-Boltzmann ion energy distribution curves with velocity offsets to account for the acceleration of the ions in the magnetic nozzle. The curves show that the ions with the greatest velocity have curves equivalent to the lowest energy ions and demonstrate that the thermal energy of the ions have been converted to directed kinetic energy through the effect of the magnetic nozzle in a mechanism analogous to de Laval nozzles used in chemical rockets. The labels on each curve indicate the temperature of each distribution in eV. The inset shows the decline of ion temperature in eV with velocity as the plasma expands through the magnetic nozzle. The error bars in the inset show the standard error.

8.11 Discussion

These measurements have demonstrated that a solenoidal magnetic field that has its axis normal to the centre of a cylindrical HiPIMS target increases the magnitude and the velocity of the flux of ions and neutrals produced by the HiPIMS discharge along that axis. The measurements demonstrate that the flux is proportional to the solenoid current. The following table (Table 10) summarizes the principal findings. The thrust will have been underestimated since the solenoid current reduces the plasma potential and this effect was not taken into account.

Measured or calculated performance parameters (Icoil = 120A)	**Value**
Ionization fraction (lower limit)	87%
Exhaust velocity v_e (measured)	15.1km/s
Thrust efficiency η_t (calculated)	6%
Specific impulse I_{sp}	1543s
Total thrust F_t (calculated)	3.77×10^{-6}N

Table 10 Measured, calculated and estimated values of the performance parameters of a HiPIMS thruster. Ionization fraction and exhaust velocity were measured with a retarding field energy analyser and specific impulse was calculated from the exhaust velocity. The thrust was estimated from the measured rate of deposition of copper (neutrals and ions) over an area of 0.005m^2 that corresponded to the aperture of the solenoid former with the assumption that the flux of copper was uniform over that area.

These findings demonstrate that a HiPIMS copper plasma source coupled with a magnetic nozzle forms a useful solid-fuel plasma thruster that could find application in various missions including satellite position keeping as well as orbital manoeuvres and interplanetary probes. The fact that copper self-sputters in a vacuum potentially reduces the complexity of the thruster that is driven by a pulsed current source together with a means of triggering the initial discharge, either a small gas supply or a laser. Unlike gridded ion thrusters, there appears to be no fundamental limit to the size and thrust of these devices.

The HiPIMS thruster has a specific impulse (I_{sp} = 1543s), comparable to already deployed Hall thrusters (Isp ≅ 2000s) [Hofer 2010 [179]] and does not exhibit the disruptive instability that can affect those thrusters [McDonald and Gallimore 2011 [180]]. In particular, spoke instability in cylindrical Hall thrusters has been linked to cross B-field currents and a drastic reduction in thruster efficiency associated with large increases in back-streaming electron currents [Parker

et al 2010 [181]. So far, the physics of those instabilities is not fully understood [Kapulkin and Behar 2013 [182]. Similar instabilities can occur in HiPIMS discharges as cross B-field currents and appear as rotating spokes or ionization zones above the target [Hecimovic 2016 [183]] although no instability was observed in the experiments reported in this paper. The electric field of the potential hump associated with the spokes displaces ions in all directions although unlike Hall thrusters, that instability is not sufficient to disrupt the operation of the HiPIMS thruster since the acceleration of the ions does not depend upon the axial electric field produced by magnetized electrons retarded by the radial magnetic field.

The collimation and intensity of the plasma beam containing copper ions produced by the HiPIMS source in conjunction with a magnetic nozzle suggests that it could find application in the semiconductor industry where copper metallization is used for interconnects in integrated circuits where its high conductivity significantly increases the performance of those devices [Havemann and Hutchby 2001 [184]].

These results suggest that larger solenoid magnetic fields beyond the capacity of the present solenoid current pulse generator used in these experiments may result in an ion energy distribution function with a greater mean ion velocity and a resulting higher I_{sp}.

8.12 Conclusions

This investigation has demonstrated that a HiPIMS source can be used to produce ions from a solid target that could be used as propellant in an electrodeless thruster. It has shown that adding a magnetic nozzle to a HiPIMS plasma source greatly increases the directed ion energy by converting random thermal energy in the plasma to kinetic energy in the jet. A simple retarding field energy analyser has been able to show that that the width and therefore temperature of the ion energy distribution decreases as the directed velocity increases.

As well as applications in space technology, this device could be useful in thin film deposition and ion implantation where a directed beam with a narrow energy range is useful.

9 A thruster using magnetic reconnection to create a high-speed plasma jet

A report on the development of a plasma thruster that uses magnetic reconnection in a plasma to produce a high velocity jet of charged particles.

9.1 Introduction.

Magnetic reconnection (Priest and Forbes, 2000 [185], 2000, Biskamp, 2000 [186]) is a topological rearrangement of field lines that produces a lower energy configuration by the acceleration and heating of charged particles in highly conductive plasma that contains embedded magnetic fields (Yamada, Kulsrud, and Ji 2010 [187]). Reconnection is probably the best explanation for large scale, dynamic releases of magnetic energy in celestial objects and magnetic reconnection is the most likely driving mechanism of solar flares that produce high-energy plasma jets in the solar atmosphere (Yamada, Kulsrud, and Ji 2010 [187]). As field lines break and reconnect in the solar atmosphere, magnetic energy is converted into random thermal and directed kinetic energy of a plasma of protons and electrons that can be expelled at speeds of 300km s^{-1} from a current sheet that forms between magnetic domains (Sui and Holman 2003 [188]). Magnetic reconnection is observed in the boundary between the Earth's magnetic field and the magnetized plasma of the solar wind and produces an accelerated plasma that moves Earthwards that can cause aurora (Angelopoulos et al, 2008 [189]). Magnetic reconnection also appears to be responsible for saw-tooth instabilities in Tokamak fusion reactors that cause the plasma to escape from the confinement field. Magnetic reconnection is an active field of research in astrophysics and geophysics. However as far as it is possible to determine, there are no reports of reconnection as a possible mechanism for the production of high speed plasma jets in thrusters for spacecraft.

Magnetic reconnection was first put forward as the mechanism for the acceleration of particles in solar flares by Ronald Giovanelli (Giovanelli 1946 [190]). Electric fields induced by changing magnetic fields had been proposed as an accelerating mechanism in solar flares. However the difficulty with that proposal is that charged particles subject to effects such as betatron acceleration are often naturally confined by magnetic fields. Giovanelli suggested that, instead, acceleration occurs near magnetic nulls or neutral points where opposing magnetic fields cancel (fig. 45).

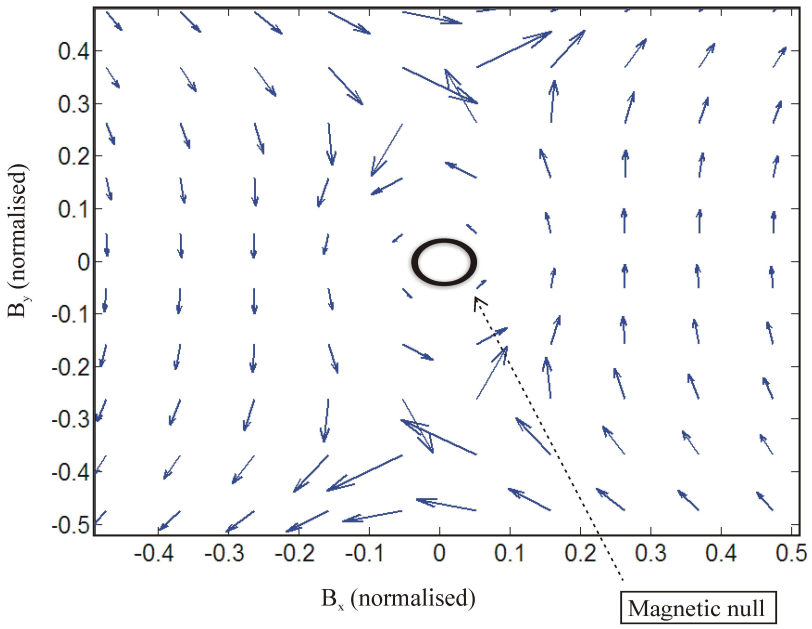

Figure 45 A 2-D Matlab plot of the vector sum of normalized magnetic field components B_x and B_y of opposing magnetic fields showing cancellation of the fields at a null or neutral point marked by **O**.

Following Giovanelli's work, a magneto-hydro-dynamic (MHD) theory of reconnection at magnetic neutral points was developed that had plasma and magnetic flux flowing into regions where the oppositely directed flux components are destroyed and the energy in the magnetic field is converted into that of heated high velocity particles (Dungey 1953 [191]).

Dungey, a student of Sir Fred Hoyle, was the first to suggest that "lines of force can be broken and re-joined".

By 1958 Sweet and Parker had introduced the idea that reconnection can occur in a current sheet whose half thickness l is much less that the global scale length L_e (fig. 46). In that model the breaking and reconnection of field lines occurs only within the current sheet where inertia is important and the out-flowing plasma is accelerated to speeds comparable to the Alfven speed[3] (Sweet, 1958 [192], Parker, 1957 [193]). The effect of reconnection is to convert the magnetic energy of the inflowing plasma into a rough equi-partition between the kinetic and thermal energies of the accelerated particles (Priest and Forbes, 2000 [185]).

[3] The Alfven speed $v_A = \frac{B}{\sqrt{\mu_0 \rho}}$ is the velocity of MHD waves that occur in magnetized plasma; B is the field strength and ρ is the plasma density.

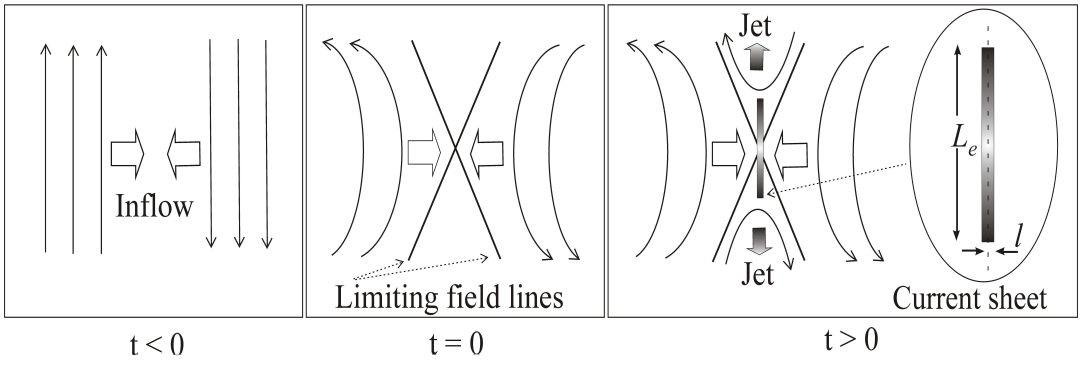

Figure 46 The Sweet-Parker model of reconnection proposes that collisions between two separate magnetic domains in plasma produce plasma jets by reconnection of magnetic field lines in a current sheet or diffusion region that forms between the domains. At t < 0 inflowing plasma with embedded magnetic flux initiates the process. At t = 0 an X-type magnetic null is produced by the interaction of opposing magnetic field lines. The limiting field lines are known as separatrices and form an "X" from which the term "X" type null point is derived (Priest and Forbes 2000 [185]). At t > 0 a current sheet forms, jets of heated plasma are ejected from the current sheet, lines of force are broken and rejoined in the current sheet and four separate magnetic domains are created.

The evolution of the magnetic field in a resistive-MHD plasma is governed by the following magnetic induction equation which, derived from Faraday's Law, together with the generalised Ohm's law and Ampere's Law, describes the motion of magnetic field lines in an MHD plasma with uniform conductivity σ_0 (Priest and Forbes, 2000 [185]):

$$\frac{\partial \mathbf{B}}{\partial t} = \nabla \times (\mathbf{v} \times \mathbf{B}) + \frac{1}{\mu_0 \sigma_0} \nabla^2 \mathbf{B} \quad , \qquad \text{Eq. 76}$$

where $\mathbf{B}$ is the magnetic field, $\mathbf{v}$ is the bulk flow velocity, and μ_0 is the magnetic permeability of free space.

This basic MHD equation states that the magnetic field changes are the sum of the effects of the transport of the plasma (the first term on the right hand side) and of the diffusion of the magnetic field through the plasma (the second term on the right hand side). If the conductivity σ_0 is high then the magnetic field is frozen into the plasma and the field lines move with the plasma. This result shows that electrically conductive plasma is a prerequisite for reconnection.

If V_0 and L_0 are typical velocity and length scales respectively, then the ratio of the first to the second terms on the right hand side of equation 1 is the dimensionless magnetic Reynolds number R_m, defined as the ratio of convection to diffusion:

$$R_m = \frac{L_0 V_0}{\eta} \quad , \qquad \text{Eq. 77}$$

where $\eta = \frac{1}{\mu_0 \sigma_0}$ is the magnetic diffusivity, μ_0 is the permittivity of free space and σ_0 is the plasma conductivity.

Reconnection occurs in magnetized plasma when $R_m >> 1$ (Priest 2004 [194]) so that the induction equation (equation 1) reduces to:

$$\frac{\partial \mathbf{B}}{\partial t} = \nabla \times (\mathbf{v} \times \mathbf{B}) \qquad \text{Eq. 78}$$

When the plasma velocity is large and equal to the Alfven velocity, then $V_0 = v_A$ and the magnetic Reynolds number is called the Lundquist number S, the ratio of the length scale L_o with the Alfven time to the magnetic diffusion time η:

$$S = \frac{L_0 v_A}{\eta} \qquad \text{Eq. 79}$$

Table 11 summarizes the conditions under which reconnection can occur.

Parameter	**Condition**	**Reference**
Magnetic Reynolds number	>>1	Priest 2004 [194]
Collisions	Reconnection rate increases in collisionless plasma	Yamada 2007 [195]
Conductive plasma	Field lines are frozen in to the plasma	Priest and Forbes, 2000 [185]
Lundquist number $\geq 10^3$	Large values of the Lundquist number indicate highly conductive plasma.	Yamada et al 1997 [196]
Ion gyroradius < plasma scale length	Allows true MHD flows to develop	Yamada et al 1997 [196]
Magnetic and electric fields	Large magnetic field gradients and electric fields.	Priest 1990 [197]

Table 11 Summary of conditions under which reconnection may occur

The scale of the experiments discussed here is smaller than the ion inertial length and therefore not in the MHD regime where processes can be described by fluid equations. That means that the Lundquist number is not relevant and processes taking place in the diffusion region must occur in the kinetic or whistler regime. Magnetic reconnection with resulting kinetic Alfven waves is probably occurring in the regions between the thruster tubes.

Table 12 shows the range of values for various parameters of magnetised plasmas in astrophysical objects and in laboratories where magnetic reconnection is either likely to occur or is known to occur.

In particular, the 420s timescale for reconnection in the Earth's magnetosphere was observed by the International Sun-Earth Explorer-1 satellite that detected flux transfer events (Russell C. T. et al, 1997 [198]). In that paper the authors state that flux transfer events (FTEs) "are clearly due to reconnection" in the magnetopause and that the flux transfer events do "not occur unless the magnetic field at the magnetopause has been southward for the order of 7 minutes [420s] or more and that this time scale is controlled by the magnetopause or the magnetosphere." The conclusion drawn is that "FTEs occur in a quasi-periodic manner under steady solar wind conditions" and that "discovering the reason for this apparent time scale for reconnection at the magnetopause is important and may provide clues as to why at times the magnetopause reconnects in a quasi-steady manner and at other times reconnects in a quasi-periodic manner".

In general, the greater the length scale then the longer the time scale so that while reconnection may take many minutes in the solar atmosphere and in the interface between the Earth's magnetosphere and the magnetic field entrained in the solar wind, reconnection is observed to occur in hundreds of microseconds in laboratory apparatus (fig.47).

Location	**Lundquist number S**	**Particle density (per m^3)**	**Temperature**	**Energy of particles**	**Global scale**	**Magnetic field strength (G)**	**Reconnection time scale**
Solar atmosphere	$>10^{10}$ Yamada et al 1997 [196]	10^{15} - 10^{16} Hansteen et al 1997 [199]	~2eV - ~1700eV Erdelyi and Ballai 2007 [200]	Ions: 1 x 10^9eV Electrons: 1x10^8eV Yamada et al 2010 [201]	10^8 m Priest and Forbes, 2000 [202]	2 x 10^3 Yamada et al 2010 [201]	2x 10^2 – 2 x 10^3 s Yamada 1999[203]
Earth's magnetosphere	0.1 – 10 Cattell 1996 [204]	7 x 10^6 Russell, 2000 [205]	0.1eV (ionosphere) - 1 x 10^3 eV (outer magnetosphere) Burch 1999 [206]	1eV – 3 x 10^5 eV Young, 1986 [207]	10^7 m Priest and Forbes, 2000 [202]	3 x 10^{-4} At 10 R_e Russell 2000 [205]	420s Russell, 1997 [198]
Tokamak (JET) Priest and Forbes 2000 [202]	$>10^7$ Yamada et al 2010 [201]	10^{20}	10^8 (K)	700keV Chen et al 1988 [208]	1 m	2 x 10^4	1 x10^{-4} s
LPD Stenzel and Gekelman 1984 [209]	1 - 10	10^{18}	T_e=10eV	……..	2 m	20	1 x10^{-4} s
MRX Yamada et al 1999 [203]	10^2 - 10^3	0.1 – 2 x 10^{20}	T_e=10eV- 30eV	Electrons: 15eV	1 m	300 - 600	1 x10^{-4} s
SSX Brown et al 2002 [210]	≤1 x 10^3	5 x 10^{19}	T_i = 20eV	50eV	0.1m	500	32 – 64 x 10^{-6}s

Table 12 Conditions where magnetic reconnection is likely to occur. Magnetic reconnection occurs in magnetized plasma in large-scale astrophysical objects such as the solar atmosphere and the Earth's magnetosphere where it interacts with the magnetized solar wind as well as in laboratory scale apparatus. Ideal MHD physics is applicable when the Lundquist number S >> 1. Abbreviations: JET = Joint European Torus, LPD = Linear Plasma Device, MRX = Magnetic Reconnection Experiment, SSX = Swarthmore Spheromak Experiment.

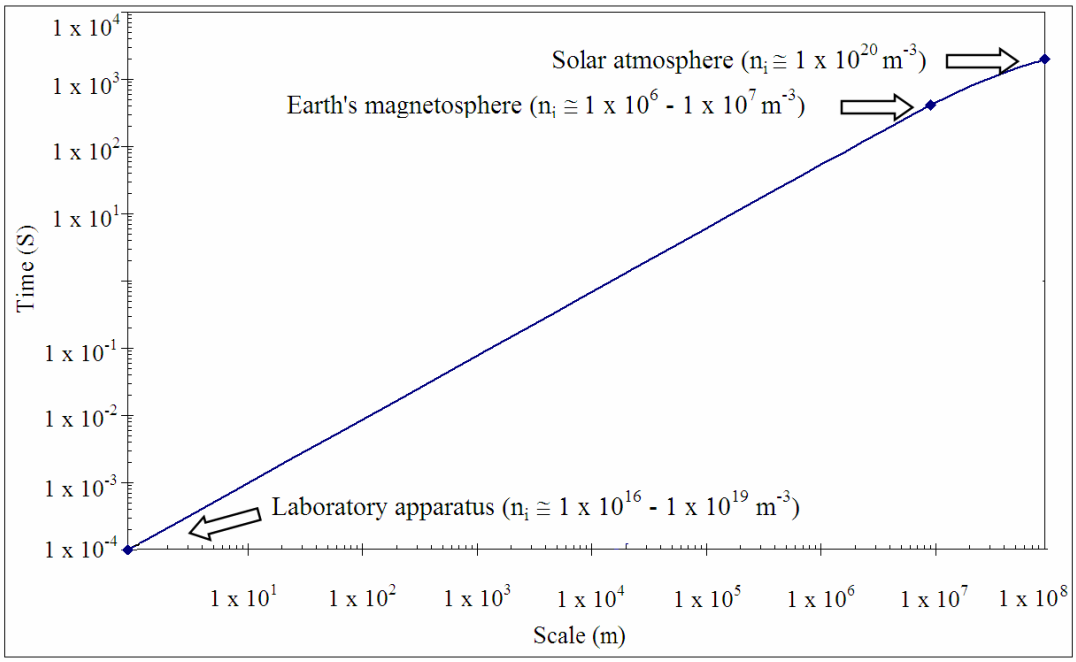

Figure 47 Reconnection time as a function of length scale.

Early simulations of reconnection were 2-D (Sonnerup 1970 [211]) although more recent work has focused on 3-D simulations (Daughton et al 2011 [212]). In both cases it has been found that reconnection in 2-D and 3-D models produces fast outflow jets from the reconnection site and reconnection occurs in current sheets where dissipation transforms magnetic energy into heat and the kinetic energy of the jets (Drake 2005 [213]) .

The dimensions of the experimental device (35 mm gap between tubes) were smaller than the ion gyro-radius (0.09 m for 4eV ions) and the ion inertial length (d_i = 0.67m for n_i = 4.5 x 10^{18}/m^3) although much larger than the electron inertial length (d_e = 2.5mm). It is probable that the processes occurring in the space between the current-carrying tubes are likely to be occurring in the Hall/whistler regime that is assumed to be responsible for the acceleration of electrons by cyclotron resonance.

Reconnection appears to be initiated by the disturbance of an anisotropic bi-Maxwellian population of electrons with $T_{\perp e} / T_{||e} > 1$ in the diffusion region that through a process such as Wiebel instability, converts the energy in the magnetic field into waves that couple with and drive the thermal and kinetic energy of the electrons. If the electron plasma temperature ω_{pe} is greater than the electron cyclotron frequency $|\Omega_e|$ and the electrons are sufficiently hot, the whistler mode has the lowest anisotropy threshold and has a maximum growth rate parallel to the background magnetic field $\mathbf{B}_0$ (Gary and Cairns 1999 [214]).

Since whistlers are dispersive ($\omega \sim k^2$), the waves driving the outflow are faster at smaller scales (Mandt et al 1994 [215]). Evidence from the Cluster satellite observations (Wei et al 2013

[216]) suggests that in the absence of a magnetic field magnetic reconnection is driven by whistlers produced by electron cyclotron resonance while laboratory experiments show that large-amplitude electromagnetic waves which have similar properties to kinetic Alfven waves are produced when a magnetic guide field is present (Inomoto et al 2013 [217]). Other Cluster satellite observations show the presence of a super-Alfvénic electron outflow jet at least 60 ion skin depths downstream from the X-line (Phan et al 2007 [218]).

Simulations of large-scale reconnection in the heliosphere show that reconnection is limited to regions where those where the interstellar magnetic field lies nearly anti-parallel to the heliospheric field (Swisdak et al 2010 [219]). This finding suggests that the anti-parallel fields that arise within the annulus of the thruster created conditions that facilitate reconnection.

Although understanding has greatly increased since Giovanelli's work (Giovanelli 1946 [190]), four key issues remain (Zweibel and Yamada, 2016 [220]).

1. The rate at which reconnection develops. Observations of phenomena such as solar flares show that the processes occur much more rapidly than predicted by theory.
2. The triggering of reconnection following the accumulation of magnetic energy is not well understood.
3. The mechanism that leads to the apportioning of magnetic energy between the jets and the heating of the plasma is still to be resolved.
4. The integration between the large scale MHD processes and the small scale kinetic interactions in which reconnection occurs has to be established on firm theoretical grounds.

In the experiments reported here, $\omega_{pe} = 1.91 \times 10^{10} Hz$ and $\Omega_e = 2.80 \times 10^{8} Hz$ so that $\omega_{pe} > \Omega_e$ and whistlers are likely to be driving the energetic electrons that were detected.

Evidence from the Cluster satellite observations (Wei et al 2013 [221]) suggests that in the absence of a magnetic field magnetic reconnection is driven by whistlers produced by electron cyclotron resonance while laboratory experiments show that large-amplitude electromagnetic waves which have similar properties to kinetic Alfven waves are produced when a magnetic guide field is present (Inomoto et al 2013 [222]).

A simulation of whistler wave mediated reconnection shows that the development of a component of the magnetic field out of the plane of the current sheet is an observable signature of whistler driven reconnection. (Mandt et al [215]).

9.2 Magnetic reconnection experiments in the laboratory

Magnetic reconnection has been the subject of laboratory investigations for some time with the aim of the investigation being the elucidation of the physics of the phenomena near magnetic null points with a focus on the vicinity of the neutral sheet.

In earlier experiments (Stenzel and Gekelman 1984 [209] 1985 [223] 1990 [224]]) a neutral sheet was created by applying a pulsed magnetic field that produced an X-type null point within a plasma that had been formed in gases (Ar, He, H) at low pressure (1 x 10^{-4}Torr) in a discharge in a large (1.5m diameter, 2.0m length) experimental chamber (fig. 48). The reconnecting magnetic fields were produced by pulsing 10kA currents with a rise time of 100μs through insulated parallel plate electrodes that were separated by a gap of 320mm. In those experiments the formation of current sheets were observed and the reconnection of field lines and the acceleration of particles was established from three dimensional time resolved field and flow measurements. The dimensions of the device were less than the ion inertial length although much larger than the electron inertial length so that the processes occurring in the space between the current-carrying plates in the presence of a guide field were likely to have produced kinetic Alfven waves that accelerated the plasma.

In those experiments the formation of current sheets were observed and the reconnection of field lines and the acceleration of particles was established from three dimensional time resolved field and flow measurements. The experiments reported here were similar in that the dimensions (0.15m) were smaller than the ion inertial length (estimated to be 0.67m in Ar with a magnetic field of 0.2T and a particle density of 4.5 x 1018/m3) although three dimensional measurements were not performed.

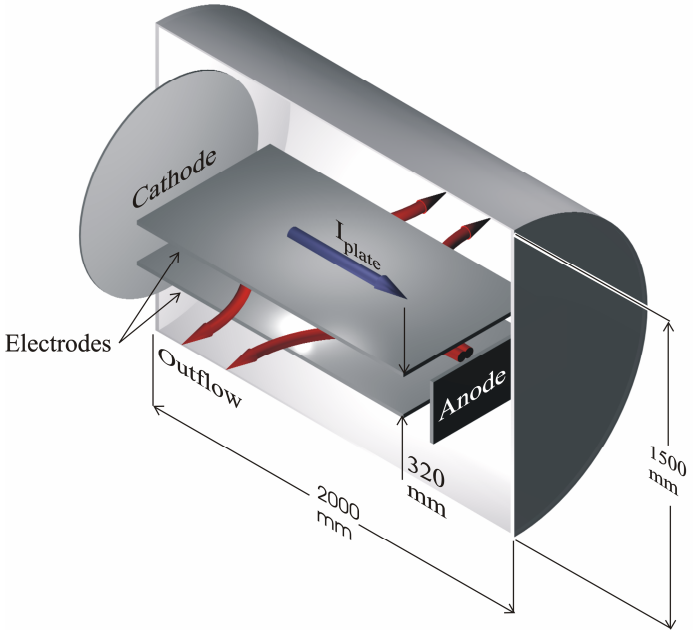

Figure 48 Magnetic reconnection was observed in experiments that were conducted in a chamber at low pressures (1 x 10^{-4} Torr) where large currents (10kA) were passed through electrodes embedded in plasma created by a discharge in Ar, He and H_2. The purpose of the experiments was to examine the physics of reconnection under controlled laboratory conditions and was not designed as part of the development of a plasma thruster. (After Stenzel et al 1985 fig.1 [223])

More recently, an experiment with a similar geometry has been designed to investigate driven magnetic reconnection in collisional and near collisionless regimes for the purpose of studying: (1) fluctuations associated with reconnection, (2) the effects of boundary conditions, (3) three dimensional reconnection and (4) the influence of a guide field (Bohlin et al 2014 [225]). Plasmas with densities ranging from n_e = 1 x 10^{16} to 1 x 10^{19} m^{-3} with T_e < 6eV were created by RF energy radiating from either a helicon antenna or a spiral antenna in a chamber 1.5 meters in length that had a strong axial guide field (B ≤ 100mT) produced by external windings. Two parallel conductors 100mm wide that carried a current of 1kA were each located 150mm from the axis of the chamber and drove reconnection by compressing the axial magnetic field towards the central axis on a time scale of 10μs.

Magnetic reconnection experiments carried out in Princeton and Tokyo (Yamada et al 1990[226]) were similarly designed to elucidate the physics of the phenomena rather than to develop a thruster and used the collision between magnetized toroidal plasmas as a means of inducing reconnection. In those experiments two annular plasmas with identical poloidal fields and toroidal currents were formed around flux cores and the reconnection forces were determined by the rate at which the toroidal current was induced into the annular plasma that caused the plasmas to expand until they collided (Yamada et al 1997 [227]) (fig. 49).

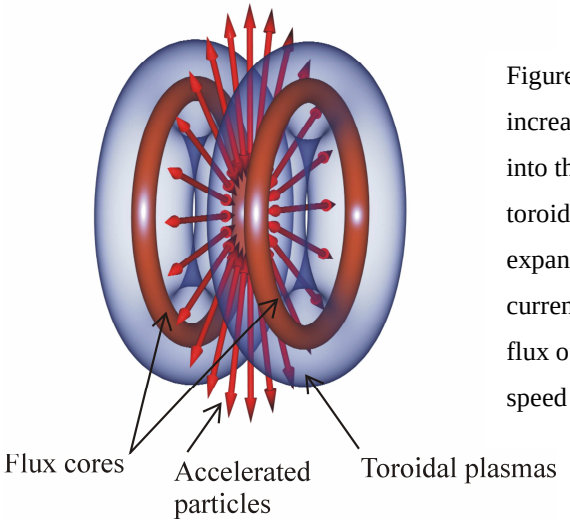

Figure 49 Colliding toroidal plasmas produced by increasing the rate of induction of toroidal current into the annular plasmas that are formed around toroidal flux cores. Reconnection occurs as the expanding plasmas collide and merge that causes a current sheet to form, field lines to reconnect and a flux of particles to be accelerated to the Alfven speed by the associated electric field.

Other investigations that investigated the triggering of magnetic reconnection used an arrangement of toroidal coils to produce an X-type geometry in plasma in the strong guide field regime (Katz et al 2010 [228]).

None of these previously reported magnetic reconnection experiments have been directed towards creating high speed plasma jets that could be used in thrusters for spacecraft, the aim of this work.

9.3 Methods

An experimental apparatus consisting of concentric copper tubes connected electrically in parallel and mounted inside a low-pressure chamber containing argon plasma was constructed. The tubes were 120 mm long with the 6mm thick inner tube having an outer diameter of 60 mm and the 3mm thick outer tube having an outer diameter of 150 mm.
Current pulses of up to 2000 amps with a duration of approximately one millisecond were fed into the tubes from a capacitor bank and the effect of the resulting magnetic field on the plasma was measured with a 20mm diameter disk shaped Langmuir probe and with a single grid retarding field energy analyzer (RFEA) that used the same probe (figs. 50 & 51).

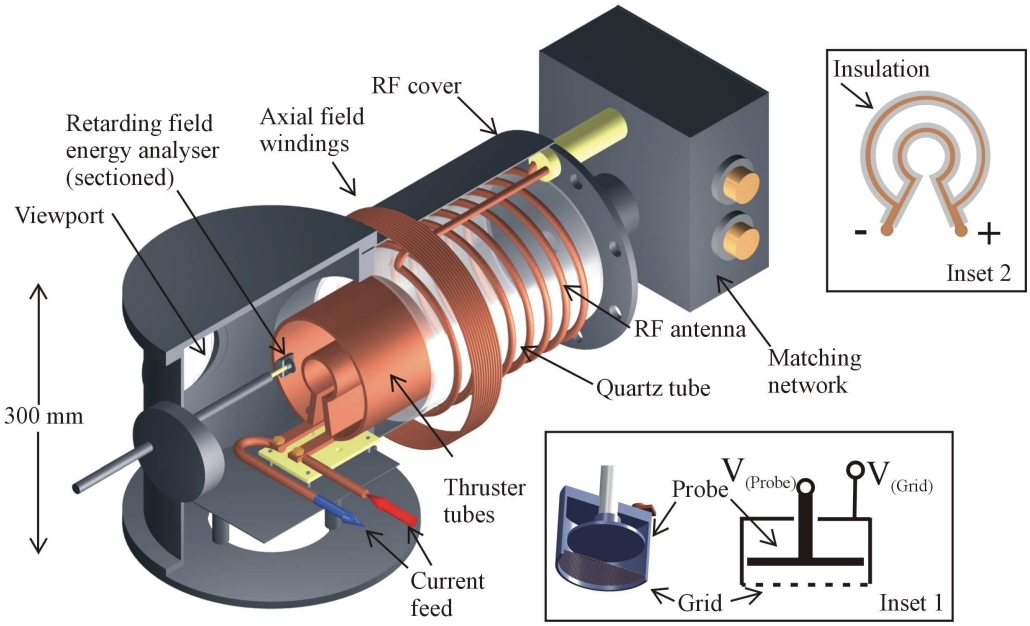

Figure 50 Sectioned schematic of the magnetic reconnection experimental apparatus showing the installation of the concentric thruster tubes inside a vacuum chamber. The thruster tubes were usually covered with Teflon insulation that is not shown in order to expose the structure of the thruster. Plasma was produced in argon by a helical antenna outside the quartz tube that was fed with radio frequency energy through a matching network at 13.56MHz. A retarding field energy analyzer (RFEA) and a Langmuir probe that either faced the annulus between the thruster tubes or the center of the tubes detected the ions accelerated by a current pulse through the thruster tubes. Inset 1 shows the structure of the RFEA without Teflon insulation. Inset 2 shows a cross section of the Teflon insulated thruster tubes.

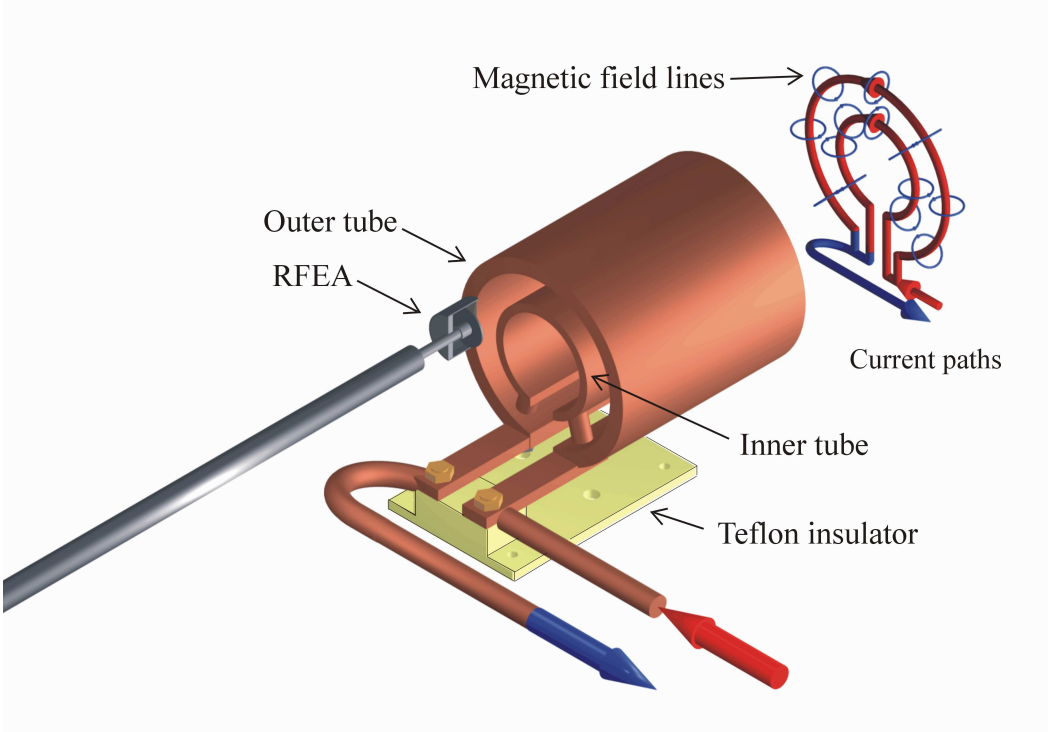

Figure 51 Concentric slit copper tubes carrying currents in the same direction create opposing magnetic fields in the gap between the tubes. When surrounded by plasma, magnetic reconnection occurs in a concentric current sheet that is formed between the inner and outer tubes. Magnetic energy is converted into heat and kinetic energy of a high velocity plasma jet. Plasma is ejected from the concentric gap between the tubes. The energy of the jet is measured with a Retarding Field energy Analyzer (RFEA). The Teflon insulation that covered the tubes to prevent shorting to the plasma is not shown.

An argon plasma was formed within the chamber and was excited by 13.56 MHz RF energy that was coupled into the plasma by a 10-turn helical antenna mounted on the outside of a 200mm diameter quartz tube. The antenna, with an impedance of approximately 1Ω with a phase angle of approximately $+88^{o}$, was fed from a purpose-built matching network that was attached to one end of the plasma chamber. The forward power delivered to the plasma was measured with a wattmeter that was part of the 1kW 13.56MHz Henry Radio power supply that delivered up to 250W through a 50Ω cable to the matching network. The antenna was matched to the power supply at an impedance of 50Ω with a phase angle of 0.0^{O} using a Hewlett Packard 4193A vector impedance meter before the power supply was connected.

Argon was chosen as the experimental gas since it was readily available and inexpensive compared to xenon, a commonly employed spacecraft propellant.

The chamber was evacuated to approximately 5×10^{-6} Torr before argon was admitted through an MKS type 247 flow controller set to maintain pressures ranging from 5×10^{-5} Torr to 5×10^{-3} Torr that was measured with a Pfeiffer Single Gauge pressure gauge.

9.4 Measurements with a Langmuir Probe

No magnetic field was present when the Langmuir probe measurements were made and Langmuir probe measurements were made when the plasma was stable and no current was being passed through the thruster tubes. The measurement circuit consisted of the Langmuir probe that was connected to a ramp generator that drove a high voltage amplifier and a difference amplifier that measured the probe current. The probe current was detected as a voltage across a resistor and that voltage was recorded with a digital oscilloscope that was connected to a computer running a Labview program. The accuracy of the measuring system was determined by replacing the Langmuir probe with a fixed resistor.

The plasma density inside the experimental chamber was measured with a Langmuir probe that was connected to a saw tooth wave generator that had a ± 150V output at a frequency of 30Hz. The resulting ion and electron currents that passed through a 561 Ω resistor were determined with an INA117 difference amplifier that can measure small differential voltages in the presence of common mode signals as high as ± 200V.

The method of determining the ion saturation current, the electron temperature (in electron volts) and the plasma density from the Langmuir probe measurements is shown in figure 54 and was based on the following calculations (Eq. 80 – Eq. 82).

If the electrons are Maxwellian, the electron current I_e is given by (Chen 2003 [229])

$$I_e = I_{es} \exp\left(e(V_p - V_s) / k_B T_e \right), \qquad \text{Eq. 80}$$

where I_{es} is the electron saturation current, V_p is the probe voltage, V_s is the plasma potential, k_B is Boltzmann's constant and T_e is the electron temperature in Kelvin.

The electron temperature is then be determined from the slope of the current-voltage curve via

$$e / k_B T_e = \ln\left(I_{es} / I_e \right) / \left(V_p - V_s \right) \qquad \text{Eq. 81}$$

Which is equal to $1/T_{eV}$ where T_{eV} is the electron temperature in electron volts.

Assuming that $T_e >> T_i$, the ion temperature, the plasma density n_i can be calculated using Bohm's approximation for the ion saturation current I_s (Merlino 2007 [230]):

$$I_{is} = 0.61 n_i e A_{probe} \sqrt{T_e / m_i}, \qquad \text{Eq. 82}$$

where e is the electron charge, A_{probe} is the probe area and m_i is the ion mass.

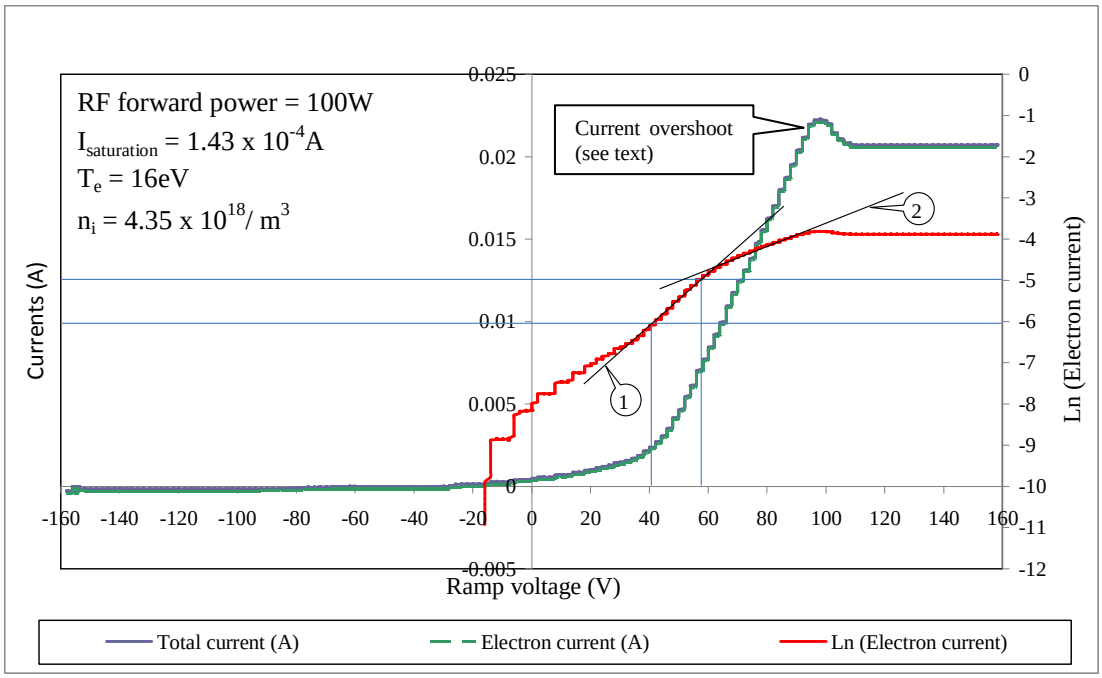

Figure 52 Determination of ion saturation current, electron temperature and plasma density from a plot of the current drawn by a 20 mm diameter Langmuir probe in argon plasma created by radio frequency energy at 13.56MHz. The plot shows two lines (line 1 and 2) that are used to determine the electron temperature. The intersection of lines 1 and 2 determines the electron saturation current and the slope of line 1, the natural logarithm of the electron current, gives the electron temperature directly in eV (Chen 2003 [229]).

In a typical experiment, the Langmuir probe measurement of the plasma density was made and then immediately followed by a measurement using the same probe of the average ion current resulting from 100 current pulses passed through the thruster tubes.

At a forward power of 100W from the 13.56MHz power supply, the ion saturation current was 1.43 x 10^{-4} A, the electron temperature was 16eV and the plasma density was 4.35 x 10^{18}/m^3. The range of experimental plasma densities was 1.0 x 10^{18} to 2.5 x 10^{19} /m^3

Noise was filtered from the data with a 50-point low-pass finite impulse response filter with a cut-off frequency of 50 kHz. Measurements were made with the 20mm diameter Langmuir probe of (1) the ion current from the centre of the thruster tubes (theta pinch) and (2) the ion current from a section of the annulus.

The current overshoot observed in the current-voltage characteristic of the Langmuir probe is evidently a well-known feature that occurs when the probe voltage is rapidly swept with a positive voltage ramp. It is apparently the result of the inertia of ions in a sheath when it changes from an ion-rich to an electron rich environment and has been observed previously [Stenzel and Urrutia 1997 [231]).

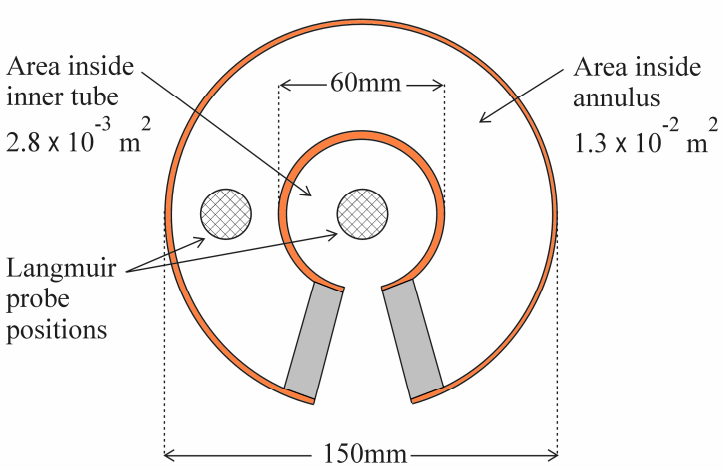

Figure 53 Ion currents were measured with a 20mm diameter Langmuir probe situated 25mm away from the face of the aperture between the inner and outer tubes of the thruster and at the same axial distance from the center of the concentric tubes. The current was measured with a difference amplifier and averaged over 100 driving current pulses supplied to the tubes. The total charge was determined by integrating the ion current over the duration of the driving current pulse. The Teflon insulation that covered the copper tubes and connectors is not shown. The area of the annulus is 4.6 times that of the area inside the inner tube. The 30^{o} sector that was cut out of the tubes to create the inner and outer circuits reduced the magnetic field strength in the annulus and in the center tube by 27% compared to a solenoid of the same diameter. The drawing is to scale.

9.5 Measurements with the Retarding Field Energy Analyser

A single grid retarding field energy analyser was used to measure the energy of ions accelerated by the thruster; RFEAs are commonly used to measure the energies of ions in beams of charged particles (Simpson 1961 [232]).

Depending upon the field strength, an axial magnetic field may affect the passage of ions through the aperture of a RFEA so that ions with a particular momentum will enter the RFEA while those with a momentum above and below that value may be rejected (Simpson 1961 [232]). It was assumed that ions with a small radial momentum and high axial momentum, those of particular interest in these experiments, were not obstructed by that effect. Similarly, although the acceptance angle of a RFEA can have a significant effect on the number of particles entering the device, it was assumed that the large entrance aperture (25mm) would have greatly reduced any effect of the acceptance angle on the ion flux entering the RFEA.

In order to separate ions from electrons in a charged particle beam entering the RFEA, a negatively charged grid at the entrance is used to repel the electrons. However secondary electrons generated inside the RFEA may contribute to the measured current. In this experiment, the secondary electron emission coefficient is small ($<10^{-1}$) for ions with an energy less than 100eV (Grondona 2001 [233]) while the grid voltage (-150V) was expected to

be sufficient to repel electrons at the thruster energies investigated. As discussed below, repelling space charge between the grid and the collector plate, created by ions inside the analyzer, may have reduced the measured energy of the ion flux.

Although ion currents were measured with the RFEA, they were smaller than anticipated from the Langmuir probe measurements. In order to reduce the loss of ions to the negatively charged body of the RFEA that was connected directly to the grid, the body of the device was completely insulated with a Teflon cover. A previous study of a theta pinch thruster reported similar difficulties in obtaining repeatable measurements of ion energies using a similar energy analyzer that consisted of a negatively biased probe inside a Faraday cup with a small entrance aperture (Turner 1969 [234]). The assembled probe complete with the Faraday cup had been calibrated in stable plasma. Modifications to both the probe bias voltage and aperture size made no difference to the measurements that were not considered reliable. The reasons for this difficulty are not apparent.

In contrast, the equipment used to measure the ion flux and ion energy in this experiment had been tested in an entirely different investigation (Bathgate et al 2016 [235]) and the accuracy of the entire measurement system was verified with a known current source (fig. 61).

Table 13 is a summary of the measured and calculated experimental parameters.

Experimental parameters and conditions	**Value**
Argon pressure range	5×10^{-5} to 5×10^{-3} Torr
Current pulse repetition rate	1.0Hz
Current pulse length	1.0msec
Plasma density range	1.0×10^{18} to 2.5×10^{19} /m^3
Ion saturation current range	$1.4 – 2.8 \times 10^{-4}$ A
Alfven velocity at I_t = 1540A, $n_i = 1.0 \times 10^{18}$ to 2.5×10^{19} /m^3	3.8×10^{4} to 7.6×10^{3} m/s
Total inductance of tubes (calculated)	2.2×10^{-8}H
Resistance of outer tube (calculated)	$4.0 \times 10^{-5}\Omega$
Resistance of inner tube (calculated)	$8.0 \times 10^{-6}\ \Omega$
Resistance of tubes in parallel (calculated)	$6.7 \times 10^{-6}\Omega$
Distance of probes from aperture	25mm
Langmuir probe diameter	20mm
Low pass 50 point finite impulse response data filter	50 kHz roll off

Table 13 Summary of experimental parameters and conditions

Table 14 shows that the experimental conditions were comparable to those obtained in previous magnetic reconnection experiments listed in Table 12.

Particle density (per m^3)	**Electron temperature**	**Global scale**	**Field strength (1500A)**	**Reconnection time scale**
$1 \times 10^{18} - 3 \times 10^{19}$	14eV - 16eV	0.12m	0.0114T (114G)	$\leq$ 1ms

Table 14 Conditions in the experimental apparatus. The particle density and electron temperature were determined from Langmuir probe measurements. The field strength inside the outer tube is calculated from a formula derived from the Biot-Savart law for a coil with a 30^o segment removed. The reconnection time scale is taken as the duration of the driving current pulse.

9.6 Magnetic field structure of the thruster

The magnetic field strength arising from the currents in the thruster were calculated at points inside and outside the tubes using the Biot-Savart law. The 4^{th} order Runge-Kutta method was used to approximate the first order differential equation that describes the magnetic field and those values were used to plot the field lines (fig. 54). The tubes were connected in series so that the currents were the same in both although the exact distribution of those currents in the tube walls was uncertain. For the purpose of calculation the 1500A current in the tubes was divided between 121 single turn coils each separated by 1.0 mm. A plot of the magnitude of the field strength from the central axis of the thruster to the outside of the thruster was made using the values obtained from the plot of the field lines (fig. 55).

The magnetic field plots show that partial cancellation between the magnetic fields inside the thruster occurs for much of the length of the thruster implying that the fields are anti-parallel and so, in accordance with Swisdak's (Swisdak et al 2010 [219]) requirement for anti-parallel fields, reconnection should occur in that region.

The field strength was at a minimum at a radius of 40 mm and accordingly, the axes of the retarding field energy analyzer and the Langmuir probe were placed at that position to record the ion and electron currents produced by the interaction of the opposing magnetic fields.

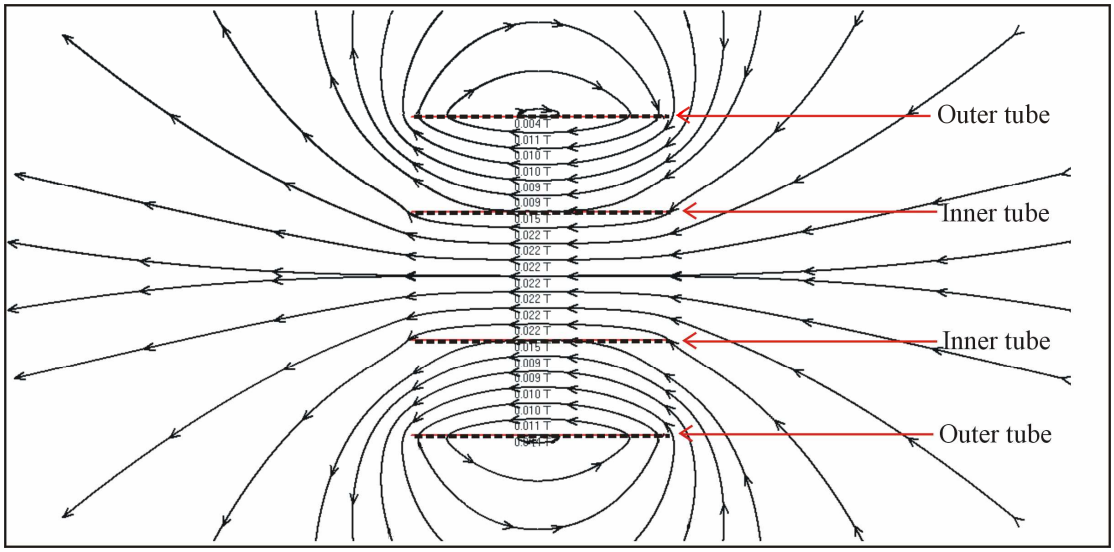

Figure 54 Cross section of the magnetic field arising from currents in the inner and outer walls of the thruster. The calculated field strength is shown in the center of the tubes and is the sum of the magnitude of the fields arising from equal currents in the inner and outer tubes. Field strength falls to a minimum in the annulus between the tubes and in the presence of a plasma, reconnection between the opposing magnetic fields drives electron and ion currents out of the thruster.

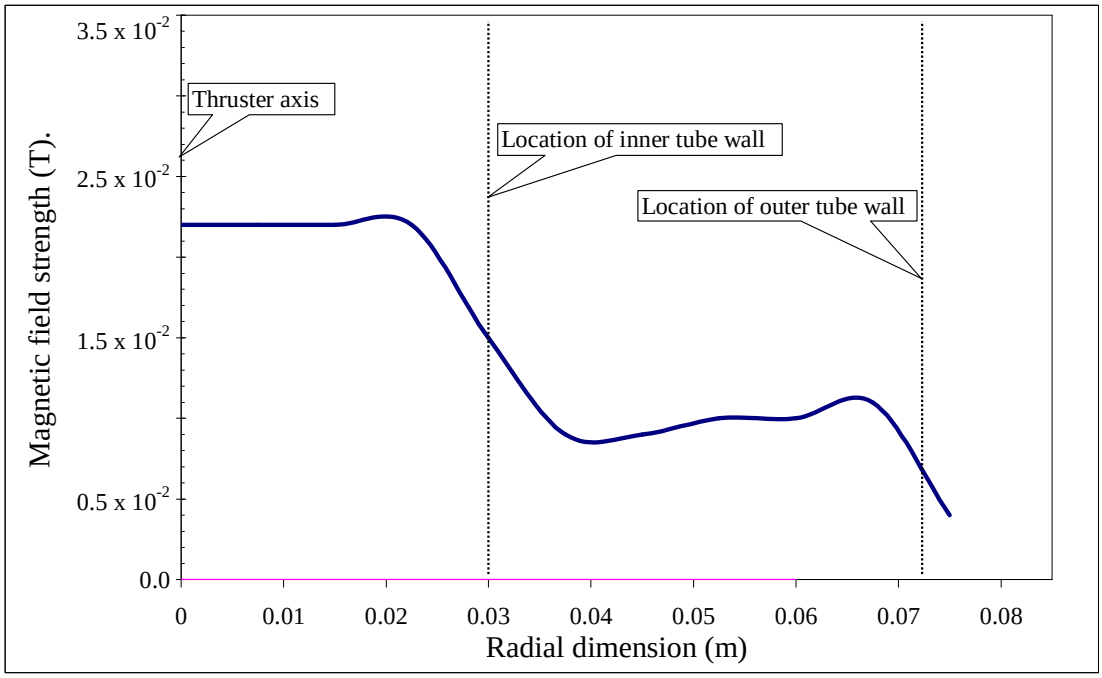

Figure 55 Plot of the magnetic field strength along a radial line from the axis of the thruster to the outer tube wall. The magnetic field strength reaches a minimum in the gap between the inner and outer tubes where the opposing fields cancel. Reconnection is expected to occur at the field minimum located approximately 40 mm from the axis of the thruster.

9.7 Results

9.7.1 Ion currents as a function of Argon pressure.

Ion currents produced by current pulses of 425±10 A that were passed through the thruster tubes that were connected in parallel (fig. 53) were measured with a Langmuir probe at argon pressures of $5x10^{-5}$, 1 x 10^{-4} and at 3 x 10^{-4} Torr at forward powers of 100W, 150W, 200W and 250W (fig. 56). The ion current increased with decreasing pressure corresponding to an increase in the mean free path of the ions. The ion currents were integrated over time from the beginning of the driving current pulse to the end of the sampling interval. The resulting integrated charge was plotted as a function of plasma density for three different pressures.

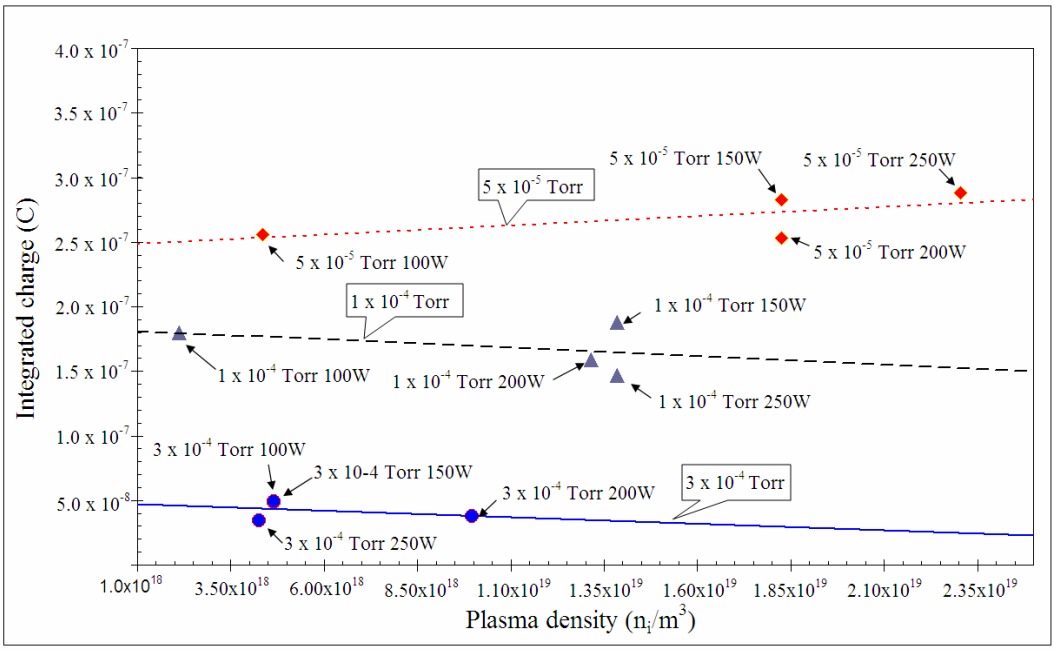

Figure 56 Integrated charge (measured with a Langmuir probe) produced by a thruster current pulse of 425±10 A at three pressures. At each pressure, total charge collected by the probe was measured as a function of plasma density and RF forward power. The collected charge increased significantly as the pressure was reduced. The difficulty in maintaining constant low pressures is the cause of the scatter in the data. Each data point is an average of 100 measurements and is labeled with the average argon pressure over the sampling time. Trend lines for each pressure series are indicated with callouts.

9.7.2 Ion Currents from the Theta Pinch zone and from the Annular reconnection zone

Ion currents produced by current pulses through the parallel connected thruster tubes at a constant RF forward power (200W) and at a constant pressure (2 x 10^{-4} ± 1 x 10^{-4} Torr) were measured with a 20mm diameter Langmuir probe for 11 different capacitor bank voltages (+20V to +120V in steps of 10V). The probe was kept at a voltage of -150V for all measurements. The total charge flowing into the Langmuir probe – determined by integrating

the ion current over the duration of the driving current pulse – was found to be approximately 3.5 times larger when the probe faced the annular region between the tubes than when the probe faced the center of the inner tube (see fig. 53 for the probe locations).

The probe facing the annulus detected a substantial electron current with an energy > 150 eV – as shown by the initial negative going excursion of the probe current (fig. 57) – while the probe facing the centre of the tubes only showed a small electron current and an ion current similar in magnitude to that detected by the probe facing the annulus (fig 58). The appearance of a significant electron current within microseconds of the rising current and resulting magnetic field within the thruster tubes is strong evidence for the acceleration of electrons by magnetic reconnection in the annular region.

Noise induced in the probe caused by the changing magnetic field in the thruster tubes was at least 2 orders of magnitude smaller than the signal.

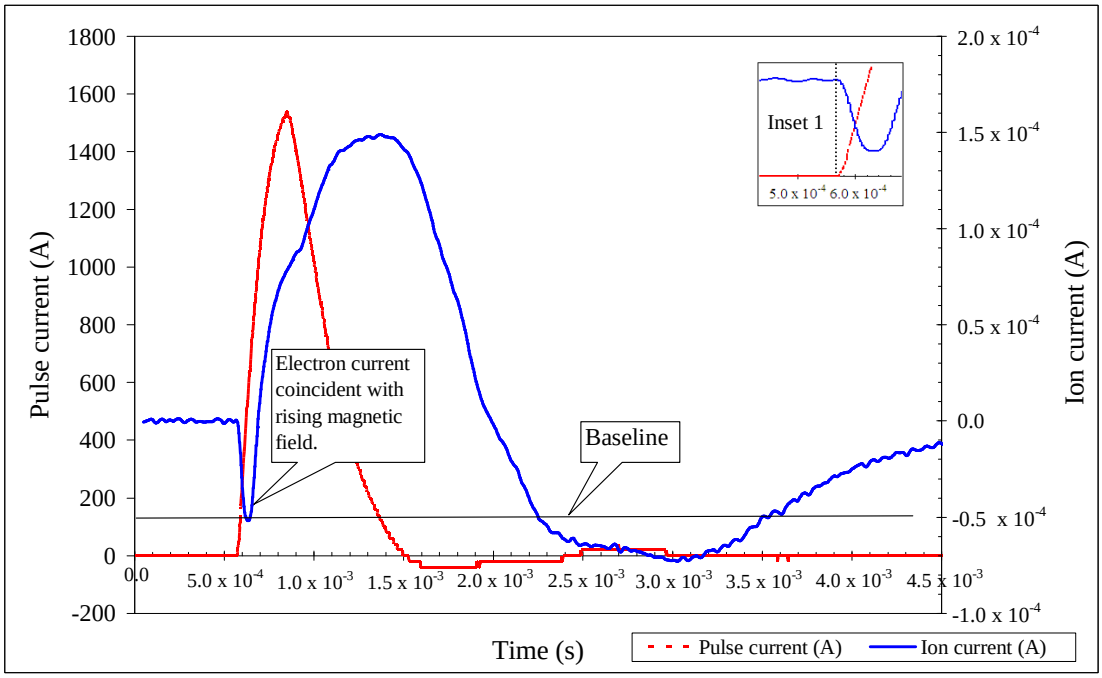

Figure 57 Current detected by a Langmuir probe placed facing the annulus (see fig. 53) at a constant RF forward power (200W) and at a constant pressure ($2 \times 10^{-4} \pm 1 \times 10^{-4}$ Torr). The initial negative excursion of the probe current is presumed to be electrons with an energy > 150 eV since the probe was kept at a voltage of -150 V. The total charge detected by the probe was determined by integrating the probe current from the time where the negative going probe current was greatest (the baseline) until the end of the sampling period, 2.5×10^{-3}s. The inset (Inset 1 on a different scale) shows the coincidence of the initial electron current and the rising thruster tube current. The baseline was used as the zero current reference for the numerical integration of the current.

The integrated charge measured with the Langmuir probe at the face of the annulus and at the center of the thruster tubes were then measured as a function of the energy discharged into the

thruster by each current pulse. Clearly, the total charge rises slowly with the applied pulse energy. The peak current density measured in the annulus was 0.47A/m^2 or 6.2 mA for the area within the annulus (fig. 53).

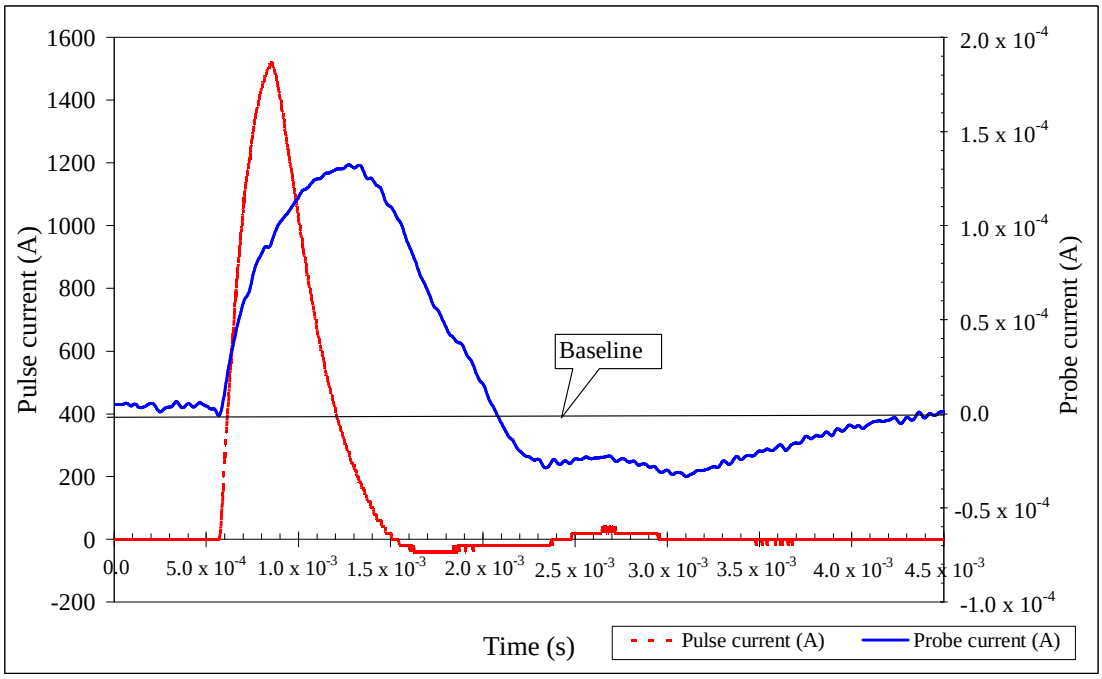

Figure 58 Current detected by a Langmuir probe placed facing the center of the tubes (see fig 53) at a constant RF forward power (200W) and at a constant pressure ($2 \times 10^{-4} \pm 1 \times 10^{-4}$ Torr). The total charge detected by the probe was determined by integrating the current from the point where the driving pulse current exceed 100 A, the point that corresponded to the rise of the probe current, and the end of the sampling period at 2.5×10^{-3}s. The baseline was used as the zero current reference for the numerical integration of the probe current.

The currents from the region of the annulus and from the region of the theta pinch measured as a function of pulse energy input differed significantly (fig. 59). The large peak in the current from the annular zone at approximately 5.6J was unlikely to be an artifact since the measurements shown on the chart are the average of 100 samples at each point. The marked differences between the currents detected from each zone at lower energies may well be the consequence of the different accelerating mechanisms operating in each zone. The decline in the current from the theta pinch at a pulse energy input > 15J that is correlated with the magnetic field strength may be the result of the effect of a magnetic mirror forming at higher magnetic field strengths that obstructed the ion flux. Further investigation of these phenomena is warranted.

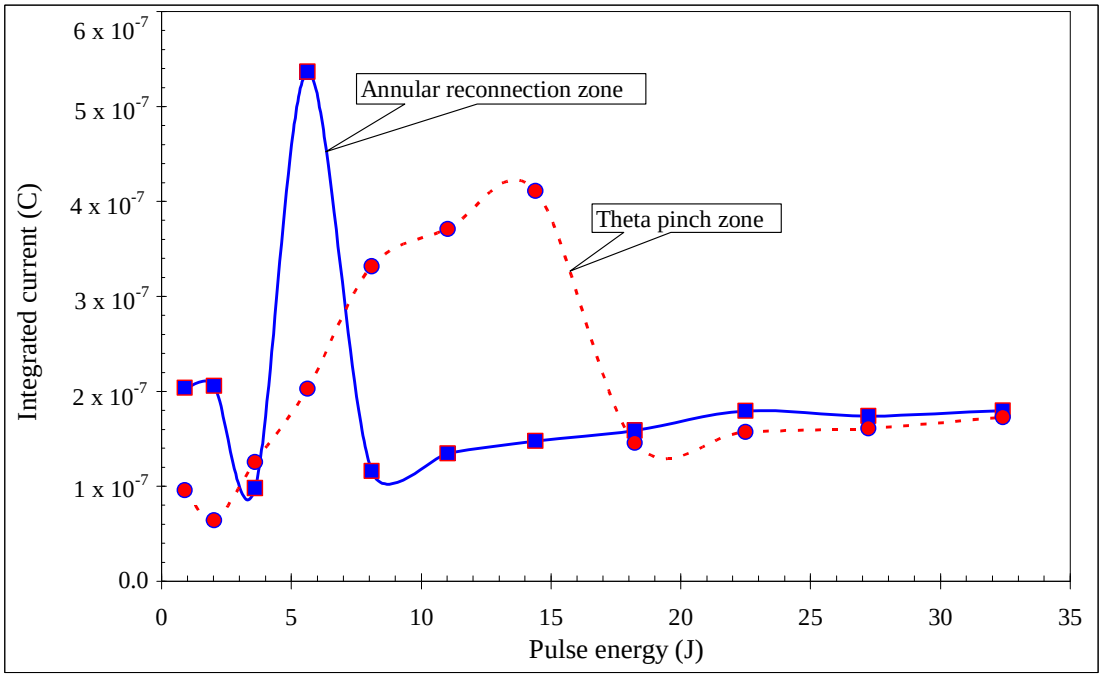

Figure 59 Total charge detected by Langmuir probes facing the annulus and facing the centre of the thruster tubes (theta pinch) at a constant RF forward power (200W) and at a constant pressure ($2 \times 10^{-4} \pm 1 \times 10^{-4}$ Torr). Each point is the average of 100 separate measurements made at 1 second intervals that were then filtered and integrated to determine the charge.

9.7.3 Currents from the Annulus measured with the RFEA

The RFEA was used to measure currents produced by the magnetic interactions in the annulus in a similar manner to previous magnetic reconnection experiments (Brown et al 2002 [236]). In that report the magnitude of ion currents aligned with the Alfvenic outflow were much larger (MA/m^2) than those measured in experiments reported in this paper ($0.5A/m^2$) and were the result of a large reconnection electromotive force $\varepsilon = \int \mathbf{E} \bullet \mathbf{dl} \approx vBL$ where L is a characteristic length of the system along the electric field. In that case $\varepsilon = vBL \leq (10^5$ m/s)(0.05T)(0.1m) = 500V where v is the ion velocity, B the magnetic field strength and L the global scale.

The reconnection electromotive force $\varepsilon = vBL \leq$ (350m/s)(0.011T)(0.12m) = 0.5V in experiments reported in this paper is much smaller than Brown's observations as is the resulting ion energy. The inflowing ion velocity v is estimated by using Faraday's law to obtain the electric field strength arising from the changing magnetic field and then using the formula for the $\mathbf{E} \times \mathbf{B}$ drift to determine the resulting acceleration of ions. The estimated inflowing ion velocity is 350m/s.

The small currents measured by the RFEA, 2 orders of magnitude less than those measured by the Langmuir probe, made it difficult to discriminate between the currents produced by the

effects of different driving pulse energies. However, since an ion current was detected even when the plate was 130V positive with respect to the grid and thus would have repelled ions of lower energy, it was evident that ions had been accelerated to energies > 130eV (fig. 60). Despite that difficulty, it was clear from the Langmuir probe measurements that ion currents were produced in the annulus by the driving pulse energies (fig. 57) while the RFEA measurements indicate that the energies of ions from the annulus exceeded 130eV in all cases. The fact that the currents from the theta pinch and annulus are similar suggest that the magnitudes of the currents are a function of the experimental equipment rather that any limitation imposed by the physics of the device itself. High power theta pinch thrusters have been proposed for deep space missions (La Ponte 2000 [237]).

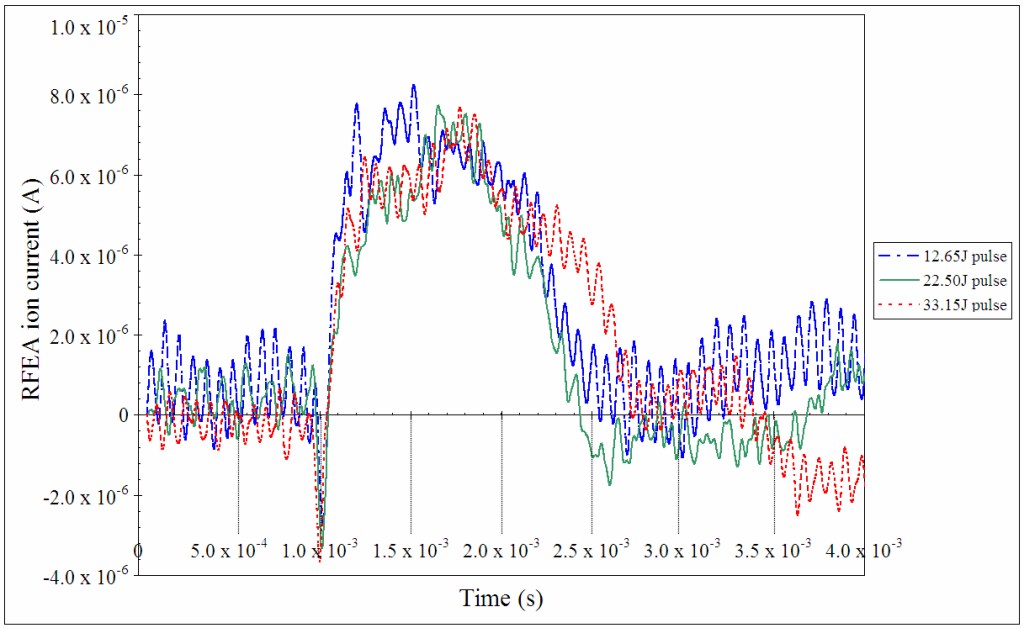

Figure 60 Ion and electron currents from the RFEA facing the annulus at a grid voltage of -150V and a plate voltage of -20V indicated that ions were accelerated to energies > 130eV by the thruster at all driving pulse energies since the probe being 130V more positive than the grid, would have repelled ions at lower energies . A poor signal to noise ratio obscured the differences in the magnitudes of ion currents at different driving pulse energies. Electron currents greater than 150eV were detected at each pulse energy. 100 samples were taken at each pulse energy and the data was filtered with a 50-step low pass finite impulse response filter. The source of the approximately 16kHz oscillation is unknown.

9.8 Analysis

The integrated charges that were measured with the Langmuir probe were proportional to the driving pulse current both in the annulus of the thruster and at the centre, demonstrating that the interaction between the magnetic fields in the thruster and the plasma accelerated charged particles. The ion currents arising in the annulus and reaching the Langmuir probe were approximately 3.5 times larger than those measured at the center and were preceded by a

relatively large electron current of brief duration whereas the ion current observed at the centre of the tubes was not preceded by any significant electron current.

The observation of accelerated charge particles from the annulus suggests that magnetic reconnection is accelerating the plasma out of the annulus since in a theta pinch thruster where the plasma is tied to the magnetic field lines, the plasma is accelerated by the combined effect of magnetic pressure, of magnitude $B^2/2\mu_0$ and magnetic tension of magnitude B^2/μ_0 while in magnetic reconnection electrons are accelerated by whistlers or kinetic Alfven waves. Figures 57 and 58 demonstrate this difference with a significant electron current that corresponds with the rise of the driving current in the tubes appearing in the probe facing the annulus. In addition, the presence of high-energy electrons that could have been produced by magnetic reconnection is evident from the large electron current with energy in excess of 130eV that flows into the probe after the ion flux finishes (the probe voltage is set at -130V). A similar electron current flows into the probe following the ion flux detected at the centre of the tubes although whether the source of those electrons was the annulus or the centre of the tubes could not be determined since equipment constraints meant that the current from the annular and theta pinch zones could not be measured simultaneously.

Further evidence for magnetic reconnection is found from the ion speed calculated from the RFEA measurements since those values are within the range of Alfven velocities expected at the peak pulse current and measured plasma density. For instance at a plasma density of n_i = 2.65 x $10^{18}/m^3$, within the range of measured densities, and at a peak pulse current of 1540 A, the calculated Alfven speed, v_A = 2.5 x 10^4 m/s, is consistent with the ion velocity measured with the RFEA. In addition, the ~ 70:1 ratio of the estimated speed of the inflowing plasma (350m/s) to the outflow speed, 2.4 x 10^4 m/s, is within the range expected for acceleration by magnetic reconnection.

Based on the Langmuir probe measurements (fig. 56), the total charge accelerated across the area of the annulus by an energy of 5.6 J corresponds to a current of 0.53 mA over a period of 1 msec. Using this result and the measured ion velocity of 2.4 x 10^4 m/s, it is estimated that the thrust produced is 2.21 x 10^{-7} N and the thrust efficiency is 4.7 x 10^{-3}%.

9.9 Discussion

This investigation has shown that a simple modification to the well-known theta pinch plasma accelerator improves the outgoing flux of ions by a factor of approximately 4.6 at pulse energy inputs > 20J assuming that the flux of ions is proportional to the ratio of the area of the inner tube to the area of the annulus.

The experimental apparatus was constructed so that electrically conductive plasma – produced by RF energy in low-pressure argon – was exposed to a pulse of oppositely directed

magnetic fields in the annulus formed between two concentric copper tubes connected electrically in parallel.

While the thrust and thrust efficiency of the experimental device is low, experience with theta pinch thrusters has shown that an unimproved theta pinch thruster may achieve a thrust efficiency of 16% (La Ponte 2000 [237]) which suggests that the similar reconnection thruster could be improved significantly. There are obvious modifications that could substantially improve the performance of the experimental device from the present thrust efficiency of 4.7 x 10^{-3}%.

Firstly, the resistances of the inner and outer thruster tubes differ by a factor of 5 which means that the bulk of the current runs through the lower resistance inner tube, significantly reducing the symmetry of the reconnection region as well as the interaction between the opposing fields. Secondly, assuming that the ions have a temperature of 1.0eV, the width of the annulus (43mm) is approximately half of the estimated ion gyro-radius (82mm) at peak field strength. Since the thickness of the diffusion layer in reconnecting plasma is of the order of an ion gyro radius (Yamada et al 1997 [196]), a significantly larger device would be required for the unobstructed formation of a diffusion layer in order to accelerate ions by magnetic reconnection. The formation of a current sheet and the production of accelerated ions by reconnection has been measured in much larger devices, for instance between 750 mm wide plates separated by 320mm carrying a 100μs long 10kA current in a 1.5 meter diameter by 2.0m long chamber (Stenzel et al 1984 [223]) so it is reasonable to suppose that increasing the scale of the thruster would improve its performance. Although we have shown evidence for the occurrence of magnetic reconnection, it is apparent that the limitations of the experimental device have restricted the acceleration of ions by this process. Theory suggests that a device in which the annulus is of a similar dimension to the ion gyro-radius could significantly improve the performance of the thruster.

9.10 Conclusions

This investigation has shown that high velocity plasma jets suitable for a spacecraft thruster can be produced by magnetic reconnection in plasma using a simple device that consists of two concentric electrically conducting tubes in which a pulsed electric current flows.

The high energy electron pulse (>150eV) that is observed coinciding with the rise of the tube current is similar to observations of high energy electrons by the Cluster satellites that are confidently regarded as being accelerated by magnetic reconnection. The Cluster measurements show the presence of a similar super-Alfvénic electron outflow jet at least 60 ion skin depths downstream from the X-line (Phan et al 2007 [218]). That no electron jet was observed from the theta pinch region strongly suggests that the phenomenon was

associated with magnetic reconnection and was not the result of any effect of the current pulse on the ICP source.

The evidence for the occurrence of magnetic reconnection in the annular zone is substantial. (1) A significant electron current was detected in the current from the annular region that coincided with the rise of the magnetic field in the thruster. (2) In accordance with known reconnection physics, ion currents were found to increase as the plasma became less collisional. (3) The ratio between the estimated speed of ions flowing into the diffusion layer (350 m/s) and the measured speed of the out-flowing ions (2.50×10^4 m/s) was approximately 70. (4) Ions with energies greater than 130 eV corresponding to a speed of 2.50×10^4 m/s were detected with the RFEA and were comparable to the expected Alfven speed for the plasma density and magnetic field strength obtained. (Alfven speed = 3.8×10^4 to 7.6×10^3 m/s at I_t = 1540A, $n_i = 1.0 \times 10^{18}$ to 2.5×10^{19} /m^3).

These results provide strong supporting evidence for the occurrence of magnetic reconnection in the thruster.

Since both ions and electrons are accelerated simultaneously, the thruster does not need a neutralizer, a device that imposes life limits on Hall and gridded ion thrusters. Assuming that the ion current detected by the Langmuir probe is uniform across the areas of the annulus and inner tubes, the ion current accelerated by the annulus at a pulse energy input > 20J is approximately 4.6 times that accelerated by the theta pinch.

The physics of magnetic reconnection indicate that the inherent thrust efficiency η_t of an optimized thruster would be approximately 50%, the result of the conversion of the magnetic energy into a rough equipartition between the thermal and kinetic energies of the accelerated particles, a figure that would be increased by the effect of the magnetic nozzle formed by the diverging magnetic field produced by the currents in the thruster.

So long as the rise time of the magnetic field is sufficiently rapid to produce an electric field that could ionize the propellant gas, no RF supply would be needed to ionize the propellant and a device consisting of no more than the concentric tubes, a capacitor, a switch, a gas supply and a power supply could form a simple robust thruster (fig. 61).

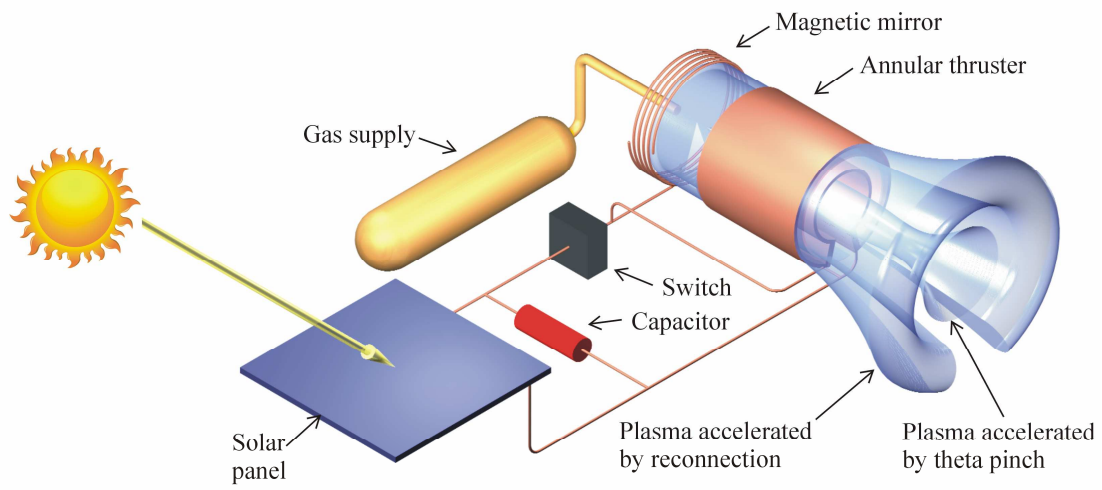

Figure 61 Schematic of a magnetic reconnection thruster installed on a spacecraft showing the most significant components. So long as the rise time of the currents in the concentric tubes is sufficiently rapid, the propellant gas will be ionized by the electric field produced in accordance with Faraday's law and no other means of producing an ionized propellant would be necessary. The resulting plasma would be expelled by magnetic reconnection from the annulus and by magnetic pressure and tension from the theta pinch. The plasma would be further accelerated by the magnetic nozzle formed by the magnetic field (not shown). A magnetic mirror coil could be used to reflect plasma expelled from the spacecraft end of the thruster.

10 Devices constructed for the investigations

10.1 Experimental apparatus (image)

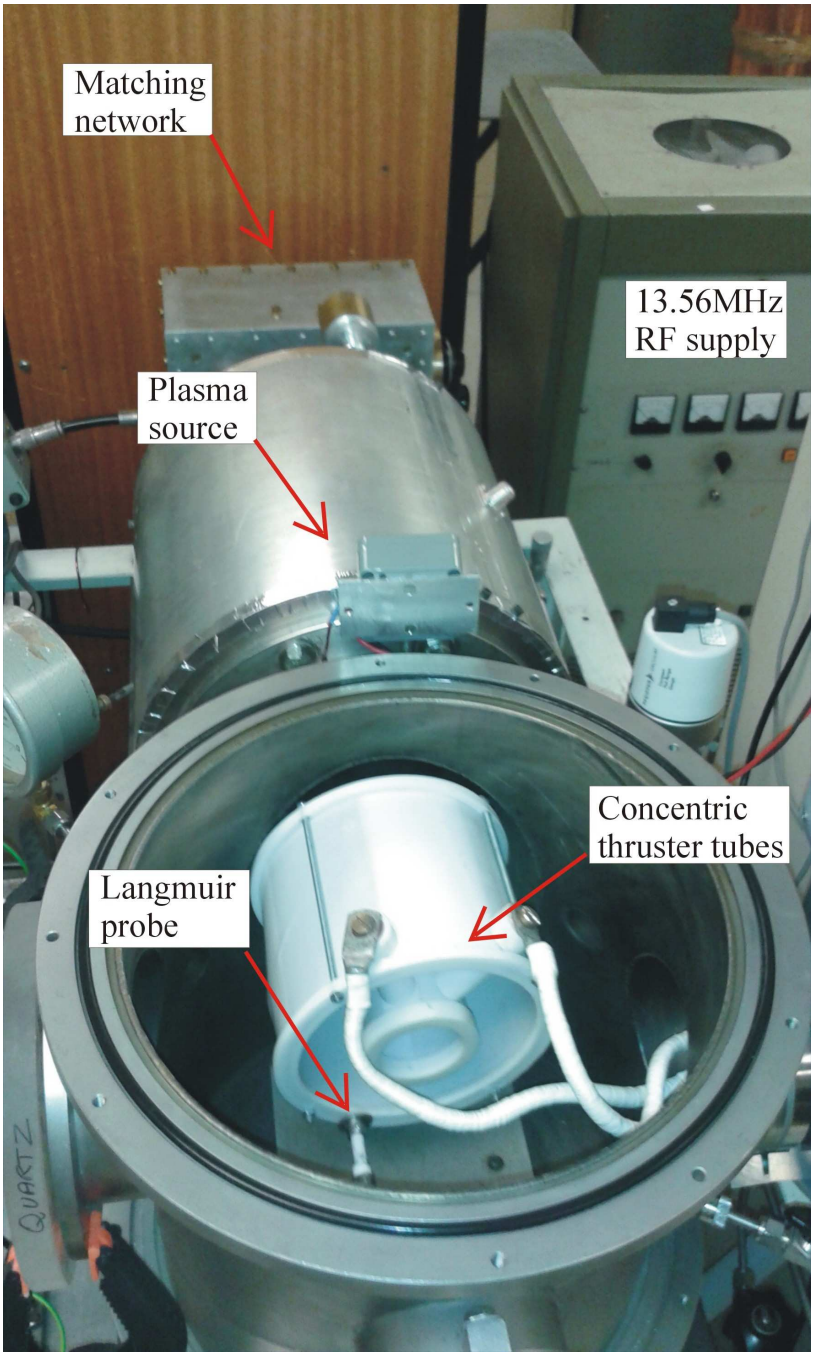

Figure 62 Experimental thruster mounted in a test chamber showing associated equipment including a 13.56MHz power supply connected to a matching network that drives an antenna surrounding a quartz tube that is under the plasma source cover. A current transformer measures the current supplied by an external pulsed high current generator to the thruster and either a Retarding Field Energy Analyzer or a Langmuir probe measures the ion current produced by the thruster when it is operated in an argon plasma. The thruster was rotated by 180^{o} to facilitate the connections to the pulse generator.

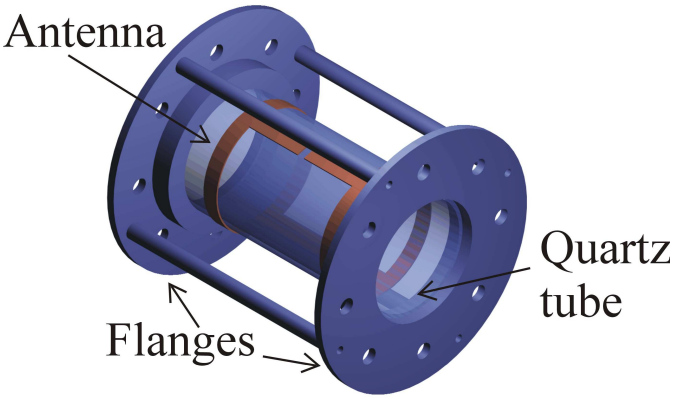

Figure 63 CAD drawing of the structure of the plasma source showing a helicon antenna mounted on the outside of a 150mm quartz tube together with supporting flanges that were bolted onto matching flanges on the vacuum chamber.

10.1.1 Experimental apparatus (schematic)

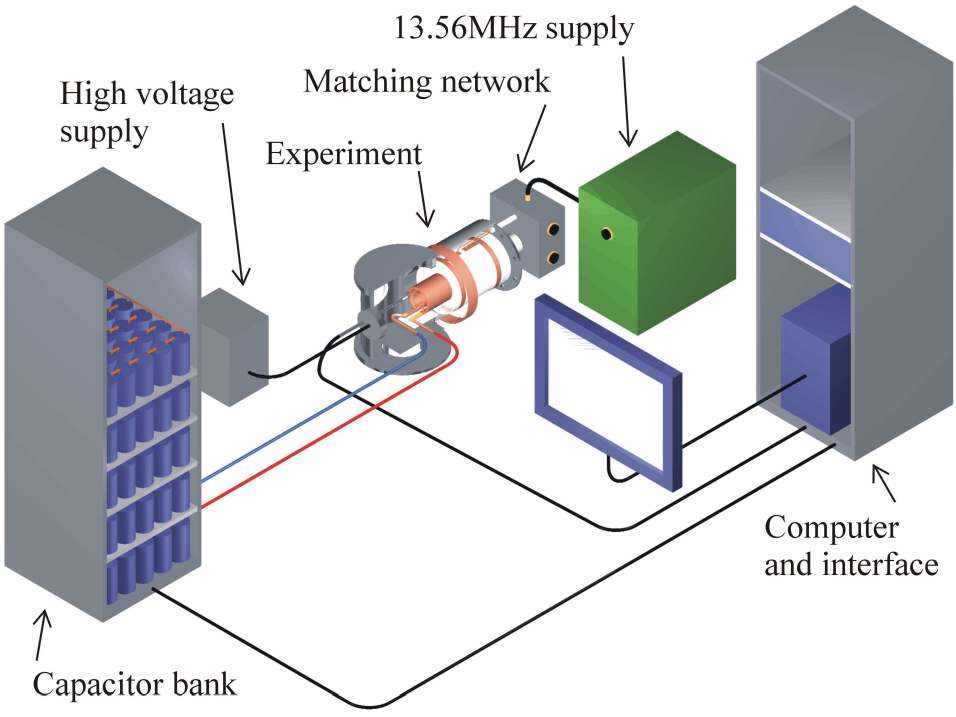

Figure 64 Magnetic reconnection experimental apparatus (schematic)

10.2 Isolating interface for magnetic reconnection experiment

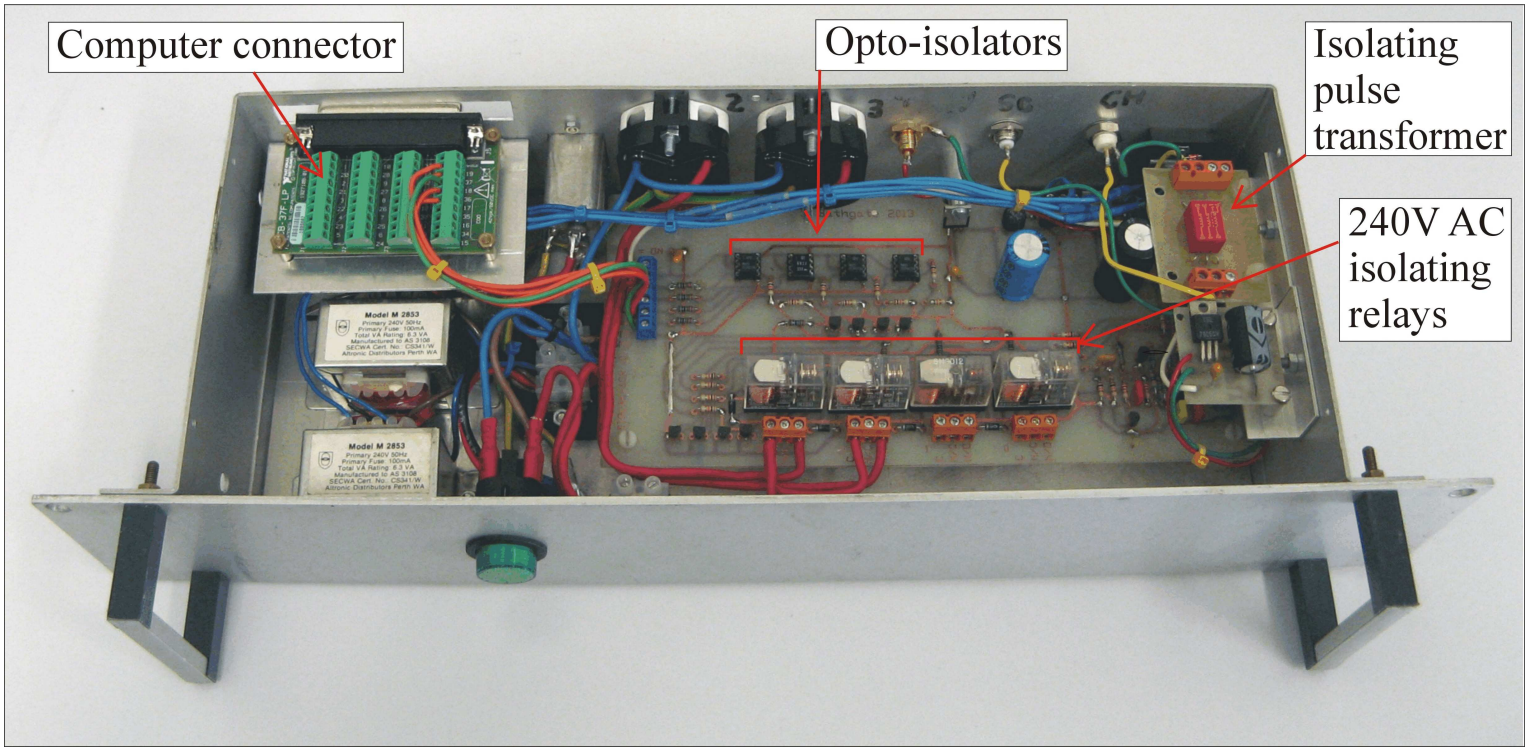

Figure 65. An interface box was constructed to enable a computer running a Labview program to control the experimental apparatus that had components that operated at high currents and voltages. The circuit had 4 logic outputs and used 4000V opto-isolators to drive transistors that (1) switched a 5V output to trigger the oscilloscope (2) switched a relay that was used to turn on a power supply for the magnet windings or (3) switched on a 30V 10μS output pulse to trigger the high voltage pulse generator. The output to the pulse generator was coupled through an isolating transformer. A computer connector was purchased from National Instruments and a circuit board was designed and constructed to interface between that connector and the experimental equipment. The circuit diagram and the circuit board layouts are shown on the following pages.

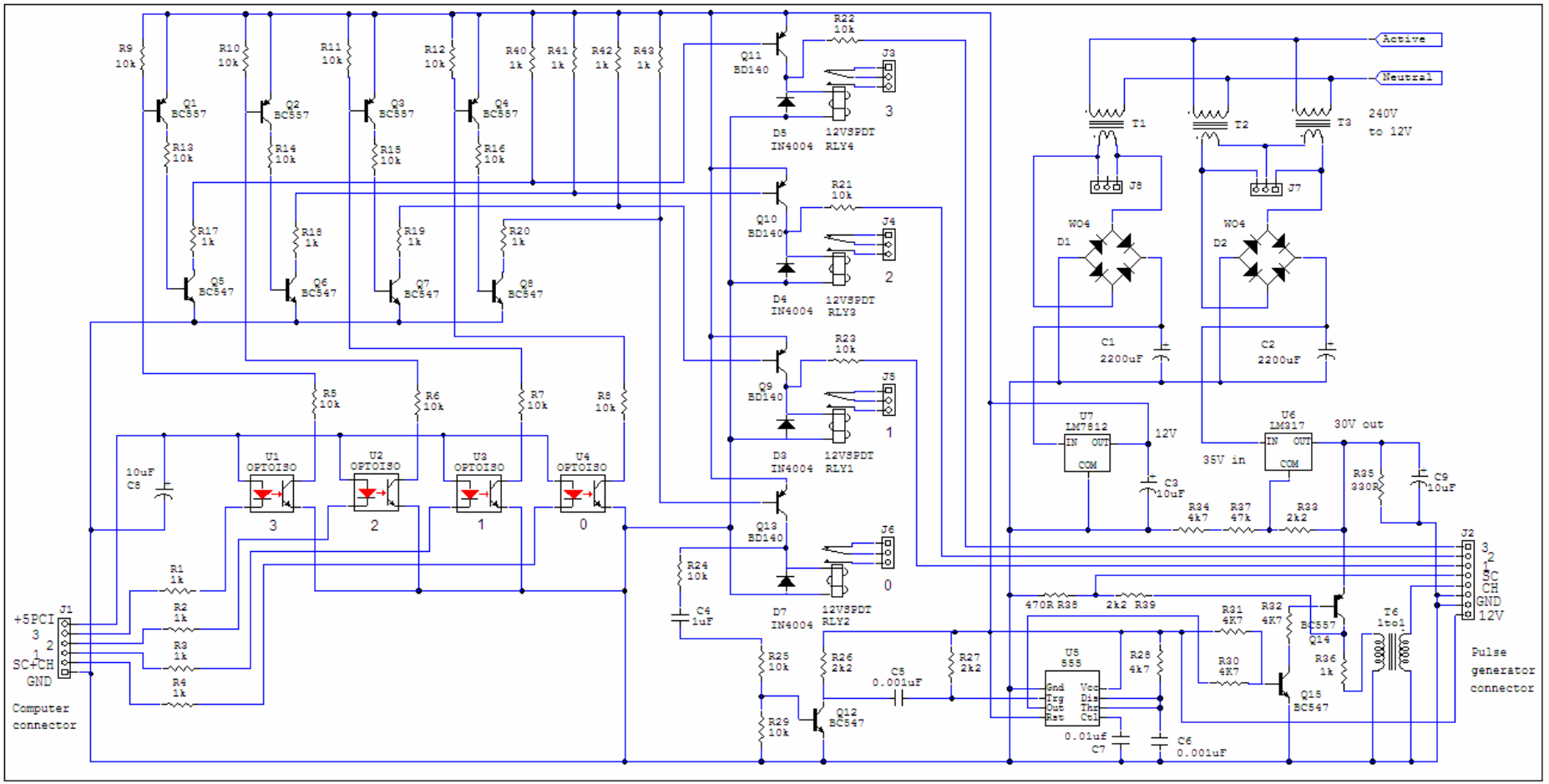

Figure 66 Circuit diagram of interface box. A 555 timer generates 10µS pulses when triggered by the computer through opto-isolator U4 that Q14 delivers to an isolation transformer T6 that delivers 30V trigger signals to the high current pulsed power supply that could deliver up to 3500A to the thruster.

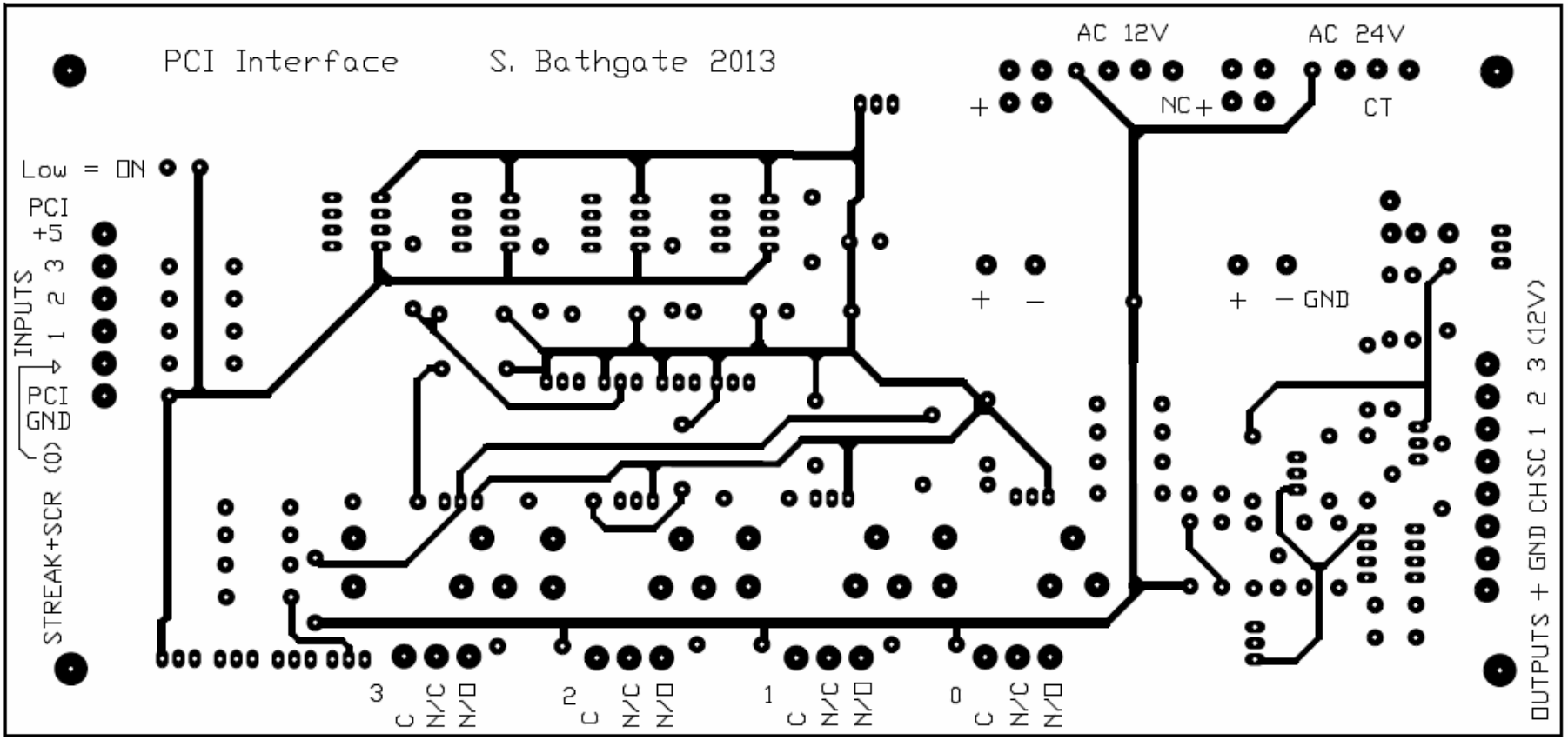

Figure 67 PCB layout of interface box top layer

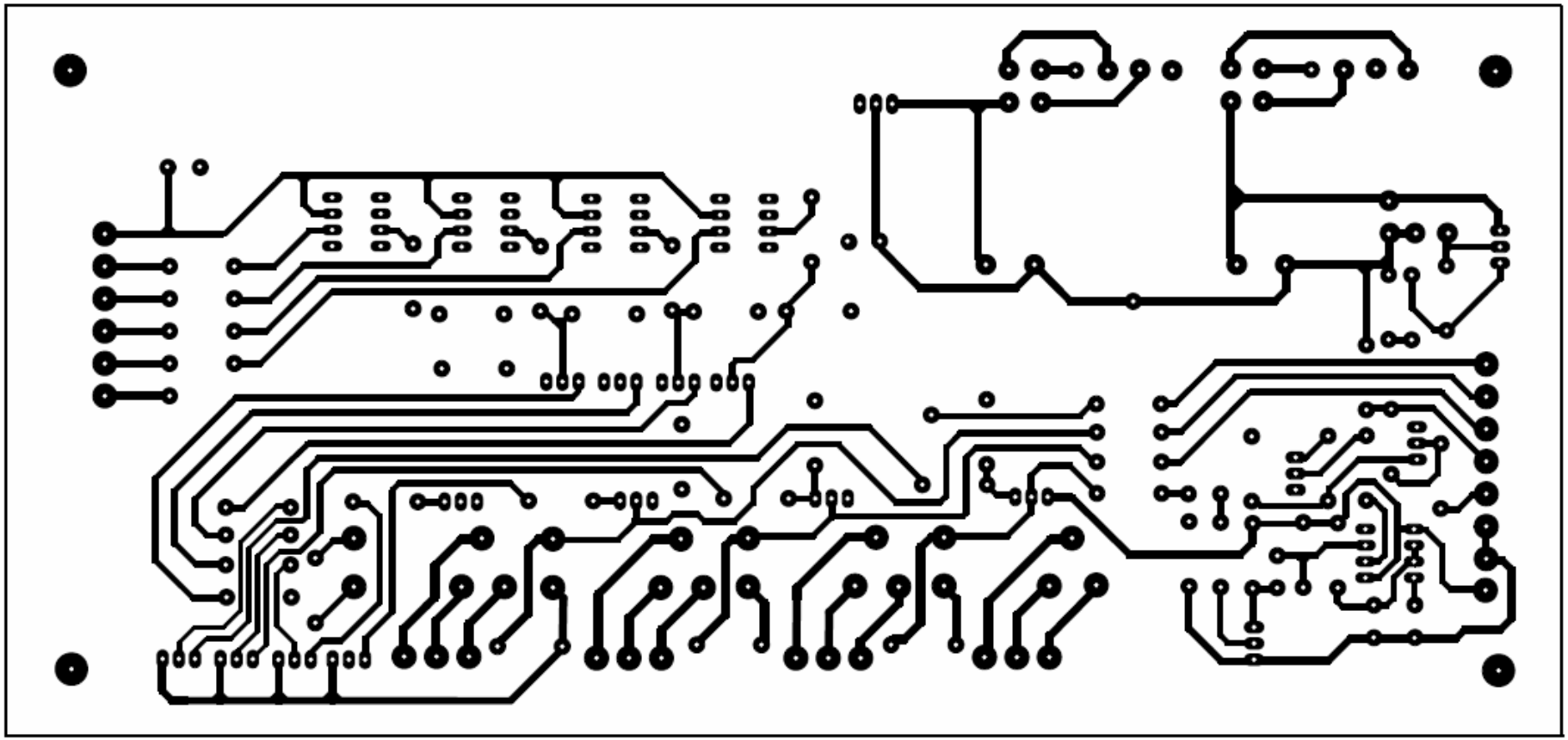

Figure 68 PCB layout of interface box bottom layer

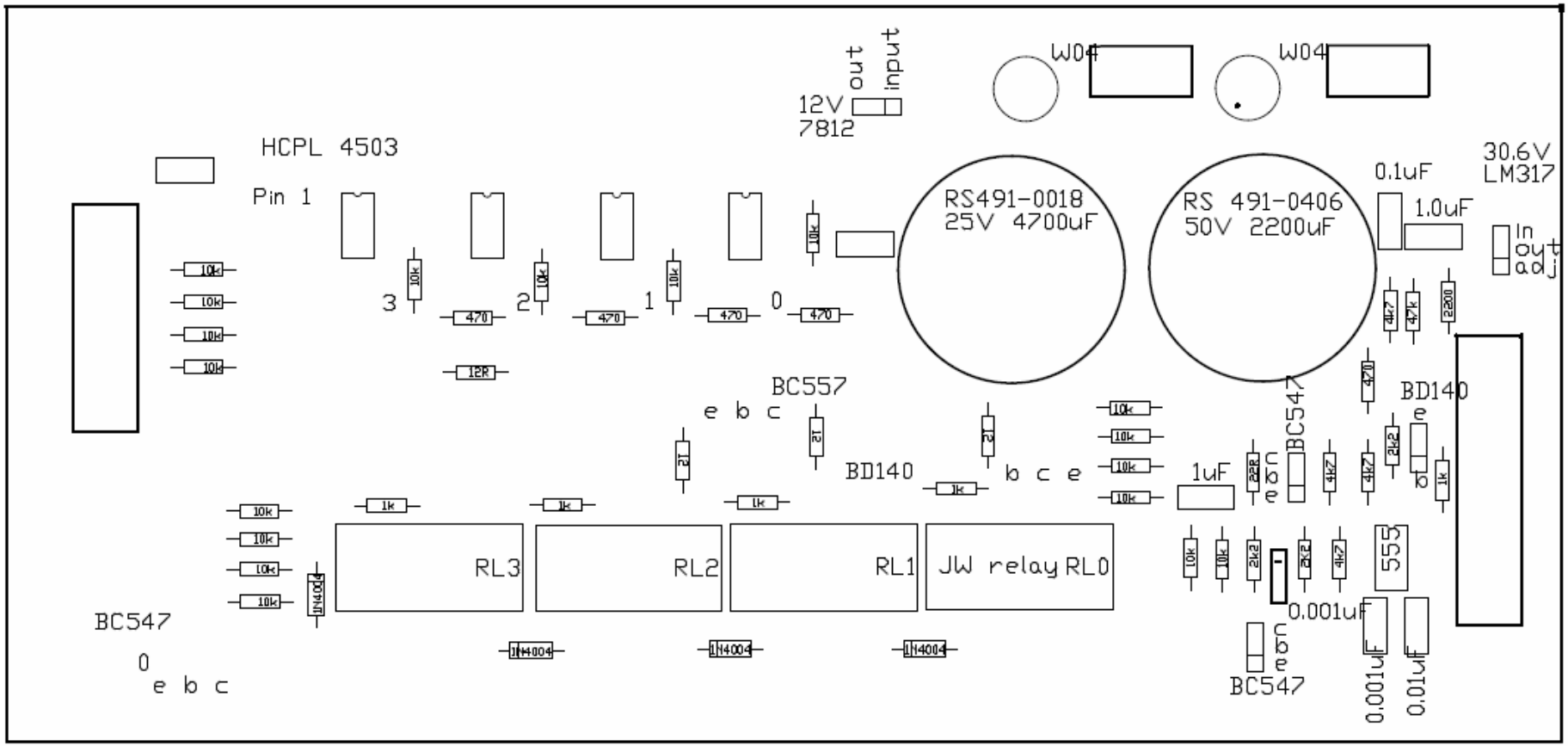

Figure 69 PCB layout of interface box top overlay showing component locations

10.3 +/- 160V DC power supply

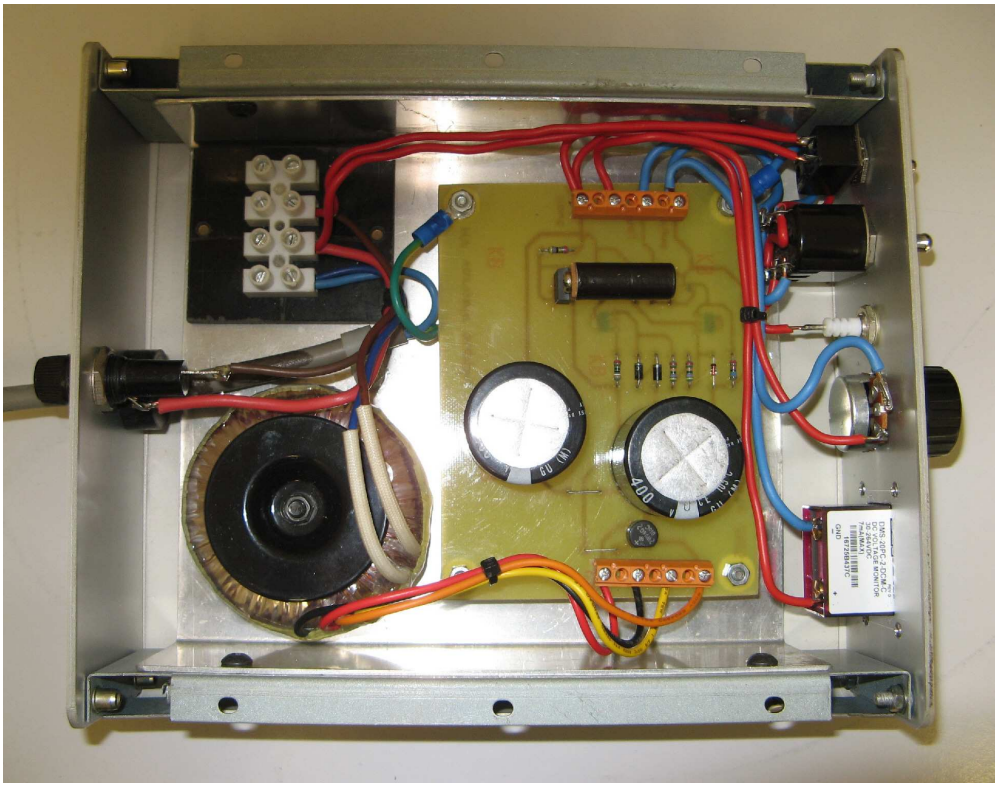

Figure 70 Variable ± 160 V DC power supply built to drive the Retarding Field Energy Analyzer

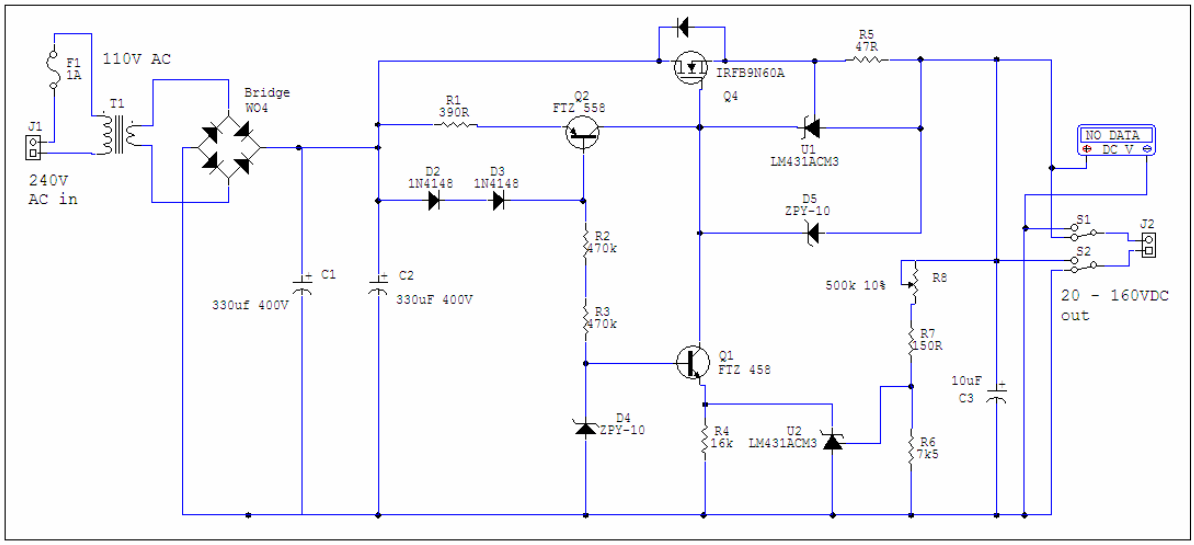

Figure 71 Circuit digram of the variable ±160 V DC power supply. The circuit was modified from an original design by Alexander Frank, ETH Quantumoptics (2008)

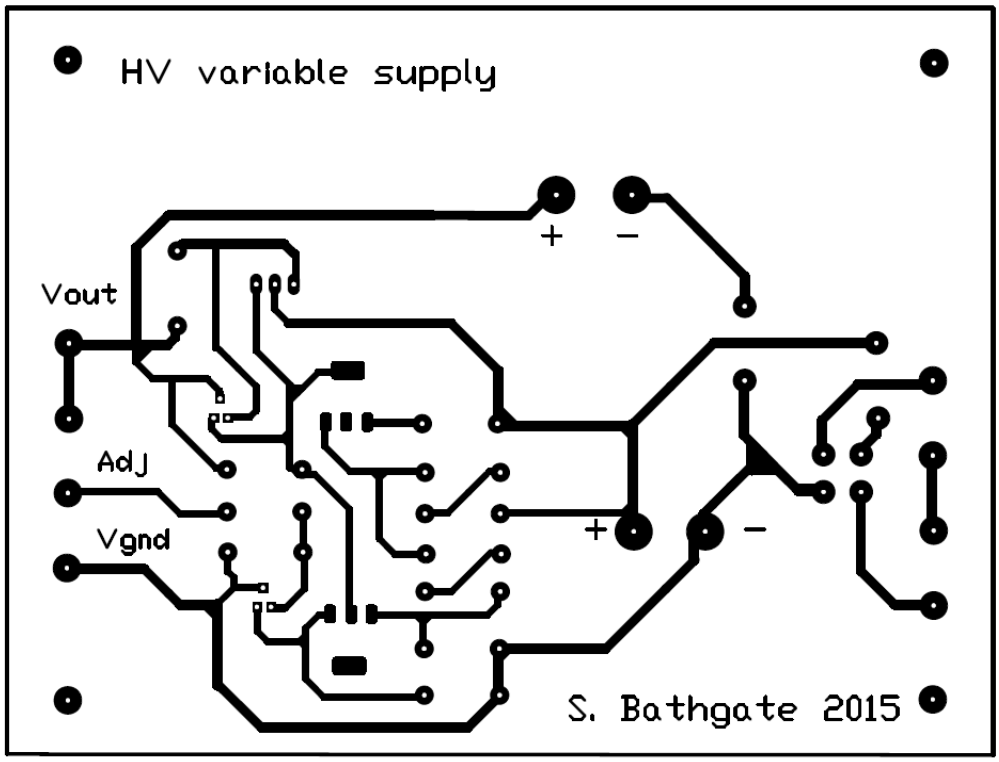

Figure 72 PCB layout of 160V DC power supply bottom layer

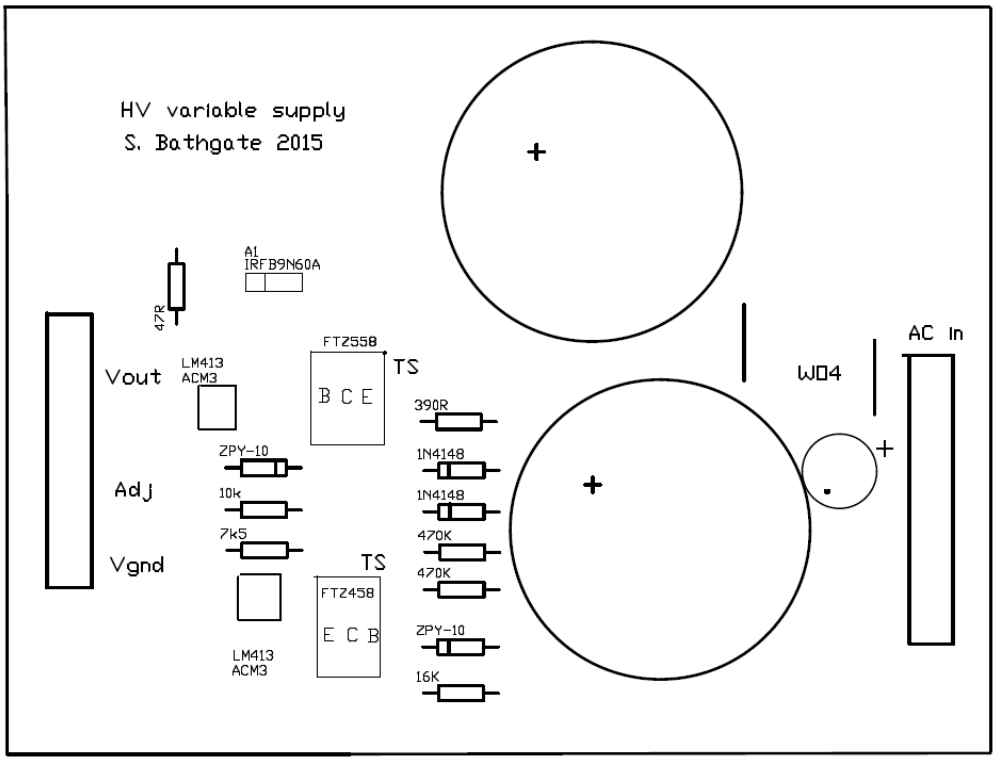

Figure 73 PCB layout of 160V DC power supply top overlay showing component locations

10.4 Difference amplifier

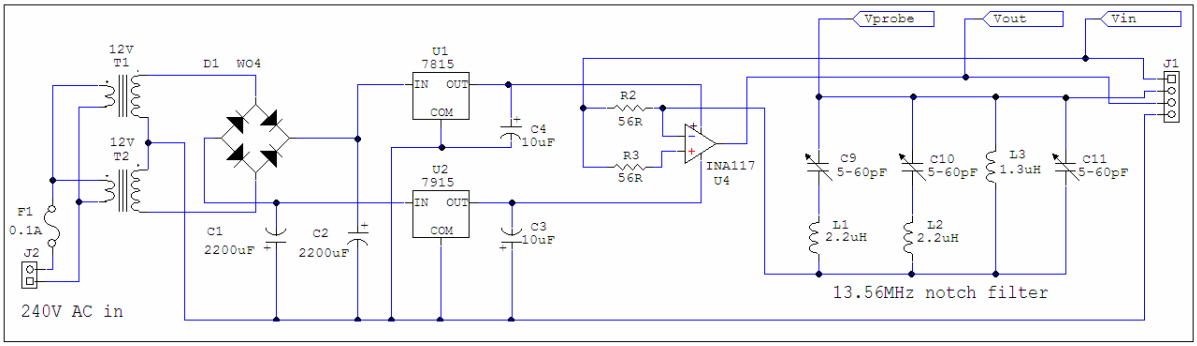

Figure 74 Circuit diagram of the difference amplifier [13.56 MHz notch filter circuit from Wendt 2001 [238]]. The notch filter blocked the 13.56MHz RF that was used to produce the plasma as well as the second and third harmonics.

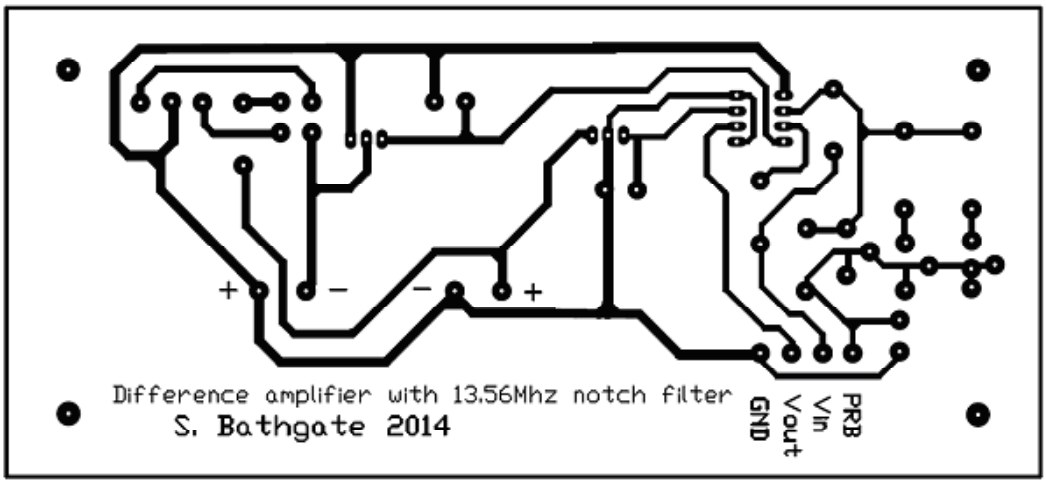

Figure 75 PCB layout of difference amplifier bottom layer

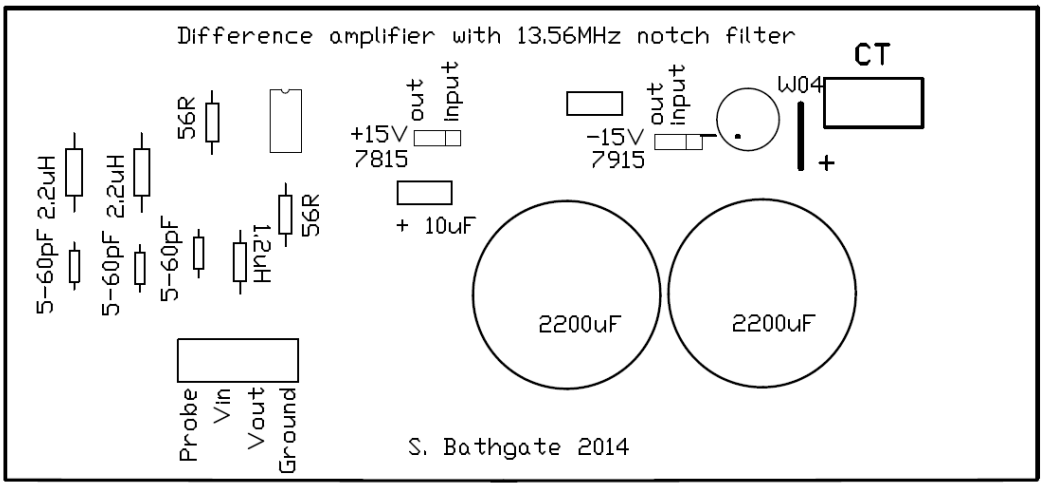

Figure 76 PCB layout of difference amplifier with 13.56MHz notch filter top overlay showing component locations.

10.5 Pulsed power supply

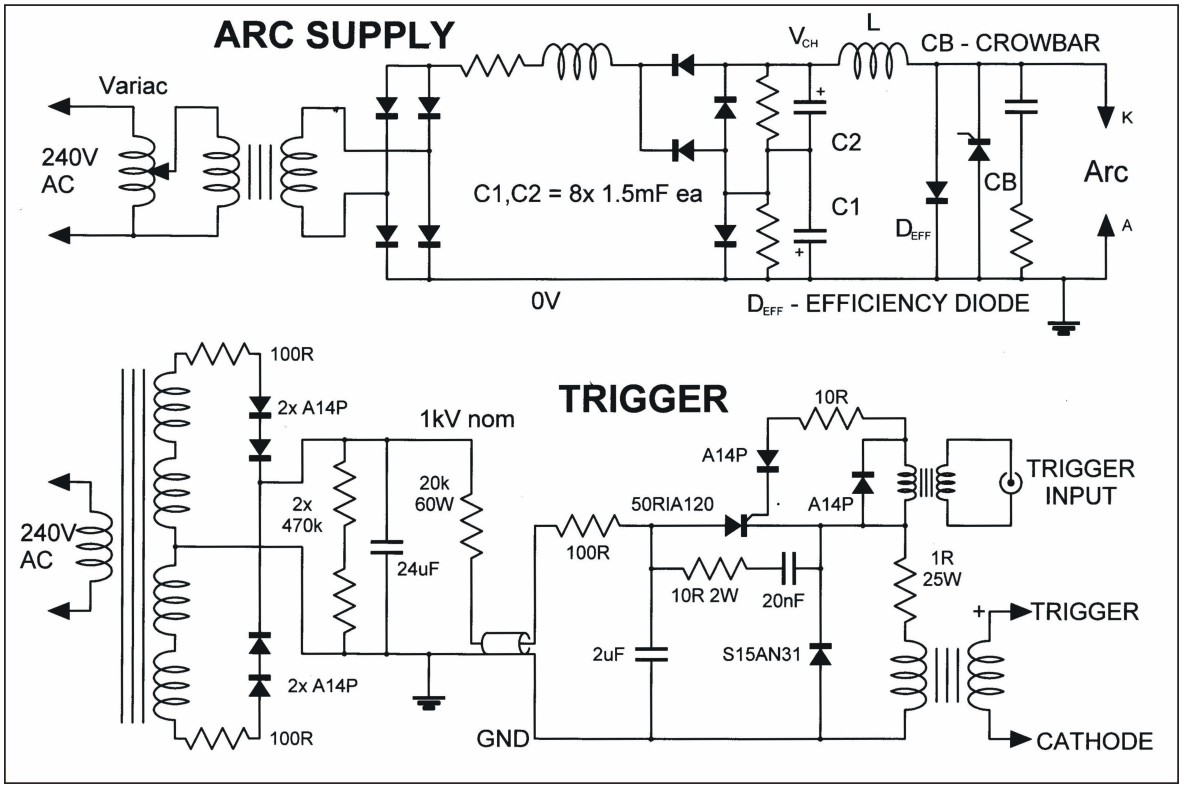

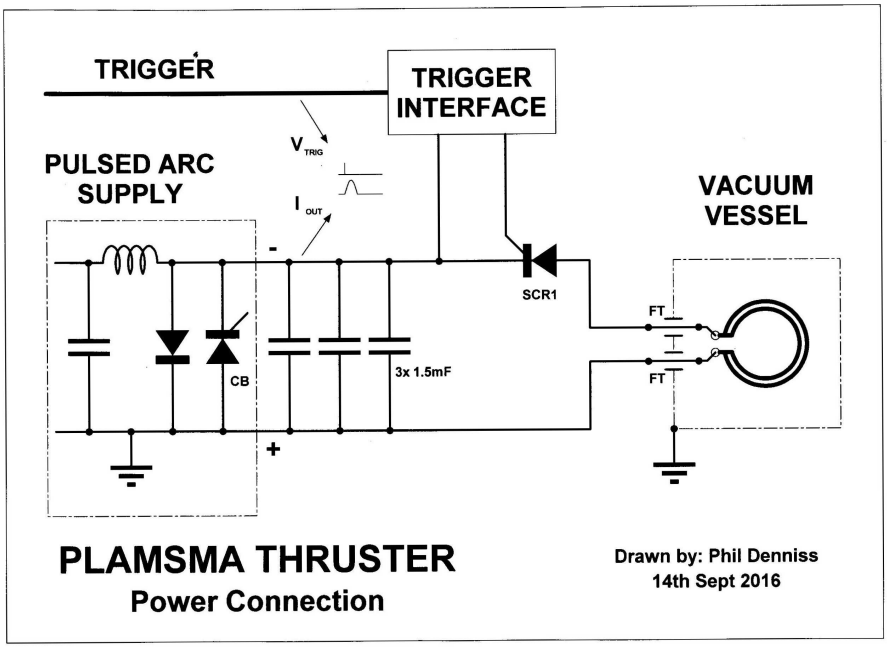

Figure 77 Pulses from the isolating interface (fig. 66) to the trigger interface caused the SCR to connect the charged capacitors connected to the pulsed arc supply to the thruster in the vacuum vessel.

10.6 Retarding field energy analyzer

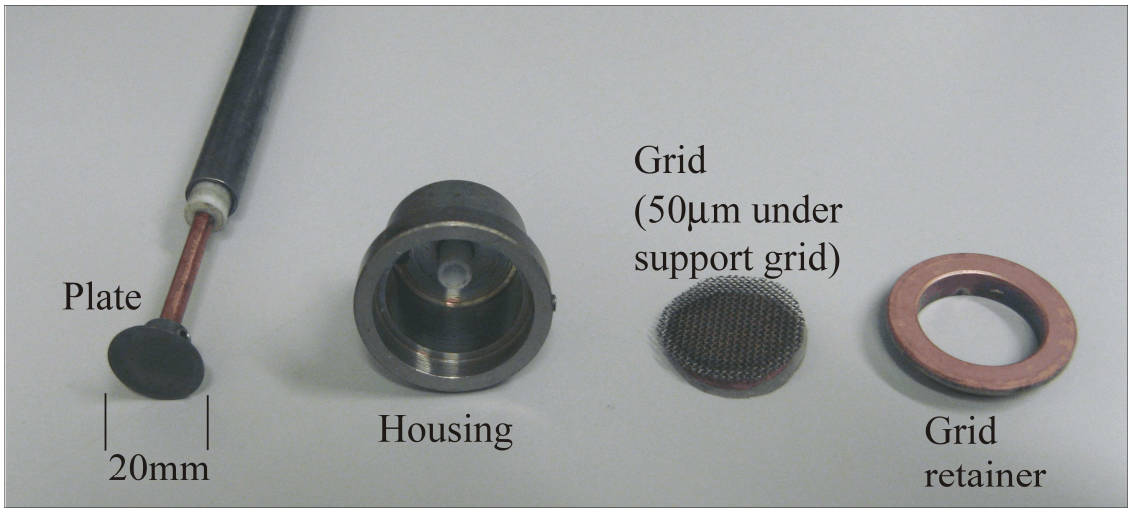

Figure 78 Components of the Retarding Field Energy Analyzer (RFEA) built for this project. With the exception of the plate (mild steel) and its mounting rod (copper), all metallic parts were made from stainless steel. The insulators were made from Teflon. The grid was in contact with and at the same potential as the housing which was connected to an external supply through a lead attached to the back of the housing. The copper on the grid retainer was the result of using the RFEA to measure the energy of copper ions in HiPIMS experiments. The housing was insulated from the plasma with a Teflon cover when in use.

10.7 13.56MHz matching network

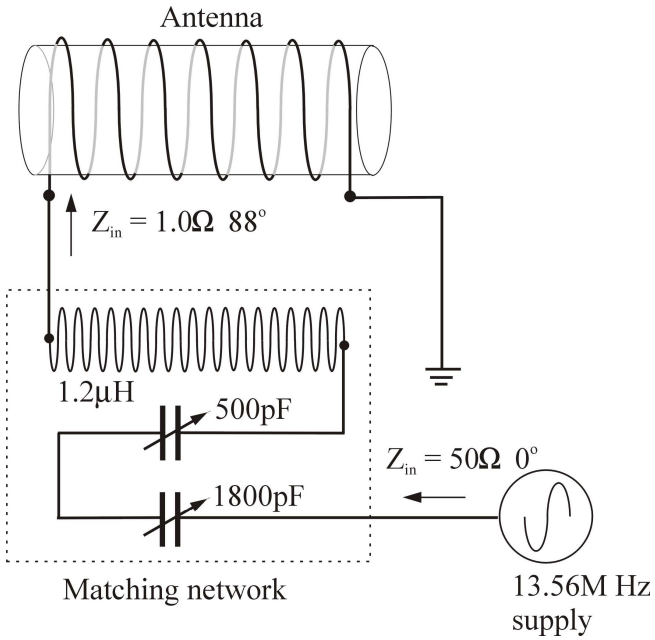

Figure 79 A matching network was constructed to match the low impedance of the plasma chamber antenna to the characteristic impedance of the 50Ω transmission line that connected the antenna to the 13.56MHz Henry Radio power supply.

10.8 Digital filters

Ion current data was filtered with a finite impulse response filter (FIR filter) programmed in Visual Basic.

Finite impulse response filters are a commonly implemented digital filter that is easily programmed. Such filters produce an output that is the sum of delayed samples, each multiplied by a weight that controls the characteristic of the filter. In this study, a Hamming window was used since it gives a smoother roll off at the cut-off frequency and a greater attenuation in the stop band than a simpler rectangular window. It has better selectivity for large signals [Papoulis 1984 [239]] (fig. 80).

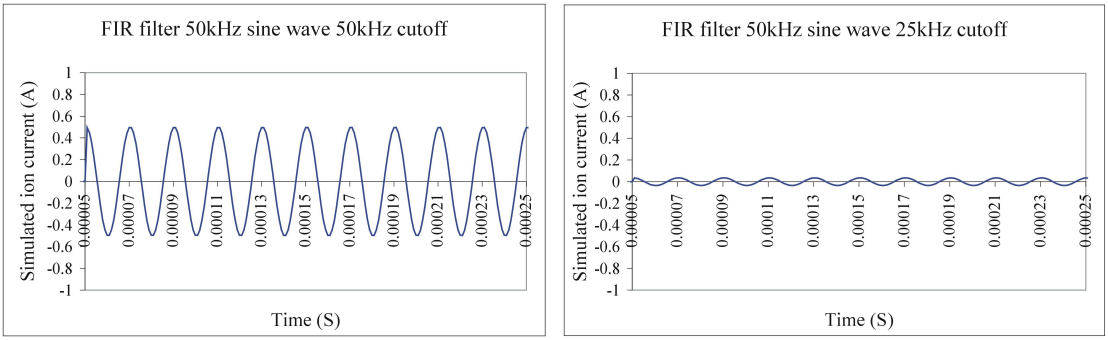

Figure 80 Sine wave tests of a low pass finite impulse response filter. A digitized 50kHz sine wave of 2500 samples with a sample frequency of 1.0 Mhz was filtered with a FIR filter of order 50, firstly with a cut off frequency of 50kHz and then with a cut off frequency of 25kHz. The attenuation of the sine wave was 23dB per octave. The same FIR filter with an order of 500 was used to filter the measurements in the magnetic reconnection experiments.

10.9 Test of measurement system accuracy.

The measurement system was tested by replacing the probe with a resistor of known value and then running a simulated plasma density and electron temperature experiment. The expected value of the current was calculated and plotted against that recorded by the oscilloscope and processed by the Labview program. The difference between the expected and measured values was experimentally insignificant (fig. 81).

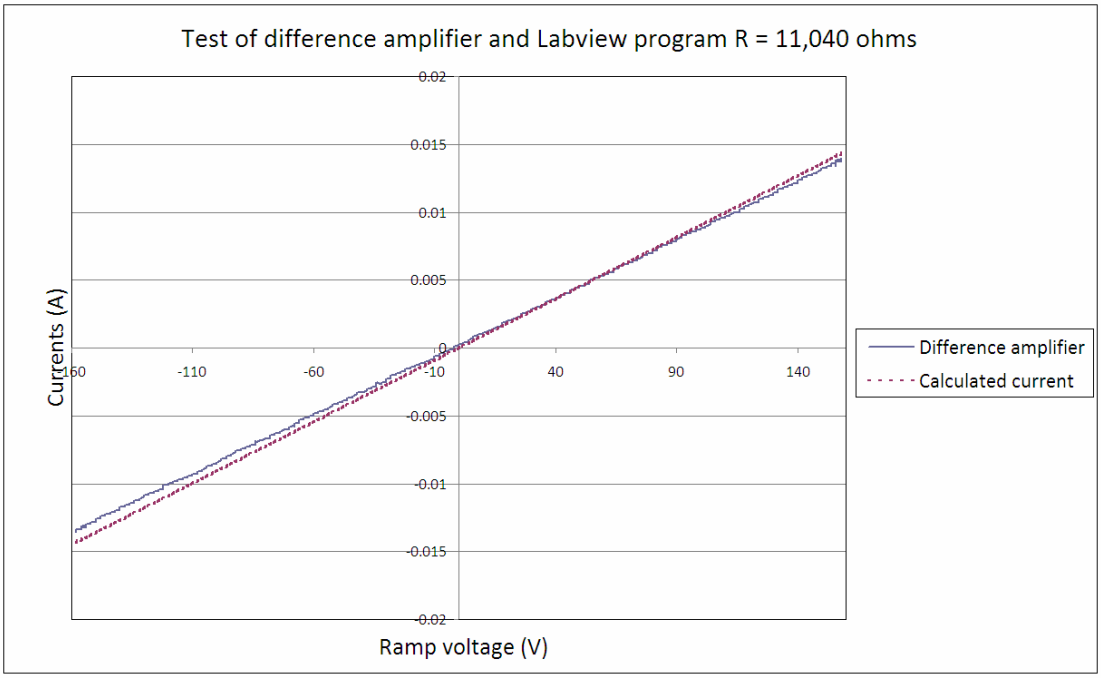

Figure 81 Test of the fidelity of the experimental system using a 11,040 ohm resistor in place of the Langmuir probe. The measured and calculated currents were very close to the same values indicating that there were no large systematic errors in the measurement system that included a difference amplifier, digital oscilloscope and Labview program that scaled the current data and stored it as a text file that was then plotted as an Excel chart.

11 Computer programs

11.1 Labview program for controlling reconnection experiments

Figure 82 Front panel of the Labview virtual instrument used to control the magnetic reconnection experiment. Shown are four charts, the two on the left display the immediate measurements of pulse current and ion current, the two on the right display the average of successive measurements of pulse current and ion current. Controls on the left set the minimum threshold for recording an ion current, controls in the center run and stop experiments, controls on the right set the number of pulses for each experiment and record measurements.

The program was written as a state machine with the following states:

1. Standby. This state was used to set up the number of pulses for an experiment and the minimum value for an acceptable ion current.
2. Get data. This state sent set up data to the Tektronix oscilloscope through an IEEE488 connection. It then sent trigger pulses to the capacitor bank to initiate a current pulse in the thruster tubes. The interface box (fig. 65) isolated the computer and the high voltage circuit. On completion of the preset number of samples it read the accumulated data from the oscilloscope and displayed it as the immediate data (left

chart) and added the measurement to the averaged data (right chart). A complex routine for communicating with the Tektronix oscilloscope was a subroutine of this state.

3. Save data. This state wrote the averaged data to a text file that could be later read and displayed as an Excel chart.

The program was written in Labview as a virtual instrument that used embedded functions from the Labview menus.

11.2 HiPIMS data analysis

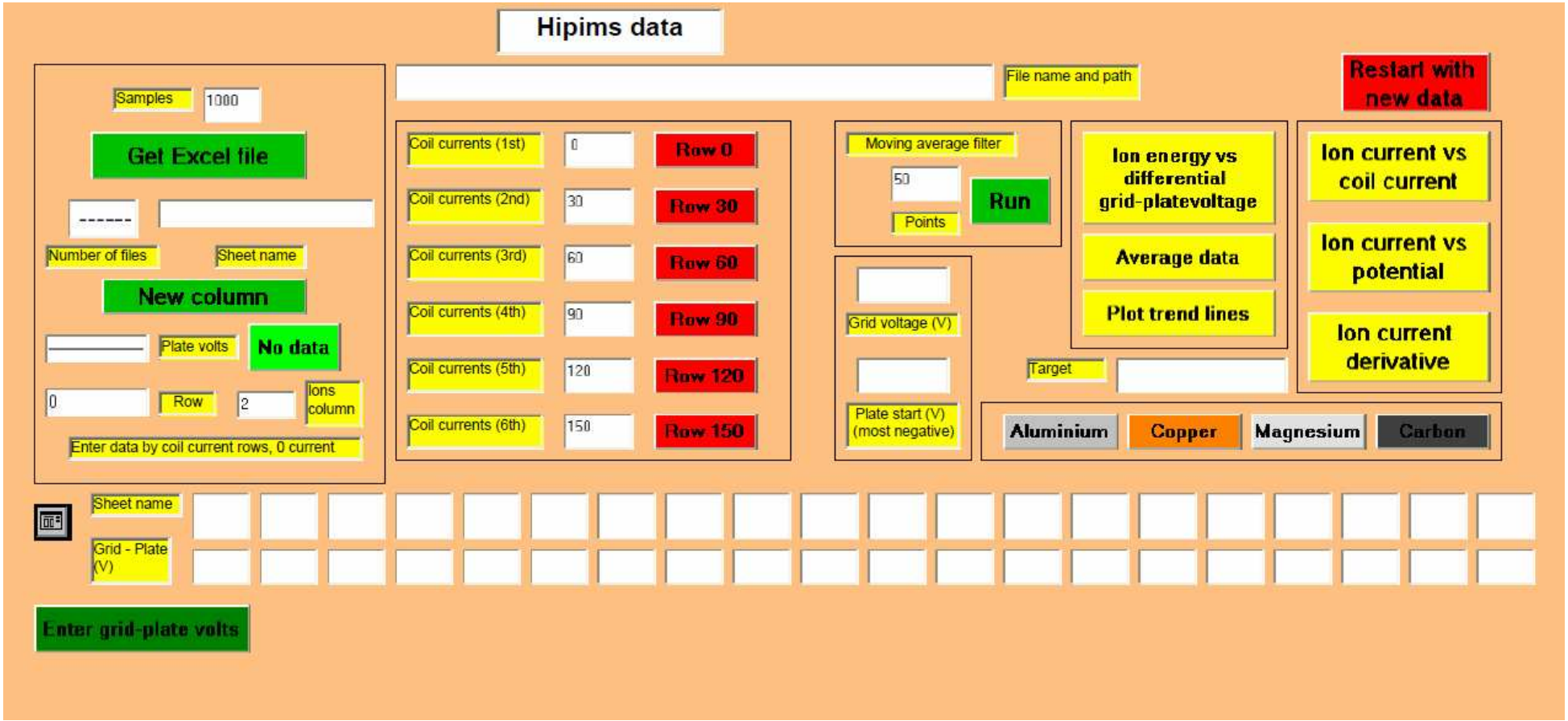

Figure 83 Front panel of aVisual Basic program written to analyze results from HiPIMS measurements. The program first compiles data from Excel files produced during an experiment into an array containing data from separate measurements. That array is then processed by a finite impulse response filter before being further manipulated for instance as a display of ion currents as a function of grid – plate voltage differences or as ion energy distribution functions. The processed data is then transferred to an Excel spreadsheet for plotting.

12 Nomenclature

$\mathbf{A}$	Magnetic vector potential
A_n	Magnetic nozzle area
$\mathbf{B}$	Magnetic flux density
B_{axial}	Axial magnetic flux density
B_θ	Azimuthal magnetic flux density
$\mathrm{B_m}$	Magnetic mirror flux density
B_r	Radial magnetic flux density
B_ω	Rotating magnetic flux density
B_z	Axial magnetic flux density
δ_s	Resistive skin depth
ΔL	Change in circuit inductance
$\Delta\mathbf{r}(t)$	Electric field oscillating component
Δt	Orbital manoeuvre time
Δv	Velocity increment
e	Electron charge
$\mathbf{e}_B$	Magnetic field unit vector
$\mathbf{E}$	Electric field strength
$\mathbf{E}_0(\mathbf{r})$	Electric field amplitude
E_{max}	Maximum amplitude of an accelerating wave field
E_{p0}	Amplitude of REF penetration into a uniform magnetized plasma
E_θ	Electric field azimuthal component
ε_a	Angular frequency ratio
ε_0	Permittivity of free space
η_p	Plasma resistivity
η_P	Power efficiency
η_t	Thrust efficiency
F_t	Thrust
$\mathbf{F}_{pf}$	Non-linear ponderomotive force
g_0	Acceleration due to Earth's gravity

i_A	Arc discharge current
$\mathrm{I_p}$	Plasma current
I_{sp}	Specific impulse
$\mathbf{I}_H$	Hall current
J	Mission difficulty parameter
$\mathbf{j}$	Current density
j_z	Axial current
j_θ	Azimuthal current density
$\mathbf{j}\times\mathbf{B}$	Hall current
k_B	Boltzmann's constant
L_A	Length of an accelerating region
L_0	Initial circuit inductance
λ_P	Plasma wavelength
m_e	Electron mass
m_f	Final mass
m_i	Initial mass
m_{ion}	Ion mass
$\dot{m}_p$	Rate of expulsion of propellant
m_{pl}	Payload mass
M	Mach number
μ	Dimensionless parameter
μ_m	Magnetic moment
μ_r	Relative permeability
μ_0	Magnetic permeability of free space
n_0	Initial electron number density
n_e	Electron number density
ν_{ei}	Electron – ion collision frequency
P_L	Laser power
P_s	Propulsion system power
q	Charge
r_p	Plasma radius

r	Radial position
r_m	Radius of the magnetic coil
R_{coil}	Axial coil radius
R_G	Gyration radius
R_L	Larmor radius
ρ_n	Net charge density
r_L	Radius of a laser beam spot
T_e	Electron temperature
V_B	Acceleration voltage
V_0	Initial REF voltage
$\mathbf{v}$	Ion velocity
v_e	Exhaust velocity
v_p	Propagation velocity
$v_\perp$	Plasma perpendicular velocity
ω_{ce}	Electron cyclotron resonant frequency
ω_{ci}	Ion cyclotron frequency
ω_f	Electromagnetic field frequency
ω_{pe0}	Initial electron plasma frequency
ω_{REF}	Rotating electric field frequency
ω_{RMF}	Rotating magnetic field frequency
Ω_{ni}	Ion cyclotron frequency

13 References

[1] J. Needham, Ho Ping-Yu, Lu Gwei-Djen and Wang Ling, *"Science and Civilization in China", Vol. 5, Chemistry and Chemical Technology; The Gunpowder Epic, Cambridge University Press,* 1986

[2] K. Tsiolkovsky, "Exploration of Space Using Reactive Devices", *Nauchnoye obzorniye (Scientific review) No.5,* 1903

[3] J. J. Thomson, *"Cathode rays", Philosophical Magazine, 44, 293,* 1897

[4] E. Y. Choueiri, "A Critical History of Electric Propulsion: The First 50 Years (1906-1956)," Journal of Propulsion and Power, Vol. 20, pp. 193–203, 2004

[5] R. Goddard, "*Report Concerning Further Developments",* Smithsonian Institution Archives, 1920

[6] J. Barnett, *"A review of Soviet plasma engine development", 21st International Electric Propulsion Conference, International Electric Propulsion Conference , AIAA-90-2600,* 1990

7 H. Oberth, Wege zur Raumschiffahrt, (R. Oldenbourg, München und Berlin 1929)

[8] G. B. Heller, "The Electric Engine as a Propulsion System for the Exploration of Space", *Space Age Astronomy, Proceedings of an international Symposium held August 7-9, 1961 at the California Institute of Technology in conjunction with the 11th General Assembly of the International Astronomical Union (IAU, GA, 11), New York: Academic Press, edited by Deutsch, Armin J.; Klemperer, Wolfgang B., p.288,* 1962

[9] E. Stuhlinger, "Ion Propulsion for Space Flight", *McGraw-Hill Book Company New York* 1964

[10] J. S. Sovey, V.K. Rawlin and M.J. Patterson, *Journal of Propulsion and Power, Vol. 17, No. 3, pp. 517-526,* May-June 2001

[11] M.N. Kazeev, K.N. Kozubskiy and G.A. Popov, *"Victor Khrabrov – Pioneer of the First Space Electric Propulsion System Development and Space Tests", IEPC-2009-235,* 2009

[12] M. G. Marcucci and J. E. Polk, *Rev. Sci. Instrum. 71, 1389, doi.org/10.1063/1.1150468*, 2000

[13] J. Brophy, *Space Sci Rev (2011) 163: 251. doi:10.1007/s11214-011-9848-y*, 2011

[14] N. Wallace, P. Jameson, C. Saunders, M. Fehringer, C. Edwards and R. Floberghagen, *IEPC-2011-327,* 2011

[15] D. M. Goebel and I. Katz, *Fundamentals of Electric Propulsion: Ion and Hall Thrusters*, (John Wiley & Sons, 2008

[16] V. Kim, G. Popov, B. Arkhipov, V. Murashko, O. Gorshkov, A. Koroteyev, V. Garkusha, A. Semenkin and S. Tverdokhlebov, *IEPC-01-05, 27th International Electric Propulsion Conference,* 15-19 October, 2001.

[17] O. Gorshkov, A. Koroteev, B. Arkhipov, V. Murashko, N. Anfimov, V. Lukyashenko, V. Kim, and G. Popov, *AIAA-3229, 37th Joint Propulsion Conference and Exhibit, Joint Propulsion Conferences, doi.org/10.2514/6.2001-3229*, 2001

[18] M. Kilter and A. Karlsson, *"Micropropulsion Technologies for the European High-Precision Formation Flying Interferometer DARWIN", Proceedings of the 4th International Spacecraft*

Propulsion Conference (ESA SP-555). Chia Laguna (Cagliari), Sardinia, Italy. Editor: A.Wilson, 2-9 June, 2004

[19] E. Ahedo, *Plasma Phys. Control. Fusion 53 124037*, 2011

[20] S. A. Cohen, X. Sun, N. M. Ferraro, E. E. Scime, M. Miah, S. Stange, N. S. Siefert and R. F. Boivin, *IEEE Transactions on Plasma Science, VOL. 34, NO. 3,* June 2006

[21] T. E. Markusic, K. A. Polzin, E. Y. Choueiri, M. Keidar, I. D. Boyd, and N. Lepsetz, "*Ablative Z-Pinch Pulsed Plasma Thruster", Journal of Propulsion and Power, Vol. 21, No. 3 (2005), pp. 392-400. (doi.org/10.2514/1.4362)* 2005

[22] D.C. Rapp, *NASA contractor report 185279, AIAA-90-1968,* July 1990

[23] M. J. Patterson, L. Pinero and J. S. Sovey, *AIAA 2009-4819, 45th AIAA/ASME/SAE/ASEE Joint Propulsion Conference & Exhibit,* 2 - 5 August 2009

[24] A. Smirnov, Y. Raitses, and N. J. Fisch, *Journal of Applied Physics, Vol. 92, No. 10, pp. 5673-5679,* 15 November 2002

[25] G. Krulle, M. Auweter-Kurtz, and A. Sasoh, doi.org/10.2514/2.5338, *Journal of Propulsion and Power, Vol. 14, No. 5, p. 754,* 1998

[26] H. Bohrk and M. Auweter-Kurtz, *57th International Astronautical Congress, IAC-06-C4.P.4.06, doi.org/10.2514/6.IAC-06-C4.P.4.06,* 2-6 October 2006

[27] P. Neumann, M. Bilek, R. Tarrant and. McKenzie, *Plasma Sources Sci. Technol. 18, 045005 (8pp),* 2009

[28] O. V. Batishchev, IEEE *Transactions on Plasma Science, Vol. 37, No. 8, pp. 1563 -1571,* August 2009

[29] K. A. Polzin and J. P. Reneau, *IEEE Transactions on Plasma Science, Vol. 37, No. 2, pp. 359-364,* February 2009

[30] B. W. Longmier, L. D. Cassady, M. G. Ballenger, M. D. Carter, F. R. Chang-Díaz, T. W. Glover, A. V. Ilin, G. E. McCaskill, C. S. Olsen, J. P. Squire and E. A. Bering III, *Journal of Propulsion and Power Vol. 27, No. 4, pp. 915-920, DOI: 10.2514/1.54932,* July–August 2011

[31] J. Jarrige, P. Q. Elias, F. Cannat and D. Packan, *IEPC-2013-420, 33rd International Electric Propulsion Conference,* October 6-10, 2013

[32] J. Slough, D. Kirtley and T. Weber, *IEPC-2009-265, 31st International Electric Propulsion Conference,* September 20-24, 2009

[33] M. M. Rathore, *Thermal Engineering,* (Tata McGraw-Hill Education 2010)

[34] G. P. Sutton and O. Biblarz, *Rocket Propulsion Elements,* (John Wiley and Sons New York 2001)

[35] A. V. Arefiev and B. N. Breizman *Phys. Plasmas 11, 2942* (2004)

[36] J. Gilland, D. Fiehler and V. J. Lyons, *Electric Propulsion Concepts Enabled by High Power Systems for Space Exploration, in proceedings: Second International Energy Conversion Engineering Conference Providence, Rhode Island,* (August 16–19, 2004)

[37] B.H Foing, G.D. Racca, A. Marini, D.J. Heather, D. Koschny, M. Grande, J. Huovelin, H.U. Keller, A. Nathues, J.L. Josset, A. Malkki, W. Schmidt, G. Noci, R. Birkl, L.Iess, Z. Sodnik, P. McManamon, *Adv.Space Res. Vol. 31, Issue 11, June 2003, p2323* (2003)

[38] M. D. Rayman, P. Varghese, D. H. Lehman and L. L. Livesay, *Acta Astronaut. Vol. 47, Issues 2–9, July–November 2000, p 475* (2000)

[39] M. Yoshikawa, A. Fujiwara, and J. Kawaguchi, *Hayabusa and its adventure around the tiny asteroid Itokawa, (Highlights of Astronomy, Volume 14 IAU XXVI General Assembly, 14-25 August 2006 K.A. van der Hucht, ed.* (2006)

[40] J. Brophy, M. Etters, J. Gates, C. Garner, M. Klatte, C. Lo, M. Marcucci, S. Mikes, G. Pixler and B. Nakazono, *AIAA Paper 2006-4319* (2006)

[41] S. W. Benson, L. A. Arrington, W. A. Hoskins and N. J. Meckel, *AIAA Paper 1999-2276,* 1999

[42] V. P. Dawson and M. D. Bowles, *Taming liquid hydrogen : the Centaur upper stage rocket, 1958-2002, NASA-SP-2004-4230,* 2004

[43] W. G. Melbourne, *Jet Propulsion Laboratory Technical Report No. 32-68,* 1961

[44] T. N. Edelbaum, *Optimal space trajectories*, (Analytical Mechanics Associates, Inc. Jerocho, New York [Sponsored by Air Force Office of Scientific Research]), 1969

[45] W. E. Moeckel, *NASA Technical Note TN D-6968,* 1972

[46] T. A. Ward, *Aerospace Propulsion Systems*, (John Wiley and Sons (Asia)), 2010

[47] G. Woodcock, NASA. *Langley Research Center, Space Transportation Materials and Structures Technology Workshop. Volume 2: Proceedings; p 93-104* , 1995

[48] K. de Grys, A. Mathers, B. Welander, *AIAA 2010-6698, 46th AIAA/ASME/SAE/ASEE Joint Propulsion Conference & Exhibit*, 25 - 28 July 2010

[49] O.A. Gorshkov, V.N. Shutov, K.N. Kozubsky, V.G. Ostrovsky and V.A. Obukhov, *IEPC-2007-136, 30th International Electric Propulsion Conference,* September 17-20, 2007

[50] J. Gilland, D. Fiehler and V. J. Lyons, *Electric Propulsion Concepts Enabled by High Power Systems for Space Exploration, in proceedings: Second International Energy Conversion Engineering Conference,* August 16–19, 2004

[51] B.H. Foing, G.D. Racca, A. Marini, D.J. Heather, D. Koschny, M. Grande, J. Huovelin, H.U. Keller, A. Nathues, J.L. Josset, A. Malkki, W. Schmidt, G. Noci, R. Birkl, L.Iess, Z. Sodnik, P. McManamon, *Advances in Space Research Vol. 31, Issue 11, June 2003, p2323,* 2003

[52] M. Yoshikawa, A. Fujiwara, and J. Kawaguchi, *Hayabusa and its adventure around the tiny asteroid Itokawa, (Highlights of Astronomy, Volume 14 IAU XXVI General Assembly, 14-25 August 2006 K.A. van der Hucht, ed.,* 2006

[53] S. W. Benson, L. A. Arrington, W. A. Hoskins and N. J. Meckel, *AIAA Paper 1999-2276,* 1999

[54] V. P. Dawson and M. D. Bowles, *Taming liquid hydrogen : the Centaur upper stage rocket, 1958-2002, NASA-SP-2004-4230,* 2004

[55] D.L. Brown, B.E. Beal and J.M. Haas, *"Air Force Research Laboratory High Power Electric Propulsion Technology Development," 2010 IEEE Aerospace Conference*, March 2010

[56] A. Fruchtman, *IEEE Transactions on Plasma Science, Vol. 36, No. 2,* April 2008

[57] M. R. LaPointe, *AIAA Paper 2000-3365*, 2000

[58] A. V. Arefiev and B. N. Breizman, *Physics of Plasmas, 15, 042109*, 2008

[59] S. A. Andersen, V. O. Jensen, P. Nielsen and N. D'Angelo, *Physics Letters, Volume 27A, number 8*, 9 September 1968

[60] K. Takahashi, C. Charles, R. Boswell and A. Ando, *Plasma Sources Sci. T. 23* (2014)

[61] U. S. Inan and M. Gołkowski, *Principles of Plasma Physics for Engineers and Scientists*, (Cambridge University Press 2010)

[62] F. H. Ebersohn, S. S. Girimaji, D. Staack, J. V. Shebalin, B. Longmier and C. Olsen, *Proceedings AIAA 2012-4274, 48th AIAA/ASME/SAE/ASEE Joint Propulsion Conference & Exhibit 30 July - 01 August 2012*, 2012

[63] M.M. Martinez, *PhD thesis, Universidad Politecnica de Madrid*, 2013

[64] F. H. Ebersohn, B. W. Longmier, J.P. Sheehan, J. V. Shebalin and S. S. Girimaji, *IEPC-2013-334* (2013)

[65] N. Oudini, G. J. M. Hagelaar, J. P. Boeuf and L. Garrrigues, *J. Appl. Phys., 109, 073310* (2011)

[66] I. R. Jones, *Physics of Plasmas Vol. 6, No. 5 p1950,* May 1999

[67] J.T. Slough and K.E. Miller, *Physics of plasmas, Vol. 7, No. 5*, 2000

[68] A. L. Hoffman, H. Y. Guo, K. E. Miller and R. D. Milroy, *doi.org/10.1063/1.2162052, Phys. Plasmas 13, 012507*, 2006

[69] S. Shinohara, H. Nishida, T. Tanikawa, T. Hada, I. Funaki and K. P. Shamrai, *IEEE Transactions on Plasma Science, Vol.42, No.5,* May 2014

[70] K. Toki, S. Shinohara, T. Tanikawa, I. Funaki and K. P. Shamrai, *IEPC 03-0168*, 2003

[71] T. Nakamura, K. Yokoi, H. Nishida, T. Matsuoka, I. Funaki, S. Shinohara, T. Tanikawa, T Hada, T. Motomura, K. P. Shamrai and T. S. Rudenko, *Trans. JSASS Aerospace Tech. Japan Vol. 10, No. ists28*, 2012

[72] G. D. Emsellem and S. Larigaldie, *IEPC-2007-240, 30th International Electric Propulsion Conference,* September 17-20, 2007

[73] F. Otsuka, T. Hada, S. Shinohara, T. Tanikawa and T. Matsuoka, *Plasma and Fusion Research: Regular Articles Volume 8, 1406012*, 2013

[74] S. M. Hooker, *Nature Photonics 7, 775–782 (2013) doi:10.1038/nphoton.2013.234*, 2013

[75] G. J. Williams Jr. and J. H. Gilland, *AIP Conf. Proc. 1103, 175*, 2009

[76] H. Alfven and C. G. Falthammar, *Cosmical Electrodynamics, 2nd Ed., p. 162, Oxford University Press, London*, 1963.

[77] L.P. Block, *Astrophysics and Space Science, 55, pp 59-83*, 1978

[78] C. Charles and R. Boswell, *Applied Physics Letters, Vol. 82, No. 9, pp. 1356-1358,* 3rd March 2003

[79] Yung-Ta Sung, Yan Li, and J. E. Scharer, Physics of Plasmas, 23, 092113, 2016

[80] A. Fruchtman, *Physical Review Letters, 96, 065002*, 2006

[81] A. Fruchtmann and G. Makrinch *IEPC – 2009 – 197*, 2009

[82] K. Takahashi, T. Lafleur, C. Charles, P. Alexander, R. W. Boswell, *Physical Review Letters, 107, 235001,* 2011

[83] T. Ziemba, J. Carscadden and J. Slough, *"High Power Helicon Thruster", AIAA 2005-4119, 41st AIAA/ASME/SAE/ASEE Joint Propulsion Conference and Exhibit*, 10-13 July 2005

[84] F.F. Chen, *Physics of Plasmas, 13, 034502,* 2006

[85] E. Ahedo and M. M. Sanchez, *AIAA 2008-5005, 44th AIAA/ASME/SAE/ASEE Joint Propulsion Conference & Exhibit,* 21 - 23 July 2008

[86] D. Benisti, A. K. Ram, and A. Bers, *Physics of Plasmas, Vol. 5, No. 9, pp. 3224 - 3232,* September, 1998

[87] P. J. Vail and E. Y. Choueiri, *IEPC-2013-204*, 2013

[88] B. Jorns and E.Y. Choueiri, *AIAA-2012-4194*, 2012

[89] B. Jorns and E. Y. Choueiri, *IEPC-2009-199, 31st International Electric Propulsion Conference, University of Michigan,* September 20–24, 2009

[90] R.G. Jahn,*"Physics of Electric Propulsion", Dover Publications Inc., Mineola, New York*, 1996

[91] J. P. Squire, M. D. Carter, F. R. Chang Diaz, L. Dean, M. Giambusso, J. Castro and J. Del Valle, *AIAA 2016-4950, doi.org/10.2514/6.2016-4950, 52nd AIAA/SAE/ASEE Joint Propulsion Conference,* 2016

[92] J. Slough, D. Kirtley and T Weber, *IEPC-2009-265*, 2009

[93] D. Kirtley, A. Pancotti, J. Slough, and C. Pihl, *AIAA Paper 2012-4071,* 2012)

[94] A. P. Pancotti, J. M. Little, J. S. Neuhoff, B. M. Cornella, D. E. Kirtley, and J. T. Slough, *IEPC-2015-67 ／ISTS-2015-b-67 Joint Conference of 30th ISTS, 34th IEPC and 6th NSAT,*, July 4 – 10, 2015

[95] D. Kirtley, J. Slough, C. Pihl. E. Meier and R. Milroy, *IEPC-2011-015,* 2011)

[96] J. Waldock, D. Kirtley and J. Slough, *IEPC-2013-376*, 2013

[97] K. Miller, J. Slough and A. Hoffman, *An overview of the star thrust experiment, in AIP Conf. Proc. 420, 1352,* 1998

[98] D. Kuwahara, S. Shinohara, T. Ishii, S. Otsuka, T. Nakagawa, K. Kishi, M. Sakata, E. Tanaka, H. Iwaya, K. Takizawa, Y. Tanida, T. Naito, K. Yano1, T. Nakamura, S. Ito and H. Nishida, *IEPC-2015-386/ISTS-2015-b-386, 34th International Electric Propulsion Conference and 6th Nano-satellite Symposium*, July 4 – 10, 2015

[99] T. Furuawa, K. Takizawa, D. Kuwahara and S. Shinohara, *"Study on Electromagnetic Plasma Acceleration Using Rotating Magnetic Field Scheme", International Journal of Physical and Mathematical Sciences Vol. 3, No. 11,* 2016

[100] T. Matsuoka, I. Funaki, T. S. Rudenko, K. P. Shamrai, S. Satoh, T. Fujino, T. Nakamura, K. Yokoi, H. Nishida, S. Shinohara and T. Hada, *IEPC-2011-079, 32nd International Electric Propulsion Conference,* September 11 – 15, 2011

[101] T. Nakamura, K. Yokoi, H. Nishida, T. Matsuoka, I. Funaki, S. Shinohara, T. Tanikawa, T. Hada, T. Motomura, K. P. Shamrai and T. S. Rudenko, JSASS Aerospace Tech. Japan, Vol. 10, No. ists28, pp. Tb_17-Tb_23, 2012

[102] K.A. Polzin, *Journal of Propulsion and Power, Vol 27, No. 3, pp. 513-531,* May-June 2011

[103] C. L. Dailey and R. H. Lovberg, *The PIT Mk V Pulsed Inductive Thruster, (NASA Contractor Report 191155 Prepared for Lewis Research Centre Under Contract NAS 1-19291)*, 1993

[104] R. H. Lovberg and C.L. Dailey, *Paper 81-0708, AIAA/JSASS/DGLR, 15th International Electric Propulsion Conference,* April 21-23, 1981

[105] A. K. Hallock and K. A. Polzin, *SP-2010-1842709, Space Propulsion 2010,* 3-6 May, 2010

[106] A.K. Martin, *J. Phys. D: Appl. Phys. 49, 025201 (16pp),* 2016

[107] M. S. Feldman and E. Y. Choueiri, *IEPC-2011-220,* 2011

[108] E. Y. Choueiri and K. A. Polzin, *AIAA Paper 2004-3940*, 2004

[109] K. A. Polzin, M. F. Rose and R. Miller, *44th AIAA/ASME/SAE/ASEE Joint Propulsion Conference,* July 21–23, 2008

[110] A.K. Hallock and K.A. Polzin *SP-2010-1842709,* 2010

[111] A. K. Hallock, K.A. Polzin, A. C. Kimberlin and K.A. Perdue, *AIAA Paper 2012-3928*, 2012

[112] A. K. Hallock, A.K. Martin, K.A. Polzin, A.C. Kimberlin and R.H. Eskridge, *JANNAF (Joint Army-Navy-NASA-Air Force)-2013-3070,* (2013)

[113] K.A. Polzin 2012 *Abstract #4344 Concepts and approaches for Mars exploration June 12-14, Lunar and Planetary Institute, Houston, Texas* (2012)

[114] R. Eskridge and A. Martin, "*Progress on the PT-1 Prototype Plasmoid Thruster", AFRL Space Propulsion and Power Workshop,* October 17 - 19, 2007

[115] K. A. Polzin, *Journal of Propulsion and Power Vol. 27, No. 3, May-June 2011, p513,* 2011

[116] C. L. Dailey and R. H. Lovberg, *NASA Contractor Report 191155, Prepared for Lewis Research Center Under Contract NAS 1-19291*, July 1993

[117] A. K. Hallock, A. K. Martin, K. A. Polzin, A. C. Kimberlin, and R. H. Eskridge, *IEEE Transactions on Plasma Science, Vol. 43, No. 1, pp. 433-443*, January 2015

[118] J. N. Navarro-Cavalle, E. Ahedo, M.Merino, V. Gomez, M. Ruiz and J.A. Gonzalez del Amo, *IEPC-2013-285*, 2013

[119] O. Batishchev, *IEEE Transaction on Plasma Science, Vol. 37, pp. 1563-1571*, 2009

[120] D. Pavarin, M. Manente, Y. Guclua, D. Curreli, C. Bettanini, M. Zaccariotto, M. Walker, D. Palmer, J. Carlsson, C. Bramanti et al, *44th AIAA/ASME/SAE/ASEE Joint Propulsion Conference & Exhibit*, (2008)

[121] F. Trezzolani, A. Lucca Fabris, D. Pavarin, A. Selmo, A. I. Tsaglov, A. V. Loyan, O. P. Rubalov and M. Manente, *IEPC-2013-153, 33rd International Electric Propulsion Conference*, October 6–10, 2013

[122] K. Takahashi, T. Laeur, C. Charles, P. Alexander, R. Boswell, M. Perren, R. Laine, S. Pottinger, V. Lappas, T. Harle et al, *Applied Physics Letters, Vol. 98, pp. 141503*, 2011

[123] T. Ziemba, J. Slough and R. Winglee, *AIP Conference Proceedings, Vol. 746, p. 965*, 2005

[124] S. Pottinger, V. Lappas, C. Charles and R. Boswell, *J. Phys. D: Appl. Phys. 44, 235201 (5pp)*, 2011

[125] K. Takahashi, C. Charles, R. Boswell and A. Ando, *Journal of Physics D: Applied Physics, Volume 46, Number 35, 352001 (5pp), doi:10.1088/0022-3727/46/35/352001*,16 August 2013

[126] G. Hairapetiat and R. L. Stenzel, *Phys. Fluids B 3, 899-914*, 1991

[127] C. Charles, *Applied Physics Letters 82, 1356*, 2003

[128] A. L. Fabris and M. A. Cappelli, *IEPC-2013-86, 33rd International Electric Propulsion Conference,The George Washington University*, October 6-10, 2013

[129] L. Heflinger, S. Ridgway and A. Schaffer, doi.org/10.2514/3.3049, *"Transverse traveling wave plasma engine", AIAA Journal, Vol. 3, No. 6, pp. 1028-1033*, 1965

[130] R.W. Palmer and R.E. Jones, "*Experimental Investigation of a Variable-Length Constant Velocity Travelling Magnetic Wave Plasma Accelerator", NASA Technical Note TN D-420*, October 1967

[131] S. Feraboli, A. L. Fabris and M. A. Cappelli, *IEPC-2015-442p ／ISTS-2015-b-442p, Joint Conference of 30th International Symposium on Space Technology and Science, 34th International Electric Propulsion Conference and 6th Nano-satellite Symposium*, July 4–10, 2015

[132] V. Kouznetsova, K. Macáka, J. M. Schneidera, U. Helmersson and I. Petrov, *Surface and Coatings Technology Vol. 122, Issues 2–3, pp. 290–293*, 1999

[133] J. T. Gudmundsson, N. Brenning, D. Lundin and U. Helmersson, *Journal of Vacuum Science & Technology. A. Vacuum, Surfaces, and Films, (30), 030801*, 2012

[134] K. Takahashi, C. Charles, R. Boswell and A. Ando, 2014, *Plasma Sources Sci. Technol. 23 044004*

[135] S. N. Bathgate, R. Ganesan, M. M. M. Bilek and D. R. McKenzie, *"A HiPIMS plasma source with a magnetic nozzle that accelerates ions: application in a thruster", Eur. Phys. J. Appl. Phys. (2016) 76: 30801*, 2016

[136] A. Anders and J. Andersson, 2008, *XXIII-rd Symp. On Discharges and Electrical Insulation in Vacuum – Bucharest*

[137] R. Kukla, T. Krug, R. Ludwig and K. Wilmes, *1990, Vacuum, Vol. 41, Nos. 7-9, pp. 1968-1970*

[138] D. I. Poston, R. J. Kapernick and R. M. Guffee, *AIP Conf. Proc. 608, 578* (2002)

[139] J. Russell and R. Cohn, *Safe Affordable Fission Engine*, (Book On Demand 2012)

[140] G. Rinehart, *Prog. Nucl. Energ., 39,(3) pp. 305-319* (2001)

[141] J. Brophy, R. Gershman, N. Strange, D. Landau, R. G. Merrill and T. Kerslake, *AIAA Paper 2011-5514* (2011)

[142] J. W. Dankanich and K. A. Polzin, *"Performance scaling of inductive pulsed plasma thrusters with coil angle and pulse rate", AIAA Paper 2008-4517,* 2008

[143] K. de Grys, B. Welander, J. Dimicco, S. Wenzel, B. Kay, V. Khayms and J. Paisley, *AIAA 2005-3682* (2005)

[144] O. G. Semyonov, *Acta Astronaut., 99, 52–70,* 2014

[145] S.W. Hawking and G. F. R. Ellis, *Astrophys. J., vol. 152, p.25,* 1968

[146] R.B. Harty, W.D. Otting, and C.T. Kudija, *IEEE AES Systems Magazine pp. 28-32,* January 1994

[147] J. L. Rovey and A. D. Gallimore, *Journal of Propulsion and Power, Vol. 24, No. 6, pp. 1361-1368,* November–December 2008

[148] J. Brophy, M. Etters, J. Gates, C. Garner, M. Klatte, C. Lo, M. Marcucci, S. Mikes, G. Pixler and B. Nakazono, *AIAA Paper 2006-4319*, 2006

[149] J. R. Brophy, I. Katz, J. E. Polk and J. R. Anderson *AIAA Paper 2002-4261,* 2002

[150] O. B. Duchemin, J. R. Brophy, C. E. Garner, P. K. Ray, V. Shutthanandan and M. A. Mantenieks, *(JPL Technical Report 97-1081),* 1997

[151] J.S. Meserole, *Journal of Propulsion and Power Vol.17, No. 1, p12,* January-February 2001

[152] S. Y. Cheng and M. Martinez-Sanchez *IEPC-2007-250,* 2007

[153] D. M. Goebel, R. R. Hofer, I. G. Mikellides, I. Katz, J. E. Polk and B. Dotson *IEPC-2013-276,* 2013

[154] R. R. Hofer, B. A. Jorns, J. E. Polk, I. G. Mikellides and J. S. Snyder *IEPC-2013-033,* 2013

[155] Sankaran, L. Cassady, A. D. Kodys and E. Y. Choueiri, *The Annals of the New York Academy of Science, Vol. 1017, p450,* May 2004.

[156] R. P. Hoyt, *IEPC-2005-230,* 2005

[157] E.Y. Choueiri and J.K. Ziemer, *Quasi-Steady Magnetoplasmadynamic Thruster Performance Database, Journal of Propulsion and Power, Vol. 17 No. 4.*, Sept/October 2001

[158] A. Boxberger, P. Bambach, G. Herdrich, and S. Fasoulas *AIAA paper 2012-4012*, 2012

[159] J. Cassibry, R. Cortez, M. Stanic, A. Watts, W. SeidlerII, R. Adams, G. Statham, and L. Fabisinski. *"Case and Development Path for Fusion Propulsion", doi.org/10.2514/1.A32782, Journal of Spacecraft and Rockets, Vol. 52, No. 2 (2015), pp. 595-612,* 2015

[160] M. Martinez-Sanchez and J. E. Pollard, 1998, *Journal of Propulsion and Power, Vol. 14, No. 5*, (September –October 1998)

[161] T.E. Markusic_, K.A. Polzin, E.Y. Choueiri, M. Keidar, I. D. Boyd and N. Lepsetz, 2005, *Journal of Propulsion and Power, Vol. 21, No. 3,* (May-June 2005)

[162] V. Kouznetsova, K. Macáka, J. M. Schneidera, U. Helmersson and I. Petrov, 1999, *Surface and Coatings Technology Vol. 122, Issues 2–3, pp. 290–293*

[163] J. T. Gudmundsson, N. Brenning, D. Lundin and U. Helmersson, 2012, *Journal of Vacuum Science & Technology. A. Vacuum, Surfaces, and Films, (30), 030801*

[164] K. Takahashi, C. Charles, R. Boswell and A. Ando, 2014, *Plasma Sources Sci. Technol. 23 044004*

[165] R. Winglee, T. Ziemba, L. Giersch, J. Prager, J. Carscadden and B.R. Robertson, 2007, *Physics of Plasmas, 14,063502*

[166] J. Madocks, *Magnetron plasma source patent US 7038389 B2,* (2006)

[167] J. Bohlmark, M. Östbye, M. Lattemann, H. Ljungcrantz, T. Rosell, and U.Helmersson, *Thin Solid Films, (515), 4, pp. 1928-1931* (2006)

[168] A. Anders and J. Andersson, 2008, *XXIII-rd Symp. On Discharges and Electrical Insulation in Vacuum – Bucharest*

[169] R. Kukla, T. Krug, R. Ludwig and K. Wilmes, *1990, Vacuum, Vol. 41, Nos. 7-9, pp. 1968-1970*

[170] J. A. Simpson, 1961, *Rev. Sci. Instrum., Vol. 32, No. 12, 1283,* (December 1961)

[171] D. Grondona, H. Kelly and A. Marquez, *Appl. Phys. Lett., Vol. 79, No. 1, pp. 317-319* (2001)

[172] C. Rusteberg, M. Lindmayer, B. Juttner and H. Pursch, *IEEE T. Plasma Sci., Vol. 23, No. 6* (Dec. 1995)

[173] S. G. Ingram and N. St. J. Braithwaite, *J. Phys. D. Appl. Phys, 21, pp. 1496-1503,* 1998

[174] M.M.M Bilek, M. Chowalla, M. Weiler, W.I. Milne, *Ion energy and plasma characterization in a silicon filtered cathodic vacuum arc, Journal of Applied Physics, 79(3):1287-1291* (1996)

[175] J. Bohlmark, M. Lattemann, J.T. Gudmundsson, A.P. Ehiasarian, Y. Aranda Gonzalvo, N. Brenning and U. Helmersson, *Thin Solid Films, 515:1522-1526* (2006)

[176] J. Vlcek, P. Kudlacek, K. Burcalova, J. Musil, *Europhys. Lett. 77, 45002,* 2007

[177] M.M.M Bilek, Y.B. Yin, D.R. McKenzie, *IEEE Transactions on Plasma Science, 24(3):1165-1173*, 1996

[178] A. Hecimovic, K. Burcalova and A. P. Ehiasarian, *J. Phys. D: Appl. Phys. 41, 095203,* 2008

[179] R. Hofer, *46th AIAA/ASME/SAE/ASEE Joint Propulsion Conference & Exhibit, High-Specific Impulse Operation of the BPT-4000 Hall Thruster for NASA Science Missions,* 2010

[180] M. S. McDonald and A. D. Gallimore, *IEPC-2011-242,* 2011

[181] J. B. Parker, Y. Raitses, and N.J. Fisch, Applied Physics Letters, Vol. 97, No. 9, pp. 091501, 2010

[182] A. Kapulkin and E. Behar, *IEPC-2013-71,* 2013

[183] A. Hecimovic, *J. Phys. D. Appl.Phys., 49 18LT01 (6pp),* 2016

[184] R.H. Havemann and J.A. Hutchby, 2001, *IEEE Proceedings of the IEEE, Vol. 89, No. 5,* May 2001

[185] E. Priest and T. Forbes, "Magnetic Reconnection – MHD theory and applications", Cambridge University Press, (2000)

[186] D. Biskamp, "Magnetic reconnection in plasmas", Cambridge University Press, (2000)

[187] M. Yamada, R. Kulsrud, and H. Ji, “Magnetic Reconnection”, *Reviews of Modern Physics, Vol. 82,* (2010)

[188] L. Sui and G. D. Holman, “Evidence for the formation of a large-scale current sheet in a solar flare”, *The Astrophysical Journal, 596:L251–L254,* (2003)

[189] V. Angelopoulos, J. P. McFadden, D. Larson, C. W. Carlson, S. B. Mende, H. Frey, T. Phan, D. G. Sibeck, K.-H. Glassmeier, U. Auster, E. Donovan, I. R. Mann, I. J. Rae, C. T. Russell, A. Runov, Xu-Zhi Zhou and L. Kepko, “Tail Reconnection Triggering Substorm Onset”, *Science, Vol. 321 no. 5891 pp. 931-935,* (2008)

[190] R. G. Giovanelli, “A theory of chromospheric flares”, *Nature, 158, 81,* (1946)

[191] J.W. Dungey, "Conditions for the occurrence of electrical discharges in astrophysical systems", *Philosophical Magazine Series 6 01/1953; 44(354):725-738,* (1953)

[192] P.A. Sweet, “The Neutral Point Theory of Solar Flares”, Electromagnetic Phenomena in Cosmical Physics, *Proceedings from IAU Symposium no. 6, p. 123, Edited by Bo Lehnert. International Astronomical Union. Symposium no. 6, Cambridge University Press,* (1958)

[193] E. N. Parker, “Sweet's mechanism for merging magnetic fields in conducting fluids”, *Journal of Geophysical Research, 62, pp. 509 - 520,* (1957)

[194] E. Priest “Magnetohydrodynamics of the Sun”, Cambridge University Press, (2014)

[195] M. Yamada, “Progress in understanding magnetic reconnection in laboratory and space astrophysical plasmas”, *Physics of Plasmas, 14, 058102,* 2007

[196] M. Yamada,H. Ji, S. Hsu, T. Carter, R. Karlsrud, N. Bretz, F. Jobes, Y. Ono and F. Perkins, “*Study of driven magnetic reconnection in a laboratory plasma”, pp 1936 – 1944, Phys. Plasmas, 4 (5),* (1997)

[197] E. R. Priest, *Società Astronomica Italiana, Memorie, vol. 61, no. 2, , pp. 383-399,* (1990)

[198] Russell et al, "Intrinsic time scale for reconnection on the dayside magnetopause", *Adv. Space Res. Vol. 19. No. 12, pp. 1913-1917* (1997)

[199] V. H. Hansteen, E. Leer, and T. E. Holzer, "The role of helium in the outer solar atmosphere". *The Astrophysical Journal 482 (1): pp 498–509,* (1997)

[200] R. Erdelyi, I. Ballai, "Heating of the solar and stellar coronae: a review". *Astron. Nachr.* 328 (8), pp 726–733, (2007)

[201] M. Yamada, R. Kulsrud, and H. Ji, “Magnetic reconnection”, *Reviews of modern physics, Vol. 82,* (2010)

[202] E. Priest and T. Forbes “*Magnetic Reconnection. MHD Theory and Application”* Cambridge University Press, (2000)

[203] M. Yamada, “Review of controlled laboratory experiments on physics of magnetic reconnection”, Journal *of Geophysical research, Vol. 104, No. A7, pp 14,529-14,541,* (1999)

[204] C. A. Cattell, "Experimental evaluation of the Lundquist number for the Earth's magnetopause and magnetotail", *Journal of geophysical research, Vol. 101, No. A12, pp 27,309-27,316,* (1996)

[205] C.T. Russell "The Solar wind interaction with the Earth's magnetosphere – a tutorial", IEEE, (2000)

[206] J.L. Burch (Editor) "The Image Mission", Kluwer Academic Publishers, (2000)

[207] D.T. Young, "Experimental aspects of ion acceleration in the Earth's magnetosphere", *Ion acceleration in the magnetosphere and ionosphere, Editor Tom Chang, American Geophysical Union,* (1986)

[208] L. Chen, R. B. White, G. Rewoldt, P. L. Colestock, P.H. Rutherford, M.N. Bussac, Y.P. Chen, F. J. Ke, and S. T. Tsai, "Theory of energetic/alpha particle effects on magnetohydrodynamic modes in tokamaks", *Proceedings of the twelfth international conference on plasma physics and controlled nuclear fusion research held by the International Atomic Energy Agency in Nice 12-19 October 1988, Volume 2, International Atomic Energy Agency Vienna*, (1989)

[209] R.L. Stenzel and W. Gekelman, "Particle Acceleration During Reconnection in Laboratory Plasmas", *Adv. Space Res. Vol. 4, No. 2-3, pp. 459-470*, (1984)

[210] M. R. Brown, C. D. Cothran, M. Landreman and D. Schlossberg, "Experimental observation of energetic ions accelerated by three-dimensional magnetic reconnection in a laboratory plasma", *The Astrophysical Journal, vol. 577, pp. L63-L66,* (September 2002)

[211] B. U. Ö. Sonnerup, "Magnetic-field re-connexion in a highly conducting incompressible fluid", *Journal of Plasma Physics, Volume 4, Issue 1 pp. 161-174,* (February 1970)

[212] W. Daughton, V. Roytershteyn, H. Karimabadi, L. Yin, B. J. Albright, B. Bergen and K. J. Bowers, "Role of electron physics in the development of turbulent magnetic reconnection in collisionless plasmas", *Nature Physics 7, pp. 539–542* (2011)

[213] J. F. Drake, M. A. Shay, and W. Thongthai, "Production of Energetic Electrons during Magnetic Reconnection", *Physical Review Letters, 94, 095001* (2005)

[214] S.P. Gary and I.H. Cairns, *Journal of Geophysical Research, Vol. 104, No. A9, pp. 19835 - 19842,* September 1999

[215] M. E. Mandt, R. E. Denton, J. F. Drake, *Geophysical Research Letters, Vol. 21, Issue 1, pp. 73–76,* 1994

[216] X.H. Wei, J.B. Cao, G.C. Zhou, H.S. Fu, O. Santolik, H. Reme, I. Dandouras, N. Cornilleau and A. Fazakerley, *Advances in Space Research Vol. 52, pp. 205–210,* 2013

[217] M. Inomoto, A. Kuwahata, H. Tanabe, Y. Ono, and TS Group, 2013, *Physics of Plasmas 20, 061209,* doi.org/10.1063/1.4811469

[218] T. D. Phan, J. F. Drake, M. A. Shay, F. S. Mozer, and J. P. Eastwood, *Phys. Rev. Lett. 99, 255002* (2007)

[219] M. Swisdak, M. Opher, J. F. Drake, and F. Alouani Bibi, *The Astrophysical Journal, 710, pp. 1769–1775,* 2010, doi:10.1088/0004-637X/710/2/1769

[220] E. G. Zweibel and M. Yamada, *Proceedings of the Royal Society A, 472: 20160479*, DOI: 10.1098/rspa.2016.0479, (2016)

[221] X.H. Wei, J.B. Cao, G.C. Zhou, H.S. Fu, O. Santolik, H. Reme, I. Dandouras, N. Cornilleau and A. Fazakerley, *Advances in Space Research Vol. 52, pp. 205–210*, (2013)

[222] M. Inomoto, A. Kuwahata, H. Tanabe, Y. Ono, and TS Group, *Physics of Plasmas 20, 061209*, doi.org/10.1063/1.4811469, (2013)

[223] R.L. Stenzel, W. Gekelman and J.M. Urratia, **"**Laboratory experiments on magnetic reconnection and turbulence"*, Magnetic Reconnection and Turbulence, M.A. Dubois et al , Editor Editions de Physique,* (1985)

[224] R.L. Stenzel, W. Gekelman, J.M. Urratia and H. Pfister, **"**Laboratory experiments on magnetic reconnection and current systems*", Adv. Space Res. Vol. 10, No. 9, pp. (9)55- (9)71*, (1990)

[225] H. Bohlin, A. Von Stechow, K. Rahbarnia, O. Grulke and T. Klinger, "VINETA II: A linear magnetic reconnection experiment", *Review of Scientific Instruments, 85, 023501,* (2014)

[226] M. Yamada, Y. Ono, A. Hayakawa, M. Katsurai, and F. W. Perkins, "Magnetic reconnection of plasma toroids with cohelicity and counterhelicity", *Phys. Rev. Lett. 65, 721,* (1990)

[227] M. Yamada, H. Ji, S. Hsu, T. Carter, R. Kulsrud, N. Bretz, F. Jobes, Y. Ono, and F. Perkins, "Study of driven magnetic reconnection in a laboratory plasma", *Physics of Plasmas 4, 1936* (1997)

[228] N. Katz, J. Egedal, W. Fox, A. Le, J. Bonde and A. Vrublevskis, "Laboratory observation of localized onset of magnetic reconnection", *Physical Review Letters, 104, 255004* (2010)

[229] F. Chen, **"**Langmuir Probe Diagnostics", *Mini-Course on Plasma Diagnostics, IEEE-ICOPS meeting, Jeju, Korea,* (2003)

[230] R. L. Merlino, *Am. J. Phys. 75, 12, pp. 1078 – 1085*, (2007)

[231] R. L. Stenzel and J. M. Urrutia, *Phys. Plasmas **4** (1), pp. 26-35*, (1997)

[232] J.A. Simpson, *Rev. Sci. Instrun, 32, 1283*, (1961)

[233] D. Grondona, H. Kelly and A. Marquez, *Appl. Phys. Lett., Vol. 79, No. 1, pp. 317-319* (2001)

[234] R. Turner, "Theta pinch plasma gun studies", *APL Technical digest, pp. 2 – 13*, (June 1969)

[235] S. N. Bathgate, R. Ganesan, M. M.M. Bilek and D. R. McKenzie, *Eur. Phys. J. Appl. Phys. 76: 30801*(2016)

[236] M. R. Brown, C. D. Cothran, M. Landreman, D. Schlossberg, W. H. Matthaeus, G. Qin, V. S. Lukin and T. Gray, "Energetic particles from three-dimensional magnetic reconnection events in the Swarthmore Spheromak Experiment", *Physics of Plasmas, Vol. 9, No.5, pp. 2077 - 2084*, (May 2002)

[237] M. R. LaPointe, "Theta-Pinch Thruster for Piloted Deep Space Exploration", *NASA/CR-2000-210355, AIAA 2000-3365*, (2000)

[238] A.E. Wendt, *Rev. Sci. Instrum, Vol 72, No. 7, pp.,2926-2930*, 2001

[239] A. Papoulis *"Signal analysis"*, McGraw-Hill International Book Company, 1984